

STUDY OF CUBIC III-V NITRIDES FOR DEVICE
APPLICATIONS

by

NORZAINI BINTI ZAINAL (Msc.)

Thesis submitted to the University of Nottingham
for the degree of Doctor of Philosophy

JULY 2010

DEDICATED TO MAK AND ABAH

CONTENTS

LIST OF FIGURES	vi
LIST OF TABLES	xi
ACKNOWLEDGEMENT	xii
ABSTRACT	xiii
LIST OF PUBLICATIONS.....	xv
CHAPTER 1: INTRODUCTION.....	1
REFERENCES.....	5
CHAPTER 2: INTRODUCTION TO CUBIC III-V NITRIDES SEMICONDUCTORS	6
2.1: CRYSTAL STRUCTURE.....	6
2.2: BASIC PROPERTIES OF III-NITRIDES	7
2.3: SUMMARY OF CUBIC GaN RESEARCH	9
2.3.1: Studies of Cubic GaN growth.....	9
2.3.2: Optical Studies of Cubic GaN	14
2.3.3: Electrical Studies of Cubic GaN.....	20
2.4: CONCLUSIONS	23
REFERENCES.....	24
CHAPTER 3: SAMPLE PREPARATION AND EXPERIMENTAL TECHNIQUES	27
3.1: SAMPLE GROWTH	27
3.2: PROCESSING CUBIC GaN SUBSTRATES	28
3.3: SAMPLE CHARACTERISATIONS	30
3.3.1: Optical studies by photoluminescence measurements.....	30
3.3.1.1: Sample Mounting	31
3.3.1.2: Cryostat.....	31
3.3.1.3: Photoluminescence Measurements	33
3.3.1.4: Micro-Photoluminescence Measurement.....	36
3.3.1.5: Pump-probe measurement	40
3.3.2: Surface analysis by AFM.....	43
3.3.3: Structural analysis by XRD	44
3.3.4: Compositional analysis by SIMS.....	47
3.3.5: Electrical study by Hall effect	48
3.3.5.1: Hall voltage measurement	49
3.3.5.2: Resistivity measurement.....	49
3.4: DEVICE PREPARATIONS ON CUBIC NITRIDES BASED TUNNEL DIODE	51
3.5: ELECTRICAL MEASUREMENTS ON CUBIC NITRIDES BASED TUNNEL DIODES ...	53
3.6: CONCLUSIONS	54
REFERENCES.....	55

CHAPTER 4: STUDIES OF CUBIC GaN 56

4.1: STUDIES OF OPTICAL PROPERTIES OF CUBIC GaN..... 56
4.1.1: PL measurement on cubic GaN with the variation of III/V ratio..... 56
4.1.2: PL results for cubic GaN with the variation of growth rate..... 60
4.1.3: PL results for cubic GaN with the variation of wafer position 62
4.1.4: PL results for cubic GaN with the variation of thickness 64
4.1.5: PL results for bulk cubic GaN 67
4.2: THE ELASTO-OPTICAL STUDY ON CUBIC GaN 71
4.2.1: The effect of strain pulse on the reflectivity in cubic GaN..... 71
4.2.2: Measuring sound velocity, elastic constant and refractive index in cubic GaN..... 73
4.2.3: The dependence of the refractive index on photon energy in cubic GaN 75
4.3: STUDIES OF ELECTRICAL TRANSPORT IN CUBIC GaN 78
4.3.1: Electrical properties in cubic GaN with the variation of dopants 78
4.3.2: Electrical properties in cubic GaN with the variation of thickness..... 80
4.4: PL RESULTS FOR CUBIC $Al_xGa_{1-x}N$ 82
4.5: CONCLUSIONS 86
REFERENCES 87

CHAPTER 5: PROCESSING OF CUBIC GAN SUBSTRATE..... 89

5.1: COMPOSITIONAL ANALYSIS FOR CUBIC GaN 89
5.2: OPTICAL STUDIES FOR CUBIC GaN 92
5.3: SURFACE MORPHOLOGY STUDIES FOR CUBIC GaN 94
5.4: GROWTH OF DEVICE ON CUBIC GaN SUBSTRATE.....96
5.5: CONCLUSIONS 100
REFERENCES 101

CHAPTER 6: CUBIC NITRIDES BASED RESONANT TUNNELLING DIODE..... 102

6.1: TUNNELLING PROCESS IN DEVICE STRUCTURE 103
6.2: STUDIES OF WURTZITE NITRIDES TUNNELLING DIODES 105
6.3: MODELLING OF CUBIC NITRIDES TUNNELLING DEVICE 107
6.3.1: Theoretical Calculation of Resonant Level in Quantum Well 108
6.3.2: Theoretical Calculation of Transmission Coefficient 111
6.3.3: Theoretical Calculation of Tunnelling Current in DBRTD 114
6.4: MODELLING OF CUBIC $Al_xGa_{1-x}N/GaN$ DBRTD.....115
6.4.1: Numerical Calculation of Resonant Energy in DBRTD structure 116
6.4.2: Numerical Calculation of Tunnelling Current in $Al_xGa_{1-x}N/GaN$ DBRTD 118
6.5: VERTICAL TRANSPORT IN CUBIC $Al_xGa_{1-x}N/GaN$ DBRTD..... 125
6.5.1: Vertical transport in bulk tunnel device..... 125
6.5.2: Vertical transport in smaller device 128
6.6: CONCLUSIONS 139
REFERENCES 140

CHAPTER 7: CONCLUSIONS AND FUTURE PLANS.....142

7.1: STUDIES OF CUBIC GaN.....142
7.2: PROCESSING OF CUBIC GaN SUBSTRATE 143
7.3: CUBIC NITRIDES BASED RESONANT TUNNELLING DIODE..... 143
7.4: SUGGESTIONS FOR FURTHER WORK 144

CHAPTER 8: APPENDIX141

LIST OF FIGURES

Figure 2.1	The atom arrangement in (a) wurtzite and (b) zinc-blende structures	7
Figure 2.2	The growth diagram for cubic GaN grown by MBE. Three growth regimes under Ga stable, N stable and Ga droplets were defined with a constant N flux. The figure was taken from Sung et al [19].	11
Figure 2.3:	A typical PL spectrum for a thin (~0.8 μ m) cubic GaN layer measured at 4.2K. This spectrum was taken from our measurement.	15
Figure 2.4:	A typical PL spectrum for a thick (~1.9 μ m) cubic GaN layer measured at 4.2K. This spectrum was taken from our measurement.	20
Figure 3.1:	(a) Cubic GaN was placed on ceramic plate by low temperature wax. (b) Free standing cubic GaN was mounted on the polishing jig. (c) The sample was polished by the chemical-mechanical polishing machine. (d) Free-standing cubic GaN after polishing.	29
Figure 3.2	The dependence of the removal of cubic GaN on polishing time.	30
Figure 3.3	A modified schematic diagram of Optistat continuous flow cryostat system [5].	32
Figure 3.4	A schematic diagram of the PL system. The exciting source is a 355nm tripled Nd:YAG laser and the cryostat is cooled down to helium temperature.	34
Figure 3.5	A schematic diagram of light dispersion in the monochrometer used in this experiment. The diagram is modified from [8].	35
Figure 3.6	A schematic diagram of sample mounting on the special designed holder.	37
Figure 3.7	A schematic diagram of micro PL system. Inset (a): the mechanism for focusing the incident light onto the sample in the micro objective mirror. (b): the laser beam shines on the edge of 50 μ m cubic GaN sample in the cryostat.	39
Figure 3.8	A schematic diagram of the pump-probe measurement. The exciting source is a Ti-sapphire laser ($\lambda=800$ nm) and the sample is cooled down to helium temperature in an optical cryostat.	42
Figure 3.9	A modified schematic diagram of AFM. Original picture was taken from [8].	44

Figure 3.10	The x-ray diffraction in a crystal. This diagram is taken and modified from [10].	45
Figure 3.11	Reported data of XRD for GaN films (a) 2.5 μm thick hexagonal GaN grown on (111) Si substrate [11]. (b) 1.5 μm thick cubic GaN grown on (100) GaAs substrate [12].	46
Figure 3.12	The bombardment of primary ions on the sample surface and knock off the secondary ions from the surface. This picture is taken from [13].	47
Figure 3.13	A schematic diagram of Hall Effect measurement. There are four contacts at the corners of the sample. The red lines show the Hall voltage across different points with the variation of current and magnetic field polarities.	48
Figure 3.14	A schematic diagram of cubic $\text{Al}_x\text{Ga}_{1-x}\text{N}/\text{GaN}$ based tunnel diode	51
Figure 3.15	The fabrication process for forming smaller mesa-structures for cubic AlN/GaN based tunnel diode.	52
Figure 3.16	The circuit diagram for I - V measurement.	53
Figure 3.17	The schematic diagram for conductance measurement.	54
Figure 4.1	PL spectra for different samples grown with different III/V ratio. There are three clear peaks that are related to the emission in cubic GaN. Insert figure shows the hexagonal related emission around 3.47eV.	58
Figure 4.2	XRD data for the sample grown nearly under stoichiometric condition. The sample shows the cubic signal in [002] direction around 40°. The intensity of GaAs is coming from the GaAs substrate.	59
Figure 4.3	PL spectra for the cubic samples grown at different growth rates.	61
Figure 4.4	A piece of wafer that be used for PL measurement (b) Dependence of PL intensity of hexagonal/cubic signals as a function of energy at different distance from the centre part of the wafer. Clearly, the signal of hexagonal signal is stronger towards the edge of sample.	63
Figure 4.5	PL spectra for cubic GaN samples with different thicknesses. The signal due to hexagonal material is stronger when the thickness is increased. Insert figure shows the large scale for thinner cubic GaN.	65

Figure 4.6	XRD data for 12.0 μ m thick cubic GaN. The cubic signal in [002] direction is observed around 40°. The intensity of GaAs is coming from the GaAs substrate.	67
Figure 4.7	PL spectra with the variation of depths in a ~50 μ m thick cubic GaN (distances measured from GaAs/GaN interface). The spectra are clearly dominated by hexagonal related emission.	69
Figure 4.8	The PL intensity of hexagonal (dashed line with full-square) and the percentage of hexagonal inclusion (solid line with full-circle) as the functions of depth for a ~50 μ m thick cubic GaN. The point near GaAs/GaN interface corresponds to the start point.	70
Figure 4.9	The change of the reflectivity from cubic GaN film as a function of the time delay between the probe pulse and arrival time of the strain pulse to the GaN film. The peaks are labelled as <i>I-4</i> that show the strain pulse passing the related interfaces.	72
Figure 4.10	(a) The change of reflectivity from cubic GaN film as a function of the time delay. (b) The Fourier transform of the temporal signal.	73
Figure 4.11	The Fabry-Perot oscillations in cubic GaN film at room temperature.	76
Figure 4.12	The dependence of the derived refractive index on photon energy for cubic GaN film at room temperature. The refractive index is increased exponentially with the photon energy. The derived refractive index at low temperature is included for as comparison.	77
Figure 4.13	The sample structure with the variation of thickness, <i>d</i> .	80
Figure 4.14	PL spectra for cubic GaN (SN-368) and cubic Al _{0.2} Ga _{0.8} N (SN-370) at low temperature.	82
Figure 4.15	The PL peak energy of cubic Al _{<i>x</i>} Ga _{1-<i>x</i>} N samples with the variation of Al content, <i>x</i> at 4.7K (a) PL peaks that could be due to emission from cubic Al _{<i>x</i>} Ga _{1-<i>x</i>} N and (b) peaks that could be due to emissions hexagonal Al _{<i>x</i>} Ga _{1-<i>x</i>} N.	84
Figure 5.1	SIMS data in cubic GaN samples at different probe direction (a) Thin c-GaN before etching (b) Thick c-GaN after etched. The shaded area needs to be removed by polishing.	90
Figure 5.2	XRD data for a free standing thick cubic GaN layer. Clearly, no peak related to GaAs is observed.	92
Figure 5.3	PL spectra for polished cubic GaN at different polishing time. Clearly, hexagonal peak around 3.42eV decreases with time.	94
Figure 5.4	Dependence of the value of root mean square (RMS) roughness with the variation of removal thickness.	95

Figure 5.5	AFM images of the surface of (a) polished cubic GaN substrate and (b) commercial hexagonal substrate.	96
Figure 5.6	Cubic $\text{In}_x\text{Ga}_{1-x}\text{N}$ LED structure grown on unpolished/polished free standing cubic GaN substrates.	97
Figure 5.7	PL spectra for $\text{In}_x\text{Ga}_{1-x}\text{N}$ LED structures grown on unpolished and polished free standing cubic GaN substrates.	98
Figure 5.8	Current-voltage characteristics for $\text{In}_x\text{Ga}_{1-x}\text{N}$ LED structures grown on unpolished and polished free standing cubic GaN substrate.	99
Figure 5.9	EL spectrum for $\text{In}_x\text{Ga}_{1-x}\text{N}$ LED grown on polished free standing cubic GaN substrate. The emission wavelength of the $\text{In}_x\text{Ga}_{1-x}\text{N}$ LED structure is around 460nm.	100
Figure 6.1	(a)-(c) illustrate the changes of the band structure with the variation of applied voltage, V . The width of resonant level, Γ is indicated by the red arrows. (d) shows the dependence of current on applied voltage, V .	104
Figure 6.2	Schematic diagram of the wave function of electron at the first bound state energy, E_{pk} in the quantum well with finite barrier layers at the conduction band. The well width and potential depth are given as a and V_0 , respectively.	108
Figure 6.3	The calculated distribution of electron wave function at the first energy bound state in $\text{Al}_{0.1}\text{Ga}_{0.9}\text{N}/\text{GaN}$ double barriers structure.	111
Figure 6.4	A schematic diagram of the tunnelling of electron through a single barrier. The wave function of the electron changes as it moves towards different regions.	112
Figure 6.5	A schematic of cubic $\text{Al}_x\text{Ga}_{1-x}\text{N}/\text{GaN}$ tunnel diode.	115
Figure 6.6	The calculated distribution of probability electron density at the conduction band for different Al composition, x of cubic $\text{Al}_x\text{Ga}_{1-x}\text{N}$ barrier layers.	117
Figure 6.7	The calculated resonant energy level in the well as a function of well width.	118
Figure 6.8	The calculated tunnelling current-voltage of $\text{Al}_{0.3}\text{Ga}_{0.7}\text{N}/\text{GaN}$ DBRTD with different conduction band offsets at room temperature.	120
Figure 6.9	The dependence of peak current and resonant width on the well width in $\text{Al}_{0.3}\text{Ga}_{0.7}\text{N}/\text{GaN}$ double barrier device.	121
Figure 6.10	I - V characteristic for $\text{Al}_{0.3}\text{Ga}_{0.7}\text{N}/\text{GaN}$ DBRTD with different barrier thickness.	122

Figure 6.11	The optimum barrier thickness corresponding to the Al composition, x .	123
Figure 6.12	I - V characteristic for $\text{Al}_{0.1}\text{Ga}_{0.9}\text{N}/\text{GaN}$ DBRTD at different temperature.	124
Figure 6.13	I - V characteristic for $\text{Al}_{0.1}\text{Ga}_{0.9}\text{N}/\text{GaN}$ DBRTD. No NDR is observed.	126
Figure 6.14	Dependence of the current and conductance, G on the applied voltage for $\text{Al}_{0.1}\text{Ga}_{0.9}\text{N}/\text{GaN}$ DBRTD at 77K. A weak feature can be observed around 0.6V in the G - V characteristic.	127
Figure 6.15	Dependence of current on applied voltage for SN-298. The device shows a sharp NDR effect around 1.3V.	129
Figure 6.16	I - V characteristic for SN-299 at low temperature. Clearly, the NDR effect is observed at 1.36V.	131
Figure 6.17	I - V characteristic at different bias for SN-298. Clearly the NDR effect disappears in the subsequent sweeping.	132
Figure 6.18	I - V characteristic for another device of SN-298 at different sweeping. Clearly, the NDR effect is observed in the subsequence measurements.	133
Figure 6.19	I - V characteristic for SN-302 at different bias. Clearly, the signal of hysteresis is observed.	135
Figure 6.20	I - V characteristic for some cubic $\text{Al}_{0.3}\text{Ga}_{0.7}\text{N}/\text{GaN}$ devices with different structural parameters. The NDR effect is observed in all type of the samples.	136
Figure 6.21	Two possible consequences of structural fluctuations during the growth.	138

LIST OF TABLES

Table 2.1	Basic properties of hexagonal GaN, AlN and InN at 300K.	8
Table 2.2	Basic properties of cubic GaN, AlN and InN at 300K.	8
Table 2.3	The best reported cubic GaN layers grown under optimum growth conditions in different studies.	13
Table 2.4	The reported optical properties in cubic GaN at low temperature.	18
Table 4.1	Elasto-optical parameters for cubic GaN. The respective values for hexagonal GaN are given for a comparison.	78
Table 4.2	The electrical properties in cubic GaN samples doped with different dopants.	79
Table 4.3	The electrical properties of undoped cubic GaN samples with different thickness, d obtained from the experiment.	81
Table 4.4	Detailed specification of cubic $\text{Al}_x\text{Ga}_{1-x}\text{N}$ samples with the variation of Al content, x and thickness.	82
Table 4.5	Summary of the peak emission energies in different cubic $\text{Al}_x\text{Ga}_{1-x}\text{N}$ samples.	85
Table 6.1	List of the values of electron affinities for GaN and AlN from literature.	119
Table 6.2	Detailed structure for the grown cubic $\text{Al}_{0.3}\text{Ga}_{0.7}\text{N}/\text{GaN}$ DBRTDs	128
Table 6.3	Summary of the results from I - V measurement at 300K.	137
Table 6.4	Summary of the results from I - V measurement at 77K.	137

ACKNOWLEDGEMENT

First and foremost, I would like to express my gratitude to God, with his blessing; I had been able to finish my thesis successfully. It is my pleasure to express special thanks to my first supervisor, Prof. A.J Kent for his valuable guidance, patience, advice and support. He is the person who has introduced me to the real world of research and has been more than willing to spend his time educating and directing me throughout the journey of my study. Equally, I am indebted to Dr. Sergei Novikov for giving me more information about growth studies and Prof. Aundrey Akimov for helping me doing photoluminescence measurements. I would like to thank Dr. Paul Walker for helping me in experimental setups and sharing his experience about the challenge of being a PhD student.

My thanks also go to clean room people; Dr. Chris Mellor, Mr. Jas Chauhan and Mr. Dave Taylor for their assistance fabricating my tunnel devices. To my colleagues, Mr. Ryan Beardsley and Mr. Daniel Moss, thanks for being best mates. They are not only the people who always have been patient and listened to my whining during the course but also have been great buddies to embark myself with the life and culture in the UK. Also not to be forgotten are my friends from Malaysia, Fae, Nazri and Wan Maryam. They are my family here and we have shared a lot of wonderful moments in the UK together.

To my parents, Zainal Osman and Siti Rohani and my siblings, Kak yong, Cik Wie, Nina and Adik, I love you guys. Really looking forward to having such enjoyable time together again with you all. Finally, my deepest appreciation goes to my former supervisor in Malaysia, Prof. Zainuriah Hassan, my lecturers and friends for all their moral support and encouragement throughout the duration of my studies.

ABSTRACT

This thesis describes the optimisation of the growth of bulk cubic GaN with low hexagonal content and with the intention of making it a commercial substrate for device applications. The optimised material was then applied for fabrication of cubic $\text{Al}_x\text{Ga}_{1-x}\text{N}/\text{GaN}$ based double barrier resonant tunnelling diode (DBRTD) devices. The devices with a clear negative differential resistance (NDR) and high reproducibility are demonstrated.

In the early part of this project, we reported a study on cubic GaN material with the variation of III/V ratio, growth rate and wafer position. Using PL and XRD measurements, we found that all these factors influence the increase of hexagonal inclusions in cubic GaN, leading to poor quality in cubic nitride growth. This problem however is more significant when the thickness of cubic GaN is increased. From the calibration work, a $\sim 50\mu\text{m}$ cubic GaN layer has been grown for the first time with a low average proportion of hexagonal inclusions of around 10% and just few percent at the interface of cubic GaN and GaAs substrate. Thus, the interface would be the most suitable surface for further growth.

Next, we investigated the fundamental properties of cubic GaN using picosecond acoustic measurements. In this material, the sound velocity is found to be $6.9\pm 0.1 \text{ km s}^{-1}$, elastic constant = $285\pm 8 \text{ GPa}$ and the refractive index at 400nm = 2.63 ± 0.04 . Comparison with hexagonal GaN films indicated that these parameter values differ considerably in different symmetry of GaN. These show the usefulness of our layers for determination of the basic properties of cubic GaN using a wide range of techniques.

From the Hall transport measurement, the electrical properties of undoped cubic GaN samples depend on growth conditions and thickness. In this work, we successfully demonstrated p-type cubic GaN:Mn using C-doping and n-type behaviour from Si-doped cubic GaN. However, these samples have high electron density but low

mobility as the residual impurities and intrinsic defects were found to be higher inside the samples.

We extended the technology of growing cubic GaN to cubic $\text{Al}_x\text{Ga}_{1-x}\text{N}$. A number of cubic $\text{Al}_x\text{Ga}_{1-x}\text{N}$ samples with different Al content, x were grown and characterised by PL measurement. We found that the hexagonal PL starts to dominate when x is increased, even for thin samples. This could be due to the problems of maintaining cubic $\text{Al}_x\text{Ga}_{1-x}\text{N}$ growth. It could also be due to the miscibility gap between AlN and GaN. More results and data are required to explain this behaviour.

In this thesis, we demonstrated potential cubic GaN substrates for device applications for the first time. The study on bulk cubic GaN showed that the interface between the cubic GaN and the GaAs substrate has only few percent of hexagonal content. Thus, the surface that was in contact with GaAs is the most suitable surface for further processing and growth. Due to the effect of strain, As inclusions and defects were already formed on the surface. By polishing the surface for ~ 2 hours, these problems were minimised and the surface still had low hexagonal content. In this work, the first working InGaN LED device grown on a polished free-standing cubic GaN substrate has been demonstrated. Our polished cubic GaN substrates also improve the quality of the grown device as been measured by luminescence and I - V characteristics.

In the last part of this thesis, we investigated the potential of cubic GaN for developing cubic $\text{Al}_x\text{Ga}_{1-x}\text{N}/\text{GaN}$ DBRTD devices. In the first stage of this work, the I - V characteristics of the cubic tunnel devices were calculated for various band offset, well width, barrier composition and barrier thickness parameters. From this work, optimal designs of cubic $\text{Al}_x\text{Ga}_{1-x}\text{N}/\text{GaN}$ tunnel diodes that could be fabricated and characterised were proposed. The result was then used as a starting point for the growth of cubic $\text{Al}_x\text{Ga}_{1-x}\text{N}/\text{GaN}$ DBRTD. A number of cubic $\text{Al}_x\text{Ga}_{1-x}\text{N}/\text{GaN}$ tunnel devices with different structural parameters were grown. Some devices showed a clear NDR effect but not all of them are reproducible due to breakdown of the device. This factor may also contribute to the irreproducibility of wurtzite (hexagonal) nitride based tunnel diodes in addition to the problem related to charge trapping.

LIST OF PUBLICATIONS

1. D. Moss, A.V Akimov, S.V. Novikov, R.P. Campion, C.R. Staddon, N. Zainal, C.T. Foxon, A.J. Kent, Elasto-optical properties of zinc-blende (cubic) GaN measured by picosecond acoustics, *J. Phys. D: Appl. Phys.* **42** 115412 (2009)
2. S.V. Novikov, C.R. Staddon, A.V. Akimov, R.P. Campion, N. Zainal, A.J. Kent, C.T. Foxon, C.H. Chen, K.M. Yu and W. Walukiewicz, Molecular beam epitaxy of crystalline and amorphous GaN layers with high As content, *J. Cryst. Growth* **311** 3417 (2009)
3. Sergey V. Novikov, Chris R. Staddon, Andrey V. Akimov, Richard P. Campion, Norzaini Zainal, Anthony J. Kent, C. Thomas Foxon, Chien H. Chen, Kim M. Yu, Wladek Walukiewicz, Growth by Molecular Beam Epitaxy of GaNAs alloys with high As content for potential photoanode applications in hydrogen production, *Mater. Res. Soc. Symp. Proc.* **1167** 1167-004-07 (2009)
4. S.V. Novikov, N. Zainal, A.V. Akimov, C.R. Staddon, A.J. Kent, C.T. Foxon, MBE as a method for the growth of freestanding zinc-blende (cubic) GaN layers and substrates, *J. Vac. Sci. Technol. B* **28** 3 (2010)
5. N. Zainal, P. Walker, A.J Kent, Modelling of Cubic $\text{Al}_x\text{Ga}_{1-x}\text{N}$ GaN Resonant Tunnel Diode Structures, *Phys. Status Solidi (C)*, DOI 10.1002/pssc.200983543, (2010)
6. S.V. Novikov, N. Zainal, C.T. Foxon, A.J. Kent, F. Luckert, P.R. Edwards, R.W. Martin, Study of unintentional arsenic incorporation into free-standing zinc-blende GaN and AlGa_N layers grown by molecular beam epitaxy on GaAs substrates, *Phys. Status Solidi (C)*, DOI 10.1002/pssc.200983420 (2010)

CHAPTER 1: INTRODUCTION

GaN and its related alloys are among the most favoured compound semiconductors for many varieties of device applications. In fact, considerable advancements in fabrication technology nowadays have expanded the area for many novel researches in nitride-based structures/devices. As compared to the III-arsenide system, the nitride ternary alloys have much wider energy bandgap and optoelectronic devices based on them can cover almost the entire spectral range; from infra-red to mid-ultraviolet (UV). During the last few decades, numerous efforts have been made to produce light emitting diodes (LEDs) and laser diodes (LDs) that can operate at shorter wavelengths with excellent luminescent properties. Quite recently, nitride based blue LEDs with external quantum efficiency higher than 65% have been developed [1]. Also, a deeper UV emitting LD with emission at 336nm is now available [2]. These dramatic improvements in nitride-based opto-devices have driven a number of innovations and applications in solid-state energy-saving technologies, optical data processing and storage, fibre communication, traffic signals, mobile backlights, medical operations and general purposes, e.g. printers and scanners.

The large band discontinuity of the AlGaN/GaN heterojunction allows GaN-based devices to give an output power density 5–10 times larger than that of GaAs-based devices. With the thermal conductivity of around 1.5W/cmK, GaN based devices could work well at much higher temperature, (typically up to 200°C). Moreover, GaN has high breakdown field about 3MV/cm [3] and this is useful for GaN based devices operating at high power, especially for smaller dimensional structures. For example, Hoshi et al have developed a high power GaN-HEMT with a highly linear gain of 17dB and a high drain efficiency of 58% at a frequency of 2.14GHz and at an operating voltage of 50V [4].

The group III-nitrides normally crystallize in the hexagonal (wurtzite) phase. A unique feature of the hexagonal III-nitrides grown on *c*-axis is the existence of strong spontaneous and piezoelectric fields. In AlGaN/GaN heterostructures, the fields may

enhance the electron accumulations and increases the effective barrier height at the heterointerface. These effects are beneficial for some device applications, e.g. HEMT [4]. On the other hand, such fields can decrease the overlap of the wavefunctions in the quantum well and thus reduce the efficiency of LED and LD devices [5]. In the case of a tunnel diode, the strong fields may increase carrier trapping and may lead to highly asymmetric current-voltage (I - V) characteristics [6]. The internal fields also complicate the calculation of the tunnelling properties [7, 8].

For these reasons, growing III-V nitride materials in non-polar (semipolar) directions is preferable so that the internal fields can be eliminated or reduced. Up to now, there have been several attempts to fabricate non-polar bulk hexagonal crystals and templates on a - and m -planes; e.g. [9, 10]. However, their quality is still far from the best expectation, and they are also costly and difficult to produce. An alternative way is growing GaN directly in the non-polar (001) cubic direction. Apart from eliminating the internal fields, other reasons that increase the interest in cubic GaN are the ability to cleave the material on the perpendicular {110} cleavage planes and also the higher electron and hole mobility due to its higher symmetry structure.

Unlike for the hexagonal structure, the growth of cubic GaN is more problematic due to the thermodynamically unstable nature of the structure. Hexagonal inclusions are easily formed in cubic GaN, mainly when the thickness increases. Therefore, considerable advances in the growth of cubic nitrides are required in order to exploit the advantages of the material in many applications. Until now, no work has ever demonstrated a high quality bulk cubic GaN. If the bulk cubic GaN is available, we can use it as a substrate for growing a device or structure thus minimising problems due to strain and dislocation density.

Due to their advantageous properties, III-nitride materials have also been used in *resonant tunnelling diode* (RTD) fabrication. In this structure, it is possible to observe the fundamental properties of electron waves tunnelling even at higher temperature, power and frequency. Moreover, RTDs have received much attention owing to their negative differential resistance (NDR) properties, ease of structural growth and fabrication, and flexibilities in design and circuit functionality.

In general, the quality of RTDs is described by the ratio of peak current to valley current (PVR), e.g [11]. Up to now, considerable progress in nitride epitaxial growth has been made in order to improve the PVR value at room temperature. If an RTD is realized in cubic nitride semiconductors, a number of novel possibilities would exist for development and exploitation. For example, the calculation of tunnelling properties becomes more straightforward and tunnelling effects would be reproducible as the effect of charge trapping due to the internal fields would be eliminated. To my knowledge, no work on cubic nitride based tunnel devices has been reported so far, as the growth of such devices does not belong to the “standard” tasks of crystal growers.

The aim of this thesis is to develop the growth technology for the cubic nitride system so that high quality cubic GaN with low hexagonal content is possible even at larger film thickness. Once this technology has been established, the bulk cubic GaN will be processed to make it as a commercial substrate for cubic nitride based LED devices. The growth technology of cubic AlGaN is also adopted for developing high quality cubic nitride based tunnel structures.

This thesis is organised as follows: In Chapter 2, the reader will be introduced to basic properties of cubic and hexagonal GaN. As this thesis is focussing on cubic GaN, published results and data on growth, optical and electrical aspects of the material are reviewed. This allows the reader to be aware of the current development of cubic GaN. Chapter 3 gives description of the experimental setups used in this work and discusses some limitations that had been encountered during the measurements. Chapter 4 presents results and discussions on optical measurements of cubic GaN. From this work, the optimal growth conditions for high quality bulk cubic GaN is proposed. Once high quality bulk cubic GaN is successfully grown, it is practical to investigate the fundamental physical properties of the structure. In addition to this work, the electrical properties of cubic GaN are studied. Chapter 5 reports the processing of bulk cubic GaN to make it into a free standing substrate and, for the first time, a working cubic InGaN/GaN LED grown on the free standing cubic GaN substrate will be demonstrated.

Chapter 6 briefly presents the theoretical background of the quantum tunnelling process in RTDs. Since there are no published results and data available for cubic-based tunnel structures, the progress on developing RTDs in hexagonal $\text{Al}_x\text{Ga}_{1-x}\text{N}/\text{GaN}$ will be outlined instead. This allows the reader to understand the problems associated with hexagonal nitride based RTDs and appreciate the motivation of this project to grow RTDs in the cubic nitride system. This is followed by a presentation of detailed numerical calculation of the tunnelling I - V characteristic of cubic $\text{Al}_x\text{Ga}_{1-x}\text{N}/\text{GaN}$ double barrier RTD (DBRTD) with the variation of structural parameters such as band offset, well width, barrier composition and thickness. Optimal designs of the tunnel structure that could possibly be fabricated and characterised will be proposed. Based on the simulation result, cubic $\text{Al}_x\text{Ga}_{1-x}\text{N}/\text{GaN}$ DBRTDs are then fabricated and their electrical properties are studied by I - V measurement. Finally, a summary of these works together with a number of suggestions for future research are presented in Chapter 7.

REFERENCES

1. Regina Mueller-Mach, G.O.Mueller, Michael R. Krames, Oleg B. Shchekin, Peter J. Schmidt, Helmut Bechtel, Ching-Hui Chen, Oliver Steigelmann, *Phys. Status Solidi RRL* (2009). **3**: p. 215.
2. H. Yoshida, M. Kuwabara, Y. Yamashita, Y. Takagi, K. Uchiyama, H. Kan, *New. J. Phys.*, (2009). **11**: p. 125013.
3. Yusuke Yoshizumi, S.H. Tatsuya Tanabea and Makoto Kiyamaa, *J. Cryst. Growth*, (2007). **298**: p. 875.
4. S. Hoshi, H. Okita, Y. Morino, M. Itoh, *Oki Technical Review*, (2007). **74**: p. 90.
5. Li. Youqun, F. Wenqing, L. Weihua, L. Hechu, M. Chunlan, W. Li, J. Fengyi, *Journal of Luminescence*, (2007). **122-123**: p. 567-570.
6. A.E. Belyaev, O. Makarovskiy, D.J. Walker, L. Eaves, C.T. Foxon, S.V. Novikov, L.X. Zhao, R.I. Dykeman, S.V. Danylyuk, S.A. Vitusevich, M.J. Kappers, J.S. Barnard, C.J. Humphreys *Physica E*, (2004). **21**: p. 752.
7. A.N. Razzhvalov, S.N. Grinyaev, *Semiconductors*, (2008). **42**: p. 580.
8. F. Sacconi, A., Di Carlo, P. Lugli, *Phys. Stat. Sol. (a)*, (2002). **190**: p. 295.
9. T. Paskova, R. Kroeger, D. Hommel, P. P. Paskov, B. Monemar, E. Preble, A. Hanser, N. M. Williams, M. Tutor, *Phys. Stat. Sol. (c)*, 2007. **4(7)**: p. 2536-2539.
10. Y. Jung, M.M. J. Hite, C.R. Eddy, J. Kim, *Thin Solid Films*, (2010). **518**: p. 1747.
11. K. Kishino, A. Kikuchi, *Phys. Stat. Sol. (a)*, (2002). **190**: p. 23.

CHAPTER 2: INTRODUCTION TO CUBIC III-V NITRIDES SEMICONDUCTORS

It is well known that the basic properties of a semiconductor material are influenced by the arrangement of atoms, which also affects its optical and electrical properties. However, the presence of impurities and defects inside the material are unavoidable during growth. This disturbs the atomic arrangements and can affect the optical and electrical properties of the material.

In this chapter, basic properties of the hexagonal (wurtzite) GaN and cubic (zinc-blende) GaN will be briefly presented. This is followed by a review of a number of published results and data on growth, optical and electrical properties of cubic GaN.

2.1: CRYSTAL STRUCTURE

In general, the majority of group III-nitrides exist in two different types of crystal structures; wurtzite (hexagonal) and zinc-blende (cubic). The wurtzite structure is the thermodynamically stable phase under ambient condition. On the other hand, zinc-blende is a metastable structure and mainly forms when a film is grown on a cubic substrate, e.g. GaAs and 3C-SiC under carefully controlled conditions.

The wurtzite structure has a hexagonal unit cell, having two lattice constants; a and c while the zinc-blende structure is formed from a group of cubic unit cells and has a higher degree of crystallographic symmetry as its lattice constants are equal in three perpendicular directions. Figure 2.1 illustrates the arrangement of atoms in the wurtzite and zinc-blende structures. Clearly, both structures show that each group-III atom is coordinated by four nitrogen atoms and vice versa. Nonetheless, the stacking sequence of closest packed diatomic planes is different in the wurtzite and zinc-blende structures. The configuration of stacking sequence for (0001) plane in wurtzite is ABABAB in the $\langle 0001 \rangle$ direction, while the stacking sequence of (111) plane is ABCABC in the $\langle 111 \rangle$ direction in zinc-blende structure.

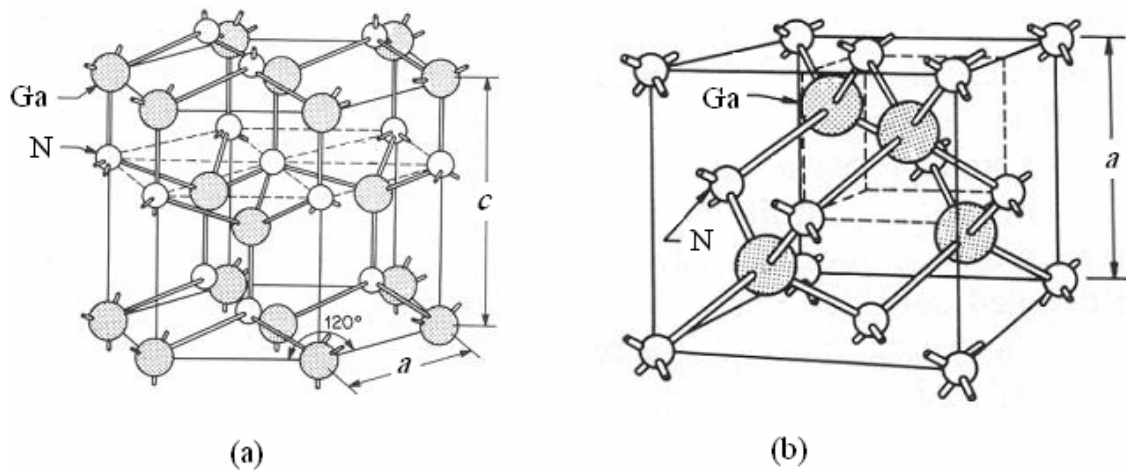


Figure 2.1: The atom arrangement in (a) wurtzite and (b) zinc-blende structures

The atomic arrangements are different in hexagonal and cubic GaN crystal phases. Hence, the basic physical properties for both structures would be expected to be different as well, and this will be discussed in the following section.

2.2: BASIC PROPERTIES OF III-NITRIDES

The basic properties for hexagonal and cubic III-nitride materials are shown in Table 2.1 and Table 2.2, respectively. The presented values are widely used in many works so far. As has been mentioned, the difference between the values in hexagonal and cubic nitride structures is due to the difference of the atomic arrangements in those phases. As the growth of cubic nitrides is challenging and samples for measurement are rare, there is the lack of some important data, like electron affinities.

Table 2.1: Basic properties of hexagonal GaN, AlN and InN at 300K.

Parameters	GaN	AlN	InN
Energy gap, E_g (eV)	3.39[1]	6.00 [2]	0.70-0.80 [3]
Electron affinity, χ (eV)	4.1 [4]	1.9 [5]	5.8 [6]
Effective electron mass, m_e	$\sim 0.22 m_0$ [7]	$0.35 m_0$ [8]	$0.07 m_0$ [9]
Effective hole mass (heavy), m_{hh}^{\parallel}	$1.27 m_0$ [10]	$2.04 m_0$ [10]	$1.56 m_0$ [10]
Effective hole mass (light), m_{lh}^{\parallel}	$1.27 m_0$ [10]	$2.04 m_0$ [10]	$1.56 m_0$ [10]
Lattice constant, a (\AA)	3.189 [11]	3.110 [11]	3.540 [11]
Lattice constant, c (\AA)	5.185 [11]	4.980 [11]	5.700 [11]

Table 2.2: Basic properties of cubic GaN, AlN and InN at 300K.

Parameters	GaN	AlN	InN
Energy gap, E_g (eV)	3.20 [12]	~ 5.10 [12]	0.56 [13]
Electron affinity, χ (eV)	-	-	-
Effective electron mass, m_e	$0.15 m_0$ [14]	$0.25 m_0$ [9]	$0.07 m_0$ [9]
Effective hole mass (heavy), m_{hh}	$0.80 m_0$ [10]	$1.20 m_0$ [10]	$0.84 m_0$ [10]
Effective hole mass (light), m_{lh}	$0.18 m_0$ [10]	$0.33 m_0$ [10]	$0.16 m_0$ [10]
Lattice constant, a (\AA)	4.500 [9]	4.380 [9]	4.980 [9]

Nearly all of these reports have used thin nitride layers (only few μm) in their studies. The reason is due to the lack of technology for growing high quality bulk cubic nitrides. Due to its metastable structure, large amounts of hexagonal inclusions inside the cubic material are expected even for thinner layers. This results in mixture phases that commonly lead to a serious problem in nitride crystal growth. For this reason, no data on bulk cubic GaN and substrates have been reported so far. If a cubic GaN layer is grown on a cubic GaN substrate, problems due to strain and defects are expected to be reduced. Consequently, study of the properties of cubic GaN would be more accurate and reliable. Besides this, there is considerable

commercial and scientific interest in cubic nitride based devices nowadays and therefore a high quality free standing bulk cubic (zinc-blende) GaN layer is urgently required. In this research, we intend to understand the key factors behind this issue of cubic nitrides growth. Once this knowledge is well understood, the problems of growing cubic GaN are tackled and high quality bulk cubic GaN and a substrate with low hexagonal inclusions will be demonstrated.

2.3: SUMMARY OF CUBIC GaN RESEARCH

Up to now, many attempts have been made to grow high quality cubic GaN, in particular to reduce the amount of hexagonal phase in the crystal structure. Commonly, cubic GaN has been characterised from optical and electrical measurements. In this section, a survey of literature data will be outlined, focusing mainly on growth, optical and electrical analysis of cubic GaN.

2.3.1: Studies of Cubic GaN growth

It is not easy to initiate the growth of cubic GaN. Therefore, it is necessary to grow the cubic layer on cubic substrates. To date, cubic GaN has been grown on cubic substrates such as GaAs and 3C-SiC [15-17]. In comparison to GaAs, the growth of cubic layers on 3C-SiC substrate has a smaller lattice mismatch, which is about 3.7% and therefore low dislocation density in the epitaxial layer is expected. However, high quality 3C-SiC substrates are not only costly but also hard to obtain. Hence, GaAs is a suitable substrate for nitride fabrications as it is a low cost and easily cleaved material even though it has a 20% mismatch to cubic GaN layers. Moreover, the main advantage of using GaAs substrates in our study is the ease of etching the substrate chemically from cubic GaN layers so that a free standing cubic GaN substrate is obtainable.

As has been mentioned above, it is difficult to initiate the growth of cubic GaN. However, it is even more difficult to sustain the growth of pure cubic GaN without any hexagonal inclusions forming inside the material. Cubic GaN is grown in the [100] direction. Due to thermodynamic instabilities, stacking faults in cubic GaN

structure may lead to the formation of hexagonal inclusions on (111) planes of cubic GaN [18]. However, a precise explanation for this behaviour is still not available.

In many reports, the percentage of hexagonal inclusions in cubic GaN is determined by X-ray diffraction (XRD) measurement, e.g. [18]. The authors had observed the XRD integrated intensities of the [002] cubic GaN peak and the $[10\bar{1}1]$ hexagonal GaN peak to estimate the percentage of hexagonal inclusions in cubic GaN. However, it should be noted that the peak at $\sim 35^\circ$ that relates to the hexagonal GaN could also be the result of (111) cubic GaN stacking faults. In earlier work at Nottingham, the average percentage of hexagonal inclusions in a bulk cubic GaN was found to be 10% by Nuclear Magnetic Resonance (NMR) measurement [16].

So far, cubic GaN samples have been grown using different growth techniques such as hydride vapour phase epitaxy (HVPE), metal organic vapour phase epitaxy (MOVPE) and molecular beam epitaxy (MBE). In 1999, Tsuchiya et al. [18] investigated the dependence of hexagonal fraction as HVPE cubic GaN thickness was increased. From their observation, the sample had a hexagonal fraction of about 10% at 5 μm thick and increased to approximately 40% at 10 μm . From this study, it was showed that the hexagonal inclusions in cubic GaN increase with thickness. Therefore, it is important to optimise the growth parameters for cubic GaN so that the amount of the hexagonal inclusions in the cubic GaN can be minimised.

Up to now, many studies reported that the amount of hexagonal inclusions varies with different V/III ratio, growth temperature, and growth rate. The growth diagram with the variation of V/III ratio is illustrated in Figure 2.2. This figure shows the dependence of Ga flux on substrate temperature for cubic (zinc-blende) GaN, as reported by Sung et al [19]. It defines three growth regimes at a constant N-flux (1×10^{-4} mbar). The open circles show the growth under Ga-rich condition, where the Ga droplets accumulate on the sample surface. The closed circles however indicate that there is no formation of excessive Ga on the surface. The boundary between Ga droplets (Ga-stable) and intermediate Ga-stable regimes is marked on the figure. On the intermediate Ga-stable regime, the Ga-flux was still found to be higher than the N-flux. Therefore, this regime can be further divided into two regimes that introduce the N-stable regime. The boundary between these conditions exhibits that Ga flux is

equal to N-flux, thus giving V/III ratio equivalents to unity (stoichiometric condition). The growth with higher N-flux is conducted below this boundary.

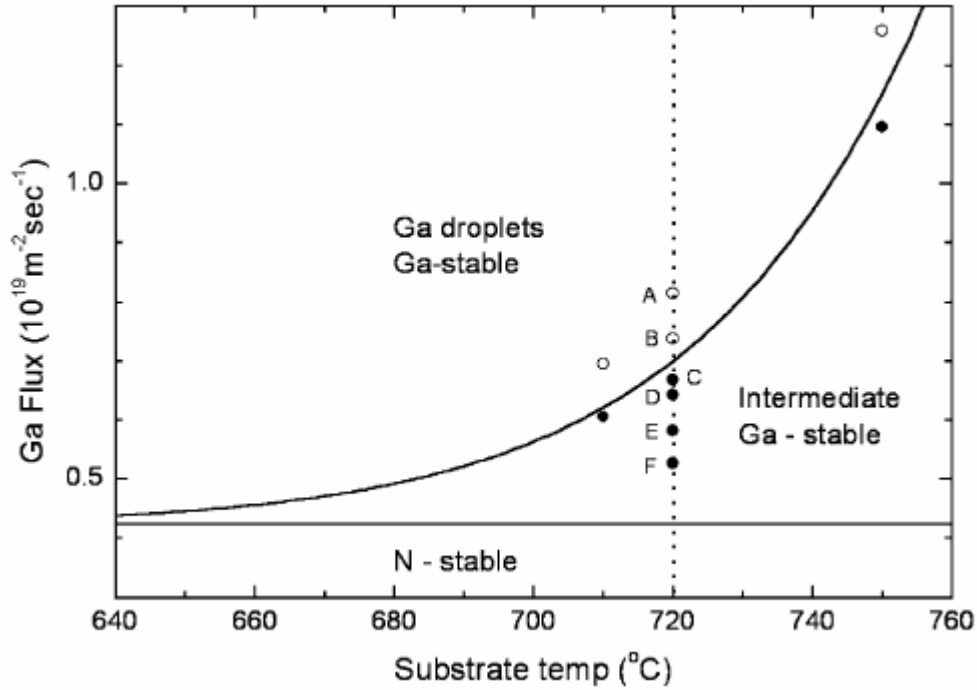


Figure 2.2: The growth diagram for cubic GaN grown by MBE. Three growth regimes under Ga stable, N stable and Ga droplets were defined with a constant N flux. The figure was taken from Sung et al [19].

Qin et al. suggested that epitaxy outside the stoichiometric condition disturbed the growth of cubic GaN [20]. Similar results had also been reported by other groups [18, 19, 21, 22]. Most authors suggested that the increase of the hexagonal fraction is correlated to the surface roughness, which could be due to higher nitrogen (N) flux. A surface analysis had been done by Tsuchiya et al. [18] and they found that cubic GaN samples with higher hexagonal fraction had a rougher surface as compared to ones with lower hexagonal fraction. Moreover, if cubic GaN was grown with higher Ga flux then Ga-droplets may form on the surface and this probably increases the hexagonal inclusions, as was observed in [19]. So far, this mechanism is poorly understood. Based on these reports, it is suggested that cubic GaN grows better under near-stoichiometric conditions. Nonetheless, it is a challenge to maintain this condition, especially for the growth of bulk cubic GaN as the Ga and N fluxes

change with time. In this work, we tried to find the solutions to maintain the optimum condition of V/III during longer growth so that a high quality bulk cubic GaN is possible.

The increase of hexagonal inclusions in cubic GaN as the growth rate changes is still not clearly understood. In fact, data relating to this subject is not widely reported so far. Daudin et al. [22] did a comparative study on MBE cubic GaN samples which were grown on SiC substrates at two different growth rates. From the measurement, it was found that faster growth increased the hexagonal fraction in the sample. In contrast, Funato et al. [23] reported that the amount of hexagonal in MOVPE cubic GaN on GaAs substrate was smaller at higher growth rate. The discrepancy of both results could be due to the different substrates and growth conditions used; like V/III ratio and temperature that lead to different amounts of hexagonal content in the measured samples. However, more results are required to clarify this behaviour and therefore will be demonstrated in this work.

Tsuchiya et al. [18] demonstrated that the hexagonal fraction in HVPE cubic GaN decreased when the growth temperature increased in the range of 700-825°C. A similar result had been observed in a MOVPE cubic GaN sample [21] within the temperature range of 750-950°C. The authors of [21] suggested that the migration of adatoms is inactive at low temperature, and therefore there is a weak interaction between GaN and buffer layer/substrate. Under this condition, GaN prefers to grow in the hexagonal phase. As the temperature increased, the interaction becomes stronger and more cubic material would be promoted into the GaN layer. Surface mobility now becomes higher and this may reduce the stacking faults and subsequently decreases the hexagonal fraction in the layer. Nevertheless, further increase in the temperature leads to higher desorption of Ga and N and therefore GaN is no longer grown. It should be noted that there might be a possibility that those authors were not aware of the variation of temperature distribution across the wafer during the growth. Such variation could lead to a variation of the density of hexagonal inclusions across the wafer and therefore will be investigated in this work.

It should be pointed out that the reviewed reports were limited to study of thin cubic GaN layers (up to a few μm). This is due to the problem of growing bulk cubic GaN,

which requires the maintenance of optimum growth conditions for longer growth periods. This is difficult due to the fluctuations of N and gallium (Ga) fluxes and temperature with time. Therefore, in this work, we intend to find solutions to stabilise those parameters so that the growth of bulk cubic GaN under optimum conditions can be sustained for longer periods.

Moreover, most of these studies only rely on one measurement technique; either XRD or PL measurements in order to investigate the dependence of hexagonal inclusions in cubic GaN. The problem with this is XRD is not sensitive to a very small amount of hexagonal material in the cubic sample. However, hexagonal PL gives stronger signal that considerably dominates the cubic PL. Therefore, in this work, we intend to use both techniques in order to observe the increase of hexagonal inclusions when the V/III ratio, growth rate and growth temperature are varied.

Table 2.3 summarises the list of the best reported cubic GaN samples in different studies. The table shows that the hexagonal fraction is already 10% for thin cubic GaN grown by HVPE and MOVPE. However, it has been demonstrated that there is negligible hexagonal phase in thin molecular beam epitaxy (MBE) cubic GaN samples [24, 25]. Therefore, MBE is probably the best method to grow cubic GaN and will be demonstrated in this work.

Table 2.3: The best reported cubic GaN layers grown under optimum growth conditions in different studies.

Growth Method	Substrate	Thickness of GaN (μm)	Hexagonal fraction (%)	Growth temperature ($^{\circ}\text{C}$)	Growth rate ($\mu\text{m/hr}$)	Total V/III ratio	References
HVPE	GaAs	5.00	10.0	800	~2.00	200	[18]
MOVPE	3C-SiC	2.50	~7.5	850	0.83	500	[26]
MOVPE	3C-SiC	1.00	9.0	950	1.50	1500	[21]
MOVPE	GaAs	1.00	10.0	900	3.00	10	[27]
MOVPE	GaAs	0.35	10.0	850-900	1.05	25	[23]
MBE	GaAs	0.8	<2	710	0.072	100	[24]
MBE	GaAs	8	-	680	0.3	100	[25]

In this work, the properties of cubic GaN are investigated through optical and electrical measurements. Therefore, the subsequent sections will outline the literature survey for optical and electrical analysis of cubic GaN.

2.3.2: Optical Studies of Cubic GaN

Previously, the optical properties of cubic GaN have been studied using various techniques, like photoluminescence (PL), cathodoluminescence (CL), Raman scattering and photoreflectance (PR). In most reports, the optical properties of cubic GaN are observed at low temperature as the effect of crystal lattice vibrations is negligible.

Before we go to a further discussion of the reported results on the optical characteristic of cubic GaN, it is useful for the reader to understand a typical PL spectrum of cubic GaN, as shown in Figure 2.3. The spectrum was taken from our measurement. Clearly, there are three peaks that could be attributed to the optical process in cubic GaN. The origin of the peak at $\sim 3.10\text{eV}$ may associate to a free to bound excitonic recombination at an additional acceptor level in cubic GaN [28]. Meanwhile, the peaks at $\sim 3.15\text{eV}$ and $\sim 3.25\text{eV}$ are probably due to donor-acceptor (DA) pair transitions and excitonic emissions in cubic GaN, respectively. Nevertheless, these peak emissions may vary in different samples and experiments, as has been reported by various researchers.

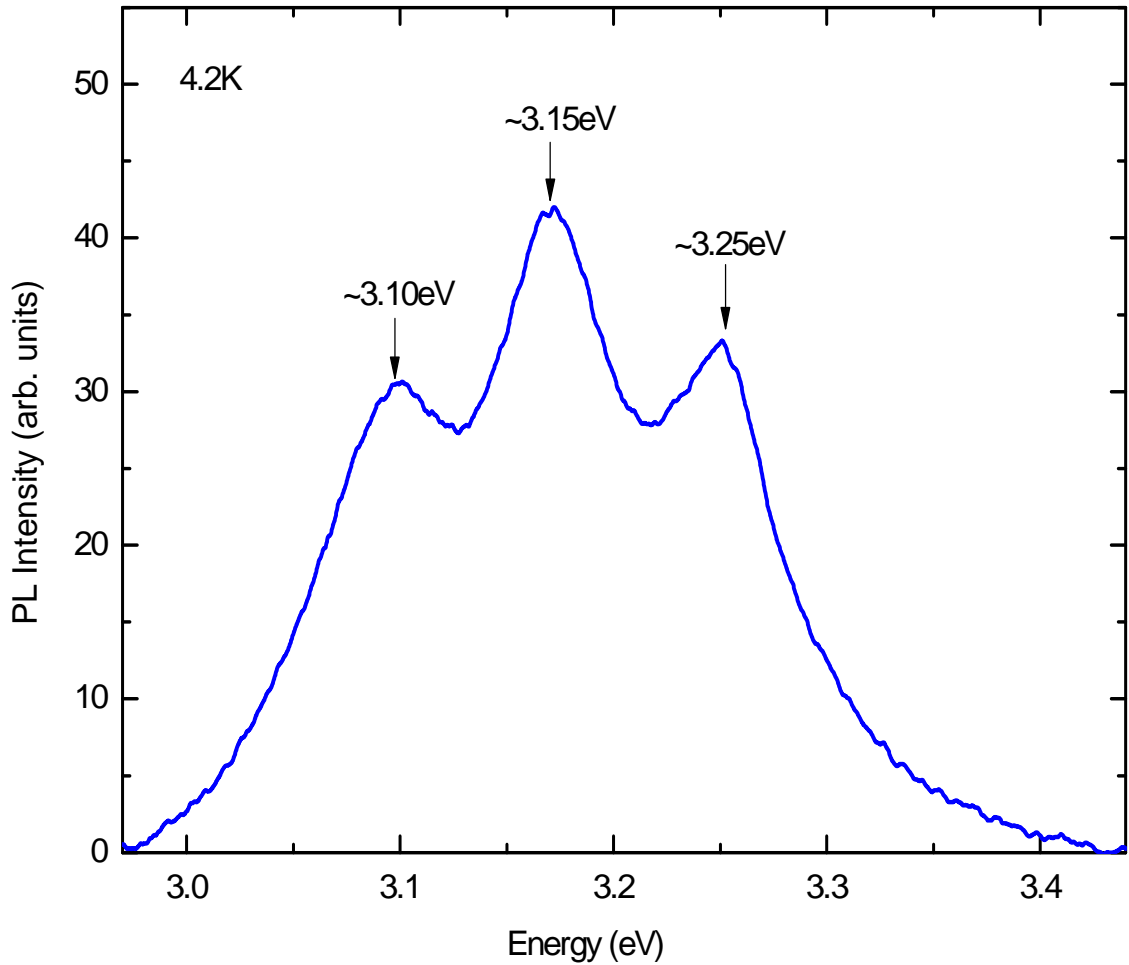


Figure 2.3: A typical PL spectrum for a thin ($\sim 0.8\mu\text{m}$) cubic GaN layer measured at 4.2K. This spectrum was taken from our measurement.

Early CL measurements on a cubic GaN layer reported that the emission lines at 3.267 and 3.183eV corresponded to free electron-bound hole (eA) and donor-acceptor (DA) pair recombinations, respectively [29]. However, the peak energy for eA should be doubted as the authors only speculated the source of the peak by comparing their data with the results in hexagonal GaN [30, 31]. A few years later, the formation of cubic GaN single crystals (micron-size) was observed on the surface of a GaN layer [32]. From CL measurement, the cubic GaN crystals exhibited the emission lines at 3.272 and 3.263eV, which were attributed to the recombination of free exciton (FX) and bound exciton (BX), respectively. Apart from that, the peak energy of DA pair transitions appeared at 3.150eV.

On the other hand, As et al [24] demonstrated that the reduction of Ga-flux helps to suppress the formation of micro-crystals, resulting in smooth and uniform cubic GaN epilayers. In their sample, the peak energies of excitonic and *DA* pair recombinations were observed at 3.26 and 3.15eV, respectively. The peak intensity of the *DA* pair transitions was found to be higher than that of the excitonic recombinations, indicating the possibility of a high impurity density in the sample. The temperature dependence for the peak at 3.15eV had also been investigated. As the temperature increased, a second peak begun to appear at higher energy and subsequently became dominant above 45K. This shows that the *DA* pair transitions turned into free electrons to acceptor level transitions (*eA*) as the ionisation of donors increased at higher temperatures.

In another experiment [28], the PL spectrum for cubic GaN showed that there were four resolved peaks at 3.274, 3.178, 3.088 and 3.056eV, and no emission signal above 3.30eV, which would correspond to hexagonal GaN. The first two peaks were attributed to excitonic and *DA* pair recombinations in cubic GaN. Both emissions occurred at the shallow acceptor level (E_A) of around 90meV. On the other hand, the emission lines at 3.088 and 3.056eV were suggested to correspond to *eA* and *DA* pair transitions that could have originated from the additional acceptor level (E_A') at about 212meV. At room temperature, the peak at 3.274eV shifted to lower energy (3.216eV) due to the variation of interband transitions with temperature, which has been derived from the Varshni empirical equation [33].

Philippe et al [34] identified the peak emission at 3.265eV as excitonic recombinations in cubic GaN. This peak however shifted to lower energy as the temperature increased. Again, this can be explained by the Varshni empirical equation [33]. The peak energies of *DA* pair and *eA* transitions were also observed around 3.130 and 3.150eV, respectively. The signal of the *DA* pair transitions however, became less dominant as the temperature increased. This implies that the *DA* pair transitions starts to transform to *eA* transitions at higher temperature.

They also demonstrated that p- and n-type cubic GaN could be achieved by controlling the III/V ratio. From the measurement, the *eA* transitions were enhanced when the cubic GaN layer was grown with lower III/V ratio. This showed that the

acceptor concentration was higher and therefore p-type cubic GaN could be achieved under slightly N-rich condition. On the other hand, the signal of BX recombinations became important at higher III/V ratio, indicating the increase of donor concentration. Therefore, cubic GaN should be grown under slightly Ga-rich conditions to get n-type behaviour. These observations are consistent with those reported by As et al. [35, 36].

In 2001, Xu et al studied lightly Magnesium (Mg) doped cubic GaN epilayers [37]. From the PL spectra, two strong emission lines had been detected at 3.269 and ~ 3.15 eV and they corresponded to BX recombinations and *DA* pair recombinations, respectively. The variation of emission energy of *eA* with temperature revealed that there was one shallow donor and two shallow acceptor levels in cubic GaN. They suggested that the Mg and Carbon (C) were the possible acceptors that contributed to the *DA* pair transitions at the acceptor level of 144meV. However, they did not comment on the origin of the second acceptor level at 71meV.

In another experiment, GaN films had been studied by XRD and PL measurements [38]. There was a weak XRD signal of cubic GaN even though the spectrum was governed by a strong signal from hexagonal. This XRD result suggested that cubic GaN had crystallised in a hexagonal matrix. In fact, the authors elucidated that the weak cubic GaN signal can be due to cubic grains at the GaN/GaAs interface or maybe a random contribution from the small cubic inclusions throughout the films. In contrast, the emission peak from cubic was more significant than hexagonal in the PL spectrum. This was attributed to the effective localization of photo-generated carriers at lower bandgap of cubic GaN. From the PL spectrum, it showed that the peak energy for donor-bound exciton (BX) and *DA* pair recombinations were 3.26eV and 3.16eV, respectively.

Table 2.4 summarises the published data for the optical properties of cubic GaN at low temperature. In general, the excitonic emission peak (which contains overlapped peaks from free exciton (FX) and bound exciton (BX) recombinations) is observed in a range of 3.26 to 3.27eV. Due to large full width at half maximum (FWHM), FX and BX cannot be resolved in some measurements. The signal of *DA* pair transitions appeared in all experiments because the recombination at state levels that donated

from doping or impurities is important at low temperature. The peak energy for *DA* pair transitions in cubic GaN had been reported in between 3.13 and 3.18eV. On the other hand, it is quite difficult to observe the peak energy of the free to bound transition, *eA* at low temperature since the loosely bound electrons at donor levels are less likely to be promoted into the conduction band. The discrepancy of the data values in different experiments may be caused by several reasons. Firstly, it is due to the variety of the hexagonal inclusions, where some broad emissions in the hexagonal GaN may shift the peak emissions in cubic GaN. This mechanism will be discussed in more detail later. Secondly, the lattice mismatch between cubic GaN and substrates introduces the strain, which consequently forms defects in the cubic GaN layers. The defects will create some additional levels in the electronic states of cubic GaN, hence change the position of the peak emissions in cubic GaN. A similar mechanism also takes place when impurities are introduced unintentionally in the cubic material during the growth.

Table 2.4: The reported optical properties in cubic GaN at low temperature.

Method	Temperature (K)	Free Exciton (eV)	Bound Exciton (eV)	FWHM (meV)	Free to bound transition (eV)	<i>DA</i> pair transition (eV)	References
CL	4	-	-	-	3.267	3.183	[29]
CL	5	3.272	3.263	8.0	-	3.150	[32]
PL	2	3.260		24.0	3.150	-	[24]
PL	6	3.274		15.0	3.178 3.088	- 3.056	[28]
PL	N/A	3.260		17.0	3.170	-	[39]
PL	9	3.265		13.7	3.150	3.130	[34]
PL	3.5	-	3.269	12.0	-	3.150	[37]
PL	10	-	3.260	-	-	3.160	[38]

As been mentioned before, hexagonal inclusions can be easily formed in cubic GaN. Thus, even a minimal amount of hexagonal inclusions could give a strong PL signal and suppress the luminescence from cubic material. This is inconsistent with what had been reported in Ref [38] but it has been experimentally observed [39, 40]. The reason is probably due to the fact that hexagonal GaN can be more easily crystallized

in a much better structure¹ as compared to cubic GaN and therefore it gives significant signal in PL spectra. The existence of hexagonal inclusions in cubic GaN is observed in Figure 2.4. This figure shows PL spectrum for a thick (~1.9 μ m) cubic GaN layer. Obviously, the excitonic emissions in hexagonal GaN can be seen around 3.42eV. On the other hand, the overlap of two broad signals from hexagonal and cubic GaN appears at lower energy side, which is about 3.28eV. It should be noted that commonly the *DA* pair transitions in hexagonal GaN also occurs at ~3.25eV and thus they are overlapped with the signal of excitonic emissions in cubic GaN.

In order to address this issue, we also propose to characterise our cubic GaN samples by XRD measurement. Data from both PL and XRD measurements are then analysed to observe the evidence of hexagonal and cubic phases in the cubic GaN samples. In this work, the dependence of hexagonal inclusion in cubic GaN with the variation of V/III ratio, growth rate, growth temperature and others are investigated by PL measurement.

¹ The crystal quality of hexagonal GaN in cubic GaN had been measured in [41]

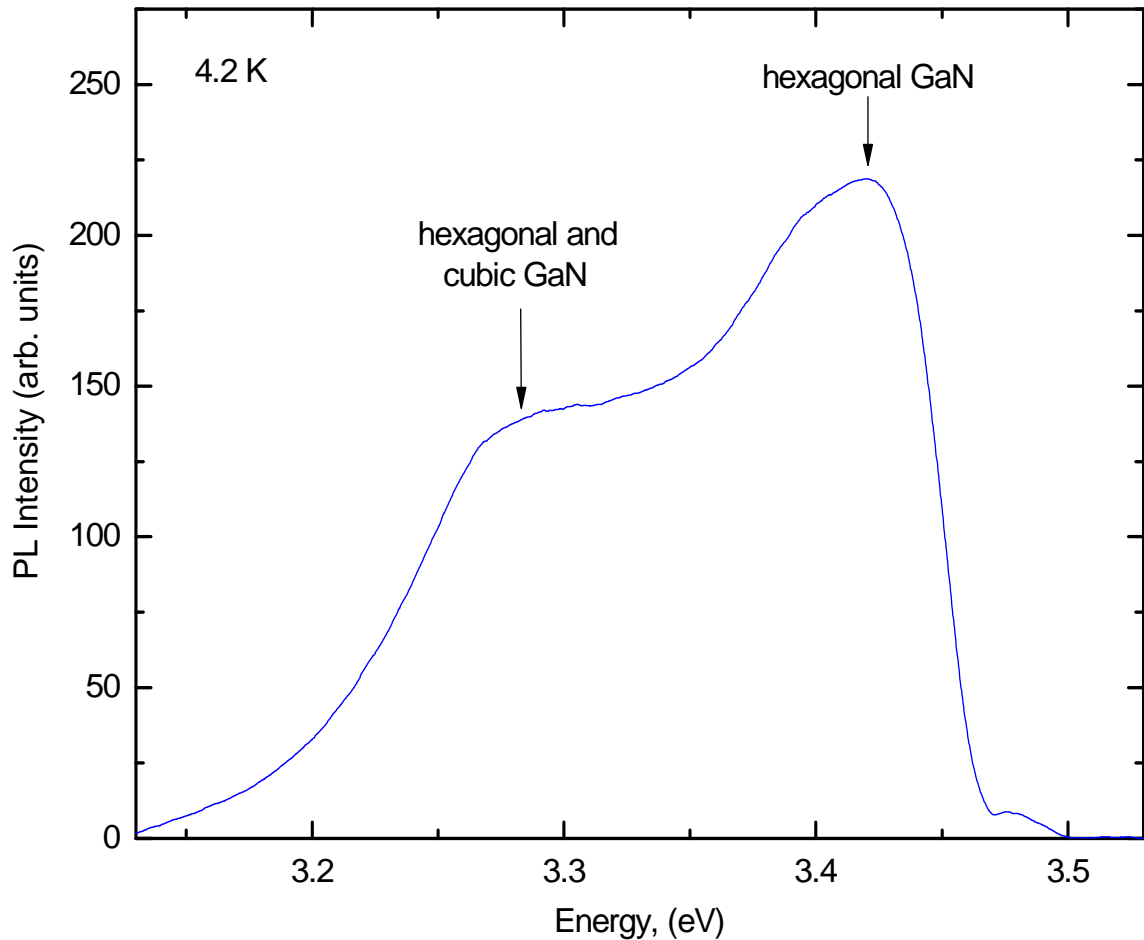


Figure 2.4: A typical PL spectrum for a thick ($\sim 1.9\mu\text{m}$) cubic GaN layer measured at 4.2K. This spectrum was taken from our measurement.

2.3.3: Electrical Studies of Cubic GaN

Adding dopants in semiconductor material is an essential process to achieve controlled electrical performance in device applications. When a dopant is introduced, the electrical properties in the material will be changed as the dopant forms an additional level closer to conduction or valence band. The semiconductor has p-type conductivity if the level is located near the valence band (acceptor level), whereas it has n-type conductivity if the level is formed near the conduction band (donor level). The distance of the level from the band can influence the efficiency of the p- and n-type conductivity in the materials. Hence, controlling the doping profile in semiconductor material is required in order to achieve a variety of device structures.

Traditionally, n-type undoped GaN was attributed to background nitrogen vacancies inside the material [42, 43]. However, the presence of Oxygen (O) impurities during the growth is more likely to be associated to the formation of n-type GaN. In this process, the O atoms may occupy the nitrogen sites during the process and create a donor level at about 29meV [44]. An optical study by Andrianov et al. found that there was an emission peak in PL spectra that may relate to the presence of O in a GaN film [45]. As et al reported that without intentional doping, p- and n-type cubic GaN could be obtained by careful adjustment of III/V ratio within the stoichiometric growth range [36]. The growth under N-rich and Ga-rich conditions, which results in p- or n-type GaN cubic layers had been achieved by controlling the surface reconstruction using *in situ* reflection high energy electron diffraction (RHEED). At this stage, N-rich or Ga-rich growth gives different defect densities that influence the electronic states in cubic GaN.

Magnesium (Mg) is conventionally used for p-type cubic GaN. However, Mg dopants shows several disadvantages such as self-compensation, segregation and solubility effects as they have a large acceptor ionization energy and are very volatile [46]. This degrades the doping efficiency and crystalline quality of the cubic layer [47]. Another alternative to Mg is Carbon (C), which is similar to nitrogen (N) in terms of atomic radius and electronegativity. When C atoms substitute for the N atoms, they may create a shallow acceptor level that leads to p-type conductivity.

In hexagonal GaN, C forms a deep level within the forbidden gap and thus results in an insulating material. On the other hand, C doped cubic GaN layers were found p-type when grown under Ga-rich conditions with a maximum hole concentration of $6 \times 10^{18} \text{cm}^{-3}$ and hole mobility of $19 \text{cm}^2/\text{Vs}$ at room temperature [48]. This report suggested that the excess Ga during the growth process forces the C atoms to be incorporated at N-sites leading to the formation of p-type material.

So far, there have been a few reports on Mn doped cubic GaN. Theoretical studies suggested that the Mn level is too deep in GaN and therefore p-type GaN:Mn is hardly observed in some experiments [49, 50]. However, Novikov et al [51] had achieved highly reproducible Mn doping in cubic GaN. The hole density was found to be about 10^{18}cm^{-3} with a corresponding hole mobility of $>300 \text{cm}^2/\text{Vs}$ under Ga-

rich and N-rich conditions. It is important to confirm that the p-type behaviour in cubic GaN is coming from the Mn dopants, not from unintentional doping of the GaAs buffer layer by Mn or other impurities. Another issue is to verify that the p-type doping in the GaMnN layer is associated with Mn in the GaN, but not from unintentional doping of the GaMnN by other impurities such as C or Mg.

To clarify these issues, a sample with an additional structure (about 150nm undoped cubic GaN grown on an insulating cubic AlN layer (50-150nm)) had been inserted between the cubic GaMnN and GaAs substrate. This was to ensure that the diffusion of Mn into the substrate was prohibited. The electrical properties of this sample were compared to the sample without the additional structure. It was found that both samples had similar hole densities and showed p-type behaviour. Thus, the result indicates that the p-type conductivity arises from Mn doping in cubic GaMnN films.

Additionally, SIMS measurements for undoped cubic GaN and GaMnN films had also been carried out. From the SIMS result, the unintentional doping of O and C levels were found to be similar for both structures. Moreover, the doping level of O and C did not change systematically with Mn concentration. These results confirm that Mn in cubic GaMnN is responsible for p-type conductivity for the film. In cubic GaN, the ionisation energy for Mn is found to be approximately 50meV, which is much shallower than for C and Mg. This shows that Mn is a preferable p-type dopant in cubic GaN compared to C.

Commonly, n-type cubic GaN is achieved by Silicon (Si) doping. In principle, Si atoms incorporate at Ga-sites and act as shallow donors in the material. As et al had characterised Si-doped cubic GaN samples through Hall Effect measurement [52]. Their analysis revealed that the maximum free electron concentration and mobility were $5 \times 10^{19} \text{ cm}^{-3}$ and $75 \text{ cm}^2/\text{Vs}$, respectively.

Martinez-Guerrero et al [53] demonstrated that the free electron concentration in Si-doped cubic GaN increased linearly with Si concentration. The mobility was about $170\text{-}50 \text{ cm}^2/\text{Vs}$ for doping concentration in the range of 3×10^{18} to $4 \times 10^{19} \text{ cm}^{-3}$. From PL measurement, it was found that the DA pair transition dominated the spectra. This peak however was broadened and shifted towards higher energy when the Si-cell

temperature was increased. This can be explained by the fact that the Si donor level moves closer to the conduction band as the Si concentration is increased. Consequently, the distance between the donor and acceptor levels increases and leads to higher energy emission.

It is well known that epitaxially grown cubic GaN suffers from residual strain and defects due to the use of a non-lattice matched substrate. These effects modify the electrical properties of the samples and leads to large data discrepancy in the literature. Furthermore, these effects are different for different growth methods, which could influence the electrical characteristic of cubic GaN. In this work, we intend to study the electrical properties of undoped cubic GaN samples grown by different growth techniques. Longer growth operation may lead to fluctuation in V/III ratio and temperature. Consequently, the electrical properties of cubic GaN may also change with thickness. This issue will be addressed in this work. Apart from that, the doping efficiency in cubic GaN is also investigated by introducing different dopants in the layer.

2.4: CONCLUSIONS

The discussion so far has summarised the basic properties and important data for both hexagonal and cubic nitrides. As this thesis focuses on cubic GaN, the current state of the art on the growth, optical and electrical properties of the structure have been outlined. In this work, we aim to produce high quality bulk cubic GaN with low hexagonal fraction by carefully calibrating the growth parameters such as V/III ratio, growth rate and temperature at optimum condition. With the available bulk cubic GaN, further investigations of the fundamental properties of cubic GaN would be possible. In this work, we also develop a procedure to process the bulk cubic GaN sample to make it as a commercial substrate for device applications.

REFERENCES

1. S. Nakamura, *Science*, (1998). **281**: p. 956.
2. E. Silveira, J.E. Freitas, B. Schujman, L.J. Schpwalter, *J. Cryst. Growth*, (2008). **310**: p. 4007.
3. J. Wu, W. Walukiewicz, K.M. Yu, J.W. Ager III, E.E. Haller, Hai Lu, W. J. Schaff, Y. Saito, Y. Nanishi, , *Appl. Phys. Lett.*, (2002). **80**: p. 3967.
4. S. Arulkumaran, T. Egawa, H. Ishikawa, T. Jimbo, M. Umeno, *Appl. Phys. Lett.*, (1998). **73**: p. 809.
5. C.I. Wu, A. Kahn, *Appl. Phys. Lett.*, (1999). **74**: p. 546.
6. W. Walukiewicz, J.W. Ager III, K.M. Yu, Z. Liliental-Weber, J. Wu, S.X. Li, R.E. Jones, J.D. Denlinger, *J. Phys. D: Appl. Phys.*, (2006). **39**: p. R83.
7. A.M. Witowski, K. Pakula, J.M. Baranowski, M.L. Sadowski, P. Wyder, *Appl. Phys. Lett.*, (1999). **75**: p. 4154.
8. K. Kim, W.R.L. Lambrecht, B. Segall, M. Van Schifgaarde, *Phys. Rev. B*, (1997). **56**: p. 7363.
9. I. Vurgaftman, J.R. Meyer, *J. Appl. Phys.*, (2003). **94**: p. 3675.
10. S.K. Pugh, D.J. Dugdale, S. Brand, R.A. Abram, *Semicond. Sci. Technol.*, (1999). **14**: p. 23.
11. S.J. Perton, C.R. Abernathy, M.E. Overberg, G.T. Thaler, D.P. Norton, N. Theodoropoulou, A.F. Hebard, Y.D. Park, F. Ren, J. Kim, L.A. Boatner, *J. Appl. Phys.*, (2003). **93**: p. 1.
12. T. Suzuki, H. Yaguchi, H. Okumura, Y. Ishida, S. Yoshida, *Jpn. J. Appl. Phys.*, (2000). **39**: p. L497.
13. J. Schörmann, D.J. As, K. Lischka, P. Schley, R. Goldhahn, S.F. Li, W. Löffler, M. Hetterich, H. Kalt, *Appl. Phys. Lett.*, (2006). **89**: p. 261903.
14. M. Fanciulli, T. Lei, T.D. Moustakas, *Phys. Rev. B*, (1993). **48**: p. 15144.
15. R. Kimura, A. Shigemori, J. Shike, K. Ishida, K. Takahashi, *J. Cryst. Growth*, (2003). **251**: p. 455.
16. S.V. Novikov, N.M. Stanton, R.P. Campion, R.D. Morris, H.L. Geen, C.T. Foxon, A.J. Kent, *Semicond. Sci. Technol.*, (2008). **23**: p. 015018
17. J. Suda, T. Kurobe, S. Nakamura, H. Matsunami, *Jpn. J. Appl. Phys.*, (2000). **39**: p. L1081
18. H. Tsuchiya, K. Sunaba, T. Suemasu, F. Hasegawa, *J. Cryst. Growth*, (1999). **198/199**: p. 1056.
19. L.W. Sung, H.H. Lin, C.T. Chia, *J. Cryst. Growth*, (2002). **241**: p. 320.
20. Z. Qin, M. Kobayashi, A. Yoshikawa, *J. Materials Science: Materials in Electronics*, (1999). **10**: p. 199.
21. C.H. Wei, Z.Y. Xie, L.Y. Li, Q.M. Yu, J.H. Edgar, *J. Electronic Materials*, (2000). **29**: p. 317.
22. B. Daudin, G. Feuillet, J. Hubner, Y. Samson, F. Widmann, A. Philippe, C. Bru-Chevallier, G. Guillot, E. Bustarret, G. Bentoumi, A. Deneuve, *J. Appl. Phys.*, (1998). **84**: p. 2295.
23. M. Funato, M. Ogawa, T. Ishido, Sz. Fujita, *Phys. Stat. Sol. (a)* (1999). **176** p. 509
24. D.J. As, F.S.C. Wang, B. Schttker, K. Lischka, *Appl. Phys. Lett.*, (1997) **70** p. 1311.
25. S.V. Novikov, N.M.S. R.P. Campion, C.T. Foxon, A.J. Kent, *J. Cryst. Growth*, (2008). **310**: p. 3964.

26. J. Camassel, P. Vicente, N. Planes, J. Allegre, J. Pankove, F. Namavar, *Phys. Stat. Sol. (b)*, (1999). **216**: p. 253.
27. J. Wu, H. Yaguchi, K. Onabe, Y. Shiraki, R. Ito, *Jpn. J. Appl. Phys.*, (1998). **37**: p. 1440.
28. J. Wu, H. Yaguchi, K. Onabe, R. Ito, Y. Shiraki, *Appl. Phys. Lett.*, (1997). **71**: p. 2067.
29. S. Strite, J. Ruan, Z. Li, A. Salvador, H. Chen, D.J. Smith, W.J. Choyke, H. Morkoc, *J. Vac. Sci. Technol. B*, (1991). **9** p. 1924
30. R. Dingle, M. Ilegems, *Solid State Communications*, (1971). **9**: p. 175.
31. R. Dingle, D., D. Sell, S.E. Stokowski, M. Ilegems, *Phys. Rev. B*, (1971). **4**: p. 1211.
32. J. Menninger, U. Jahn, O. Brandt, H. Yang, K. Ploog, *Phys. Rev. B Phys. Rev. B*, (1996). **53**: p. 1881.
33. Y.P. Varshini, *Physica (Amsterdam)* (1967). **34**: p. 149.
34. A. Philippe, C.B.-C. M. Vernay, G. Guillot, J. Hübner, B. Daudin, G. Feuillet, *Material Science and Engineering B* (1999). **59** p. 168.
35. D.J. As, D. Schikora, A. Greiner, M. Lübbbers, J. Mimkes, K. Lischka, *Physical Review B* (1996). **54**: p. R11118.
36. D.J. As, K. Lischka, *Phys. Stat. Sol. (a)* (1999). **176** p. 475.
37. S.J. Xu, C.T. Or, Q. Li, L.X. Zheng, M.H. Xie, S.Y. Tong, Hui Yang, *Phys. Stat. Sol. (a)* (2001). **188**: p. 681,.
38. O. Maksimov, Y. Gong, H. Du, P. Fisher, M. Skowronski, I.L. Kuskovsky, V.D. Heydemann, *Vacuum* (2006). **80**: p. 1042.
39. G. Feuillet, F. Widmann, B. Daudin, J. Schuler, M. Arley, J.L. Rouviere, N. Pelekonos, O. Briot, *Materials Science and Engineering B*, (1997). **50**: p. 233.
40. G. Ramírez-Flores, H. Navarro-Contreras, A. Lastras-Martínez, R. C. Powell, J.E. Greene, *Physical Review B*, 1994. **50**(12): p. 8433.
41. S.V. Novikov, N. Zainal, A.V. Akimov, C.R. Staddon, A.J. Kent, C.T. Foxon, *J. Vac. Sci. Technol. B*, (2010). **28**: p. 3.
42. K. Saarinen, P. Seppälä, J. Oila, P. Hautojärvi, C. Corbel, O. Briot, R.L. Aulombard, *Appl. Phys. Lett.* , (1998). **73**: p. 3253.
43. William E. Fenwick, A. Asghar, Shalini Gupta, Hun Kang, Martin Strassburg, Nikolaus Dietz, Samuel Graham, Matthew H. Kane, Ian, T. Ferguson, *J. Vac. Sci. Technol. A*, (2006). **24**: p. 1640
44. J.C. Zolper, R.G. Wilson, S.J. Pearton, R.A. Stall, *Appl. Phys. Lett.*, (1998). **68**: p. 1945.
45. A.V. Andrianov, D.E. Lacklison, J.W. Orton, D.J. Dewsnip, S.E. Hooper, C.T. Foxon, *Semicond. Sci. Technol.*, (1996). **11**: p. 366.
46. U. Kaufmann, P. Schlotter, H. Obloh, K. Köhler, M. Maier, *Phys. Rev. B*, (2000). **62**: p. 10867.
47. E. Martinez-Guerrero, E. Bellet-Amalric, L. Martinet, G. Feuillet, B. Daudin, H. Mariette, P. Holliger, C. Dubois, P. Aboughe Nze, T. Chassagne, G. Ferro, Y. Monteil, *J. Appl. Phys.*, (2002). **91**: p. 4983
48. D.J. As, D.G. Pacheco-Salazar, S. Potthast, K. Lischka, *Phys. Stat. Sol. (c)* (2003). **0**: p. 2537.
49. J.D. Albrecht, J.E. Van Nostrand, B. Claflin, Y. Liu, M.I. Nathan, P.P. Ruden, *J. Superconductivity: Incorporating Novel Magnetism*, (2005). **18**: p. 69
50. C.H. Choi, S.H. Kim, M.H. Jung, *Journal of Magnetism and Magnetic Materials*, (2009). **321**: p. 3833.

51. S.V. Novikov, K.W. Edmonds, L.X. Zhao, A.D. Giddings, K.Y. Wang, R.P. Champion, C.R. Staddon, M.W. Fay, Y. Han, P.D. Brown, M. Sawicki, B.L. Gallagher, C.T. Foxon, *J. Vac. Sci. Technol. B*, (2005). **23**: p. 1294.
52. D.J. As, D. Schikora, K. Lisicka, *Phys. Stat. Sol. (c)* (2003). **0**: p. 1607.
53. E. Martinez-Guerrero, B. Daudin, G. Feuillet, H. Mariette, Y. Genuist, S. Fanget, A. Philippe, C. Dubois, C. Bru-Chevallier, G. Guillot, P. Aboughe Nze, T. Chassagne, Y. Monteil, H. Gamez-Cuatzin, J. Tardy, *Materials Science and Engineering B*, (2001) **82**: p. 59

CHAPTER 3: SAMPLE PREPARATION AND EXPERIMENTAL TECHNIQUES

This chapter presents detailed descriptions of sample preparation and experimental techniques that were used to fabricate and characterise samples. Problems encountered during the measurements are also highlighted and discussed. In this project, most of the work has been carried out within the University of Nottingham.

3.1: SAMPLE GROWTH

Previously, in Chapter 2, I have discussed the issues related to growing cubic GaN, where the growth parameters like V/III ratio, growth rate and growth temperature play the main role in improving the quality of cubic materials and in particular reducing hexagonal content. In view of this, special techniques are required to achieve the optimal growth conditions for cubic GaN.

In this project, cubic nitride samples were grown on (001) GaAs substrates by Dr. Novikov using molecular beam epitaxy (MBE) Gen-II system. Additional arsenic flux was introduced to initiate the growth of cubic GaN on the substrate. This is because arsenic is a good surfactant to promote the growth of cubic materials [1, 2]. The CARS25 RF-activated plasma source was used to supply the active nitrogen for growing the III-nitride materials. In parallel, the source of gallium (Ga), aluminium (Al), indium (In), silicon (Si), Manganese (Mn) and carbon (C) were produced from conventional solid effusion cells. The growth temperature was measured by using an optical pyrometer and the growth rate was calibrated using a post growth reflectivity technique in order to measure the sample thickness with growth time. A further explanation about this technique can be found in [3].

In this work, we attempt to grow the cubic GaN samples under stoichiometric conditions. It is difficult to maintain this condition, especially for long growth times, because of the following problems; (1) drift of the Ga flux due to depletion of Ga cell, (2) drift of active nitrogen (N) flux as the efficiency of the N plasma become

unstable at longer growth times and (3) the gradual change in the heat transfer from the GaAs substrate to GaN layer as the thickness increases, which lead to a slow drift of the growth temperature. To address this problem, the MBE system was re-calibrated for each growth run and several thin GaN samples were grown for this purpose.

3.2: PROCESSING CUBIC GaN SUBSTRATES

In the effort to produce free standing cubic GaN substrates, the first thing that needs to be done is to remove the GaAs from cubic GaN layer. In this work, the samples ($10 \times 10 \text{mm}^2$) were carefully mounted on a special ceramic using low temperature wax, as shown in Figure 3.1(a). The GaAs substrate was placed on the top side and was removed by a chemical solution bath, $\text{H}_2\text{O}_2:\text{H}_3\text{PO}_4$. Through this process, free standing cubic GaN substrates were obtained.

However, the strain due to lattice mismatch between GaN and GaAs generates defects near the interface. Therefore, after the etching process, the free standing cubic GaN substrates were polished in order to remove the defective materials on the surface. At the first stage of this polishing work, the cubic substrate that had been attached to the ceramic plate was mounted on the polishing jig, as in Figure 3.1(b). Then, the substrates were polished using a cloth polishing lap together with SF1 liquid (a chemical-mechanical polishing compound which contains colloidal silica particles $\sim 20 \text{nm}$ in a caustic solution). The process is shown Figure 3.1(c). During this process, the polishing lap and polishing jig are continuously rotating. The speed of the rotations is controlled by a speed controller. On top of that, we put some weights on the polishing jig to increase the pressure of the sample on the lap which increases the polishing rate, but too much pressure can lead to cracking of the sample. The optimum pressure is determined empirically.

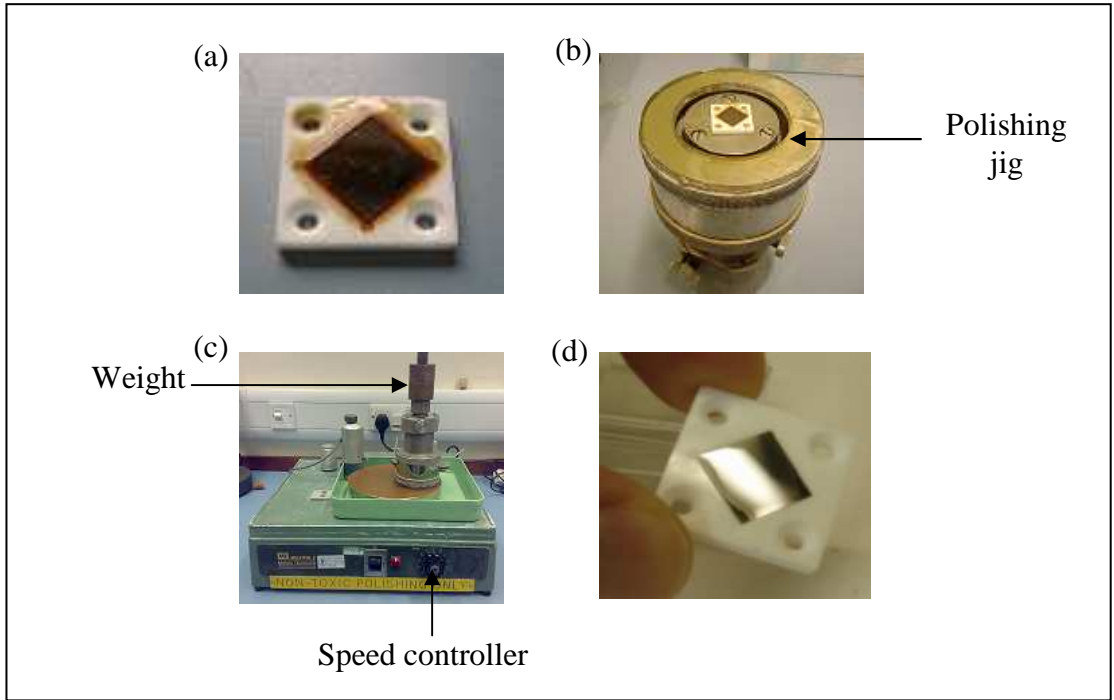


Figure 3.1: (a) Cubic GaN was placed on ceramic plate by low temperature wax. (b) Free standing cubic GaN was mounted on the polishing jig. (c) The sample was polished by the chemical-mechanical polishing machine. (d) Free-standing cubic GaN after polishing.

It is important to use the right parameters in the polishing process. Faster polishing with larger weight would crack the sample. On the other hand, slower polishing with smaller weight would take many hours to remove some micrometers from the layer. For this reason, we polished several cubic samples with different polishing parameters so that we can find the optimum polishing rate for cubic GaN substrate. From this work, we found that the optimum weight is about 2kg with the optimum polishing speed at ~ 2 rpm.

The polishing rate was then estimated. In this work, three thick cubic GaN samples were polished. Sample 1 and 2 are cubic GaN samples with a thickness of $\sim 7\mu\text{m}$ while sample 3 is $\sim 12\mu\text{m}$. Figure 3.2 shows the reduction in thickness of the samples as a function of polishing time. Apparently, the depth of material removed increases almost linearly with time and the polishing rate is roughly $3\mu\text{m}/\text{hour}$.

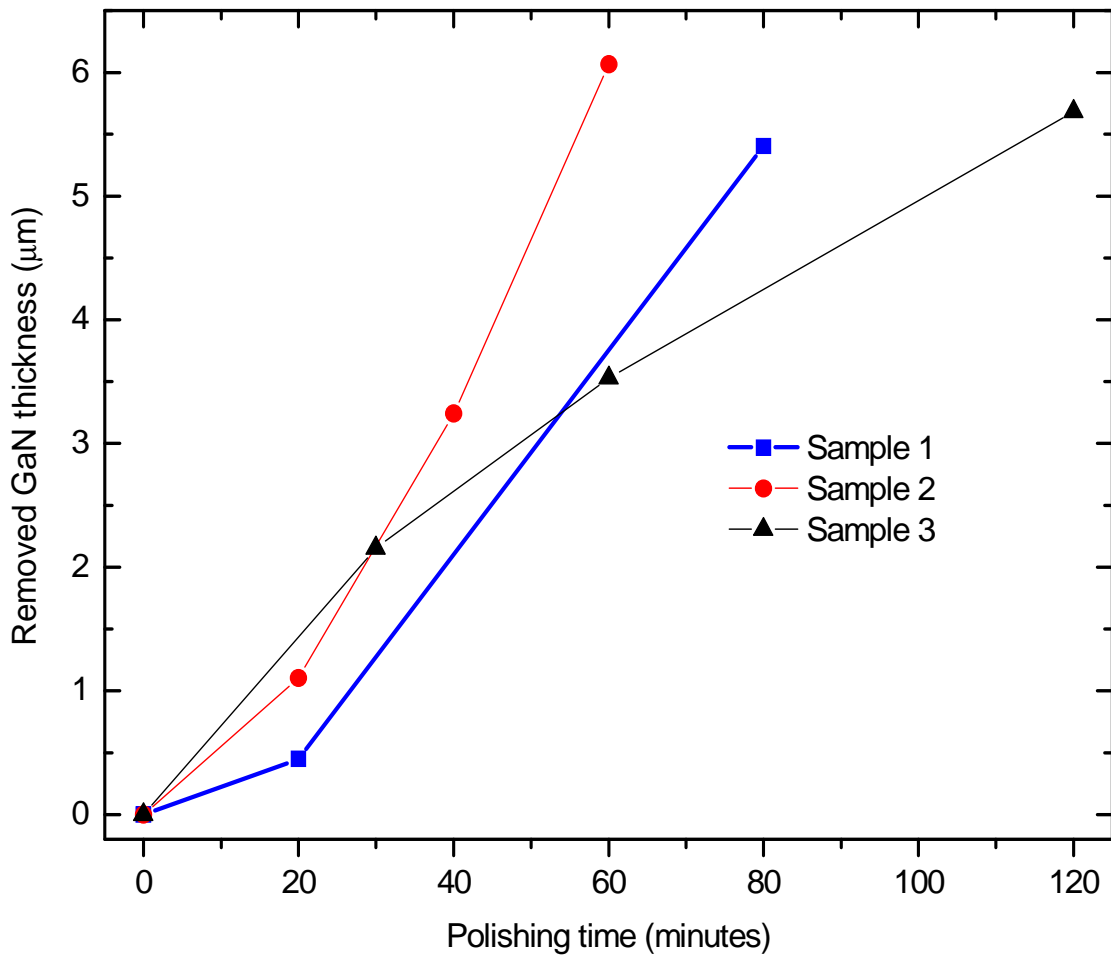


Figure 3.2: The dependence of the removal of cubic GaN on polishing time.

3.3: SAMPLE CHARACTERISATIONS

In this work, our cubic GaN samples had been characterised by photoluminescence (PL), atomic force microscopy (AFM), X-ray diffraction (XRD), secondary ion mass spectroscopy (SIMS), Hall-effect and current-voltage measurements. Most of the experiments were conducted at University of Nottingham.

3.3.1: Optical studies by photoluminescence measurements

It has been experimentally observed that [4], the hexagonal inclusions in cubic GaN give out strong PL even when present in very small quantities. In fact at room temperature, the hexagonal PL is much more significant and the cubic GaN PL is

negligible in comparison. For this reason, PL measurements were carried out at low temperature so that optical transitions in cubic GaN could be clearly observed and studied.

3.3.1.1: Sample Mounting

At the initial stage of this work, the samples were mounted onto a copper plate by using a small amount of GE Varnish (normally used for thermally anchoring electrical wires to solid surfaces and easily removed by acetone). In order to get better adhesion, the samples were dried for several hours. The plate together with the samples was then mounted on a sample holder. Next, the sample holder is put into a cryostat; a piece of apparatus in which low-temperature experiments are performed [5]. Before further discussion of the experiment details, a brief description of cryostat operation will be given.

3.3.1.2: Cryostat

In this work, an Oxford Instrument Optistat CF (continuous flow) cryostat was used to study the optical properties in cubic GaN at temperatures down to liquid helium temperature. Figure 3.3 shows the schematic diagram of the system. The optical access to sample is via a quartz window.

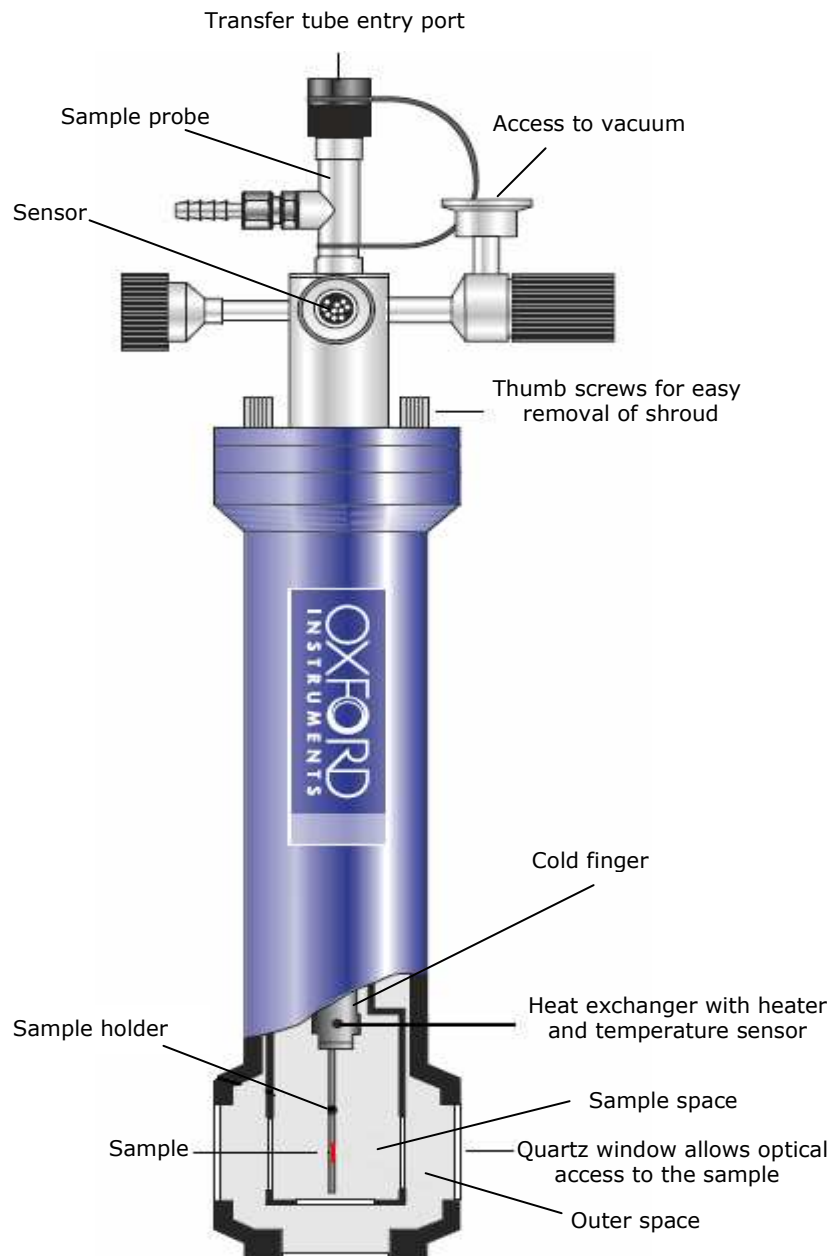


Figure 3.3: A modified schematic diagram of Optistat continuous flow cryostat system [6].

After the sample is mounted inside the cryostat, the sample space and the outer space are pumped out to reach a high vacuum $<10^{-6}$ mBar. If the vacuum is insufficient, the system will be hard to cool and the water in the air will be condensed and frozen on the sample and the optical window, which will scatter the light beam shone onto the sample, leading to noise and misleading results. To avoid this problem, it is important to ensure that the sample probe is tightly attached to the cryostat and the vacuum valve has good connection to the pump line.

After the cryostat was pumped out, liquid He was transferred from a separate He dewar, along an insulated transfer tube to the cold finger of the cryostat. He flow can be controlled by adjusting a needle valve on the transfer tube or on the gas flow controller. In the cryostat, He flows into a heat exchanger (which is thermally coupled with the sample) and goes out to the He return pipe in the form of gas. The heat exchanger is equipped with a thermometer which gives information on the temperature to a temperature controller unit. The temperature is adjusted by manually controlling the He flow.

This cryostat is small compared to other conventional bath cryostat systems. However, it allows faster pumping down to vacuum and cooling due to its size. Furthermore, the sample is directly cooled by flowing He, which turns into gas when it flows out from the system. This makes the cooling process much simpler. During the measurement, the incident laser power may change the temperature. However, this effect is very small and can be neglected.

3.3.1.3: Photoluminescence Measurements

In this experiment, a 355nm frequency-tripled Nd:YAG laser was used as the excitation source. Nomura et al [7] reported that the absorption coefficient of a cubic GaN layer is about $1 \times 10^5 \text{cm}^{-1}$ at this wavelength, which corresponds to our laser. The reciprocal of the absorption coefficient gives the penetration depth around $0.1 \mu\text{m}$.

Figure 3.4 shows the experimental setup for the PL measurement. At the first stage of this experiment, the sample was excited by the laser beam using a small lens. After that, the photons emitted by the sample were collected and focused by a larger lens. It should be noted that the laser spectrum could impinge the output data and therefore a notch filter was used to block the laser light reaching the detector. Next, the photon signal was transferred to a monochromator. A charge coupled device (CCD) camera collects the signal from the monochromator and sends it to the computer for analysis.

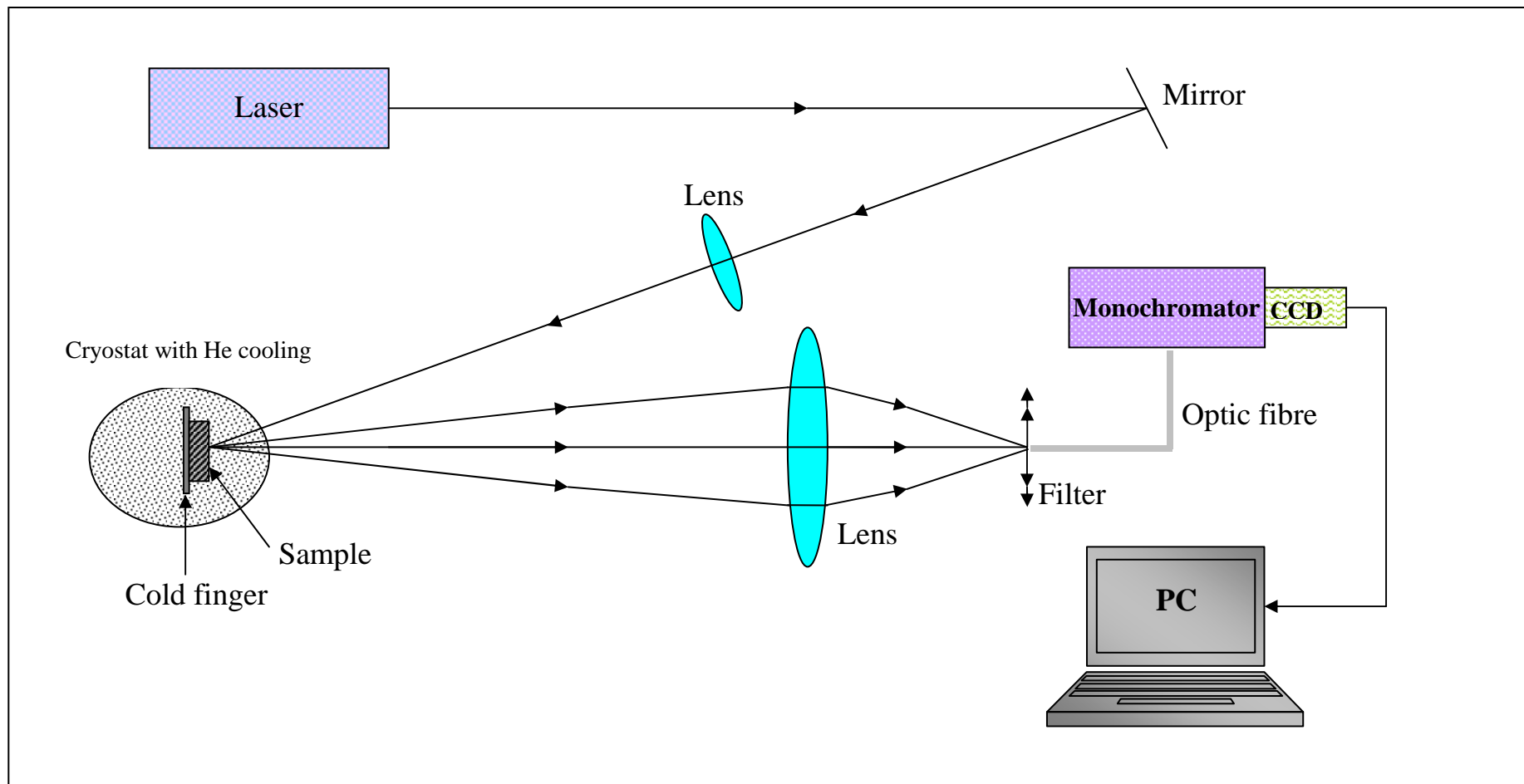


Figure 3.4: A schematic diagram of the PL system. The exciting source is a 355nm tripled Nd:YAG laser and the cryostat is cooled down to liquid helium temperature.

Figure 3.5 shows the general principal of the spectrometer used in this work. In the monochromator, the focussed light (A) enters the input slit (B). Next, the light is collimated by the first curved mirror (C). The collimated light is dispersed using an adjustable grating (D) and then being collected by the second mirror (E). At this mirror, the light is re-focussed and dispersed into different wavelengths at the CCD line camera (F). In this camera, the photon will charge up the CCD pixels to capture the image. The CCD camera then converts the image into digital signals that are subsequently transferred to the computer software. The wavelength that falls at the centre of the CCD camera is selected by adjusting the rotation angle of the prism. The advantage of using the CCD camera in this work over a detector such as a photomultiplier is that it allows simultaneous data collection for a large spectral range in each measurement.

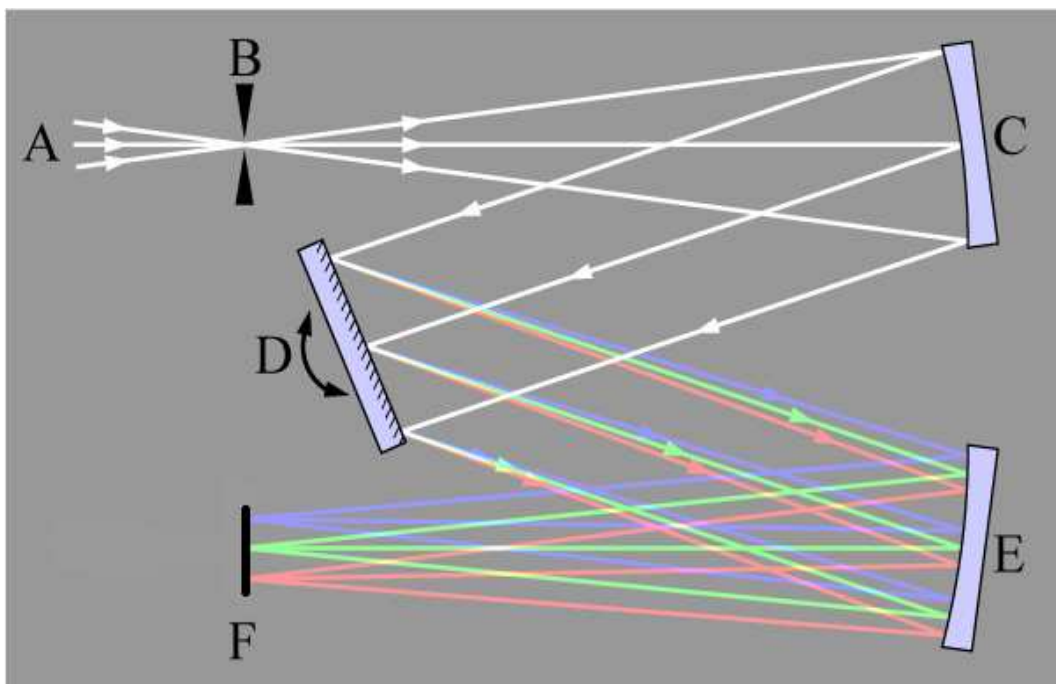


Figure 3.5: A schematic diagram of light dispersion in the monochromator used in this experiment. The diagram is modified from [8].

In this work, the laser spectrum was measured and its full width half maximum (FWHM) is found to be around 1.65nm. The laser line is narrower than this so,

therefore, the spectral resolution of the spectrometer must be better than 2nm. The whole system is controlled by Thorlabs Inc. Spectra software.

In this experiment, several issues could affect the measured data. Without extra caution, the GE Varnish may contaminate the sample surface during the sample preparation. As a result, the luminescence from the varnish would appear in the spectrum and mask the required data. Therefore, the samples should be stuck onto the copper plate with great care so that it will not contaminate the sample.

Moreover, some background noises like dark count from the detector (which is unavoidable during the measurement), scattering, movement of the optical system and stray light are always present during the measurement. To overcome these problems, these following actions were undertaken. Firstly, the surface of the measured samples should be cleaned and free from dust. Secondly, the system needs to be isolated from mechanical vibration; in this work, such vibration was coming from the pump. In addition, the optic components should be fixed firmly on the optical bench. Finally, the experiment was conducted in a nearly dark environment.

Sometimes, the collected light may saturate the CCD pixels. This causes a saturation that leads to misleading output. To address this problem, the intensity of the light should be reduced by placing an attenuation plate in front of the optic fibre.

3.3.1.4: Micro-Photoluminescence Measurement

In this work, we intend to observe the increase of hexagonal inclusions as a function of depth for bulk cubic GaN. Therefore, a reasonably small size of the laser spot is required in order to obtain the required spatial resolution. For this purpose, a special technique had been introduced in the PL setup.

At the initial stage of this work, a bulk cubic GaN sample was carefully cleaved so that the edge of the sample will be smooth for better measurement. Then, the sample was stuck on a specially designed holder, as shown in Figure 3.6, using

GE Varnish. During this process, it is important to ensure that the cubic GaN side faces toward the air so that the sample is not contaminated by the varnish. The sample was then mounted on the cold finger of the cryostat.

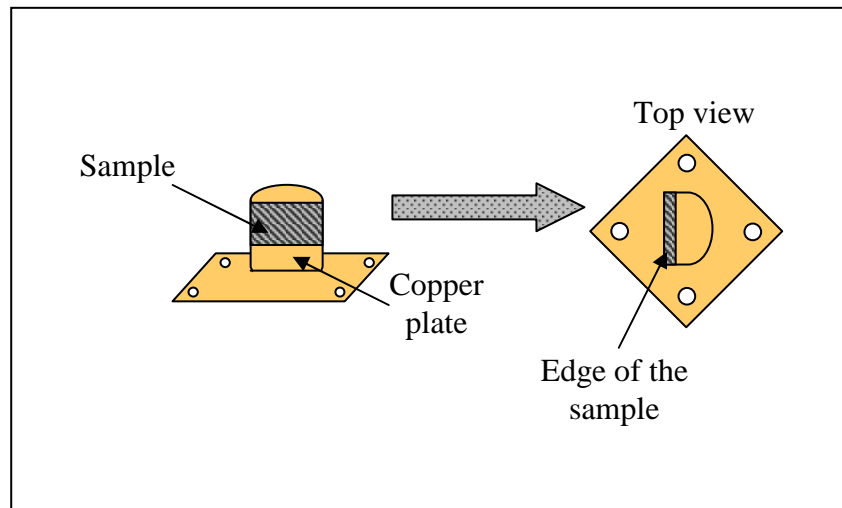


Figure 3.6: A schematic diagram of sample mounting on the specially designed holder.

As was mentioned earlier, the size of the laser spot used should be much less than the film thickness. To get this spot size, a micro objective mirror was used as it provides a laser spot with diameter less than $5\mu\text{m}$. Before the measurement, the sample needed to be placed exactly at the focus point of the laser spot. This can be done by adjusting the cryostat and/or the micro objective mirror. The position of the latter is controlled by a piezo-electric stage. This work required considerable care since even very small changes in the positions will put the sample considerably out from the focus point. When the sample was finally located at the focus point, the system was pumped out and cooled down to He temperature. Once this was done, the micro-luminescence measurement could be carried out.

Figure 3.7 shows the experimental setup for the micro-luminescence measurement. In this experiment, a quadrupled Nd:YAG laser with $\lambda.=266\text{nm}$ was used as the excitation source. The laser beam travelled through a beam

expander, where the diameter of the beam becomes larger but the angular divergence is reduced in order to get a better focussed laser spot. Next, the beam was directed to the micro-objective mirror by a small splitter prism. Details of the mechanism for focussing light onto the sample are shown in insert (a) of figure 3.7. The photons emitted by the sample travelled through the micro mirror in a similar way but in the opposite direction and reached a flip-out mirror. By using this mirror, the beam can be directed either to a camera or to the monochromator. Using the camera, we can view the laser spot on the sample, and the picture is shown in the insert (b) of figure 3.7. Using the monochromator, the spectrum of the sample as a function of depth was measured. The depth was varied starting from the point near the GaAs/GaN interface and moving towards the GaN/vacuum interface and the change of depth was controlled by a micrometer screw that was attached to the cryostat.

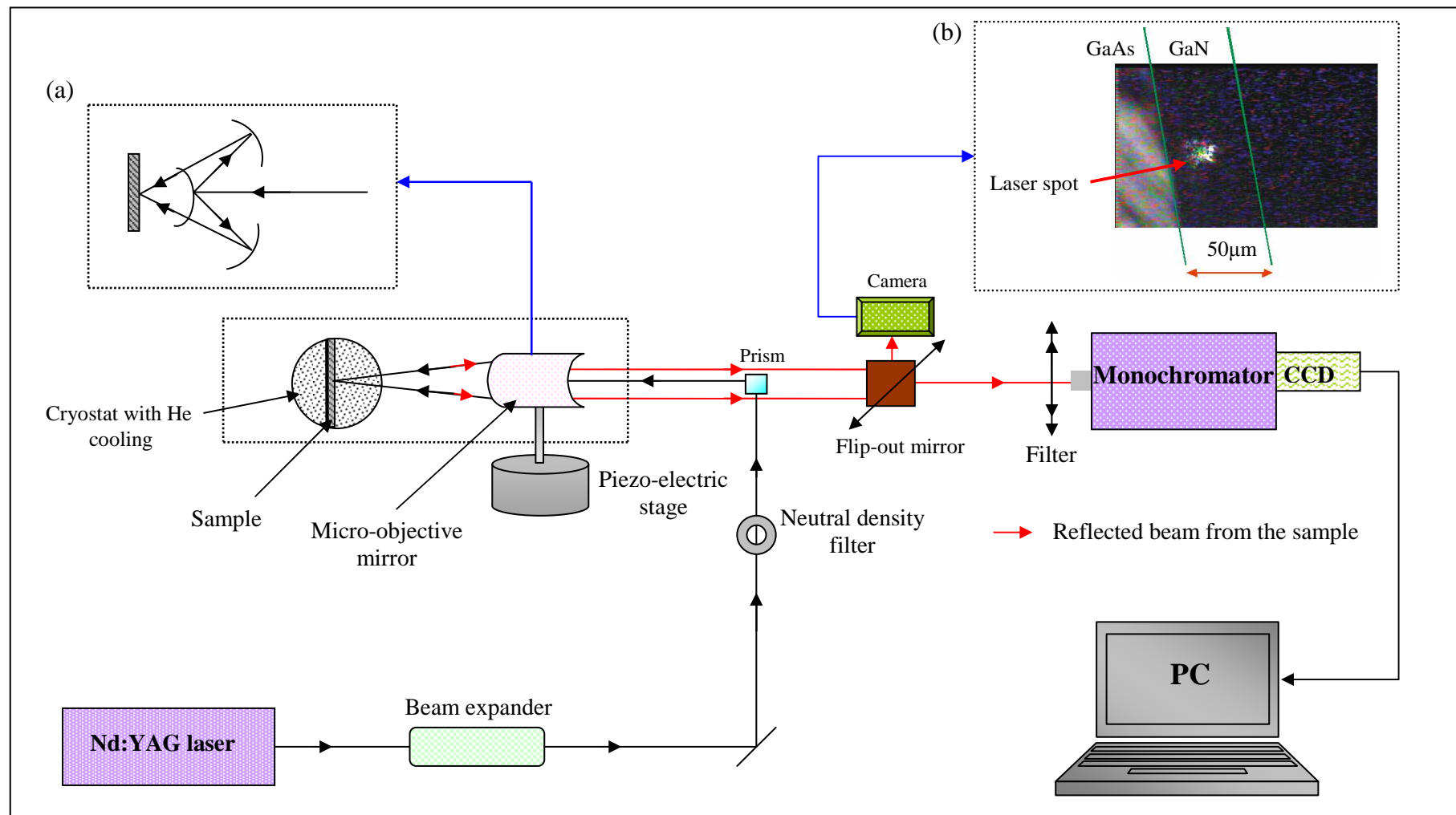


Figure 3.7: A schematic diagram of the micro PL system. Inset (a): the mechanism for focusing the incident light onto the sample in the micro objective mirror. Inset (b): the laser beam shines on the edge of 50µm cubic GaN sample in the cryostat.

3.3.1.5: Pump-probe measurement

In this experiment, the fundamental properties of cubic GaN such as sound velocity, elastic constants and refractive index were investigated. This work was carried out using the picosecond acoustic technique. It is a powerful technique to study the fundamental properties of solids for thin epilayers (only a few microns thick), and it is based on the generation and detection of picosecond-duration strain pulses using an ultrafast laser.

Before the measurement, an 80nm thick Al film was deposited on the polished side of the GaAs substrate to act as a hypersonic transducer. Then the sample was mounted onto the cold finger inside an optical cryostat. The pump beam ($\lambda=800\text{nm}$) was generated from a 40fs amplified Ti-sapphire laser. Firstly, a probe beam was split from the pump by a beam splitter and frequency doubled to give a probe beam wavelength of 400nm. The pump beam was modulated at 500Hz using a mechanical chopper and its time delay was controlled by a mechanical delay line. The beam spot with diameter of $200\mu\text{m}$ was focused onto the Al surface and the maximum excitation density applied was below $10\text{mJ}/\text{cm}^2$. When the pump pulses hit the Al film, strain pulses were generated as a result of the thermo-elastic effect in the metal. The bipolar strain pulses travel from the Al film to the GaAs substrate within 20-50ps and the strain amplitude was $\sim 10^{-3}$, depending on pump energy.

In parallel, the probe beam passed through a fixed distance delay line to allow for the time for the acoustic pulse to propagate through the substrate. The beam was then focused at an angle of incidence, $\alpha = 20^\circ$ onto the surface of the cubic GaN film. Next, the probe beam was aligned exactly opposite to the pump beam. The probe spot had a diameter less than $50\mu\text{m}$ with the excitation density below $10\mu\text{J}/\text{cm}^2$. The reflected beam from the sample was then detected by a balanced photodiode. The balanced photodiode provides a subtraction of the reflected beam and a reference beam split from the incident probe beam to reduce noise due to laser power fluctuations. A phase-sensitive detector (lock-in amplifier) was used to measure the signal after the balanced photodiode. The data was then transferred to the computer for analysis. In this work, the measurement was carried out for different temperatures

in the range of 4.7 to 300K. The experimental setup for this measurement is shown in Figure 3.8.

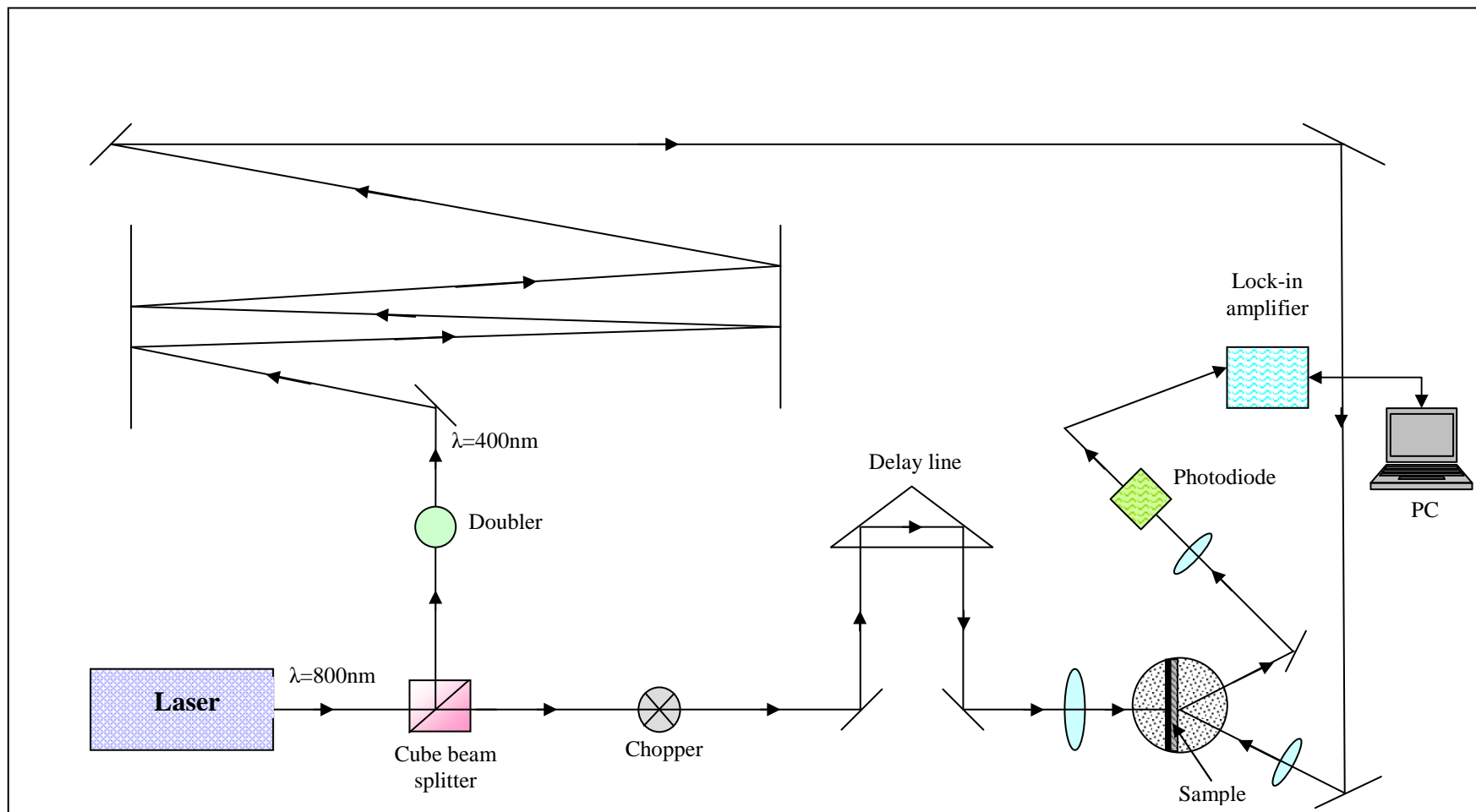


Figure 3.8: A schematic diagram of the pump-probe measurement. The exciting source is a Ti-sapphire laser ($\lambda=800\text{nm}$) and the sample is cooled down to helium temperature in an optical cryostat.

3.3.2: Surface analysis by AFM

In this work, the surface morphology of cubic GaN samples had been investigated by atomic force microscopy (AFM) measurements using an Asylum Research (Rambo) system. The advantages of using AFM in this work over other techniques, like scanning electron microscopy (SEM) for example, are it provides higher resolution as well as its simplicity in that it does not require any special treatment such as metal/carbon coating that can damage the sample.

The basic principle behind the AFM measurement is described as follows: initially, the sample was placed on a piezo-electric scanner stage. This stage controls the movement of the sample (on the order of nanometers) by changing an applied voltage during scanning. Next, the tip on the end of a cantilever is manually brought close to the sample surface. If the tip is too close to the sample surface, it would crack and at the same time scratch the surface. In this work, the tip was applied with constant force, which is monitored by the Igor Pro 6.04 software provided by the manufacturers of the AFM system, which controls the whole system. The resolution of the system is less than 1nm.

In this measurement, the tip is dragged across a sample surface and the change in the vertical position (z-axis) reflects the topography of the surface. Figure 3.9 shows a typical mechanism of the AFM measurement. The change in the height or vertical movement of the tip while the sample was moving was probed by a reflected laser beam on the backside of the cantilever. The reflected beam then hit a multi-segment photodiode. In the photodiode, the movement of cantilever and tip were detected and the signal was transferred to the computer program for analysis.

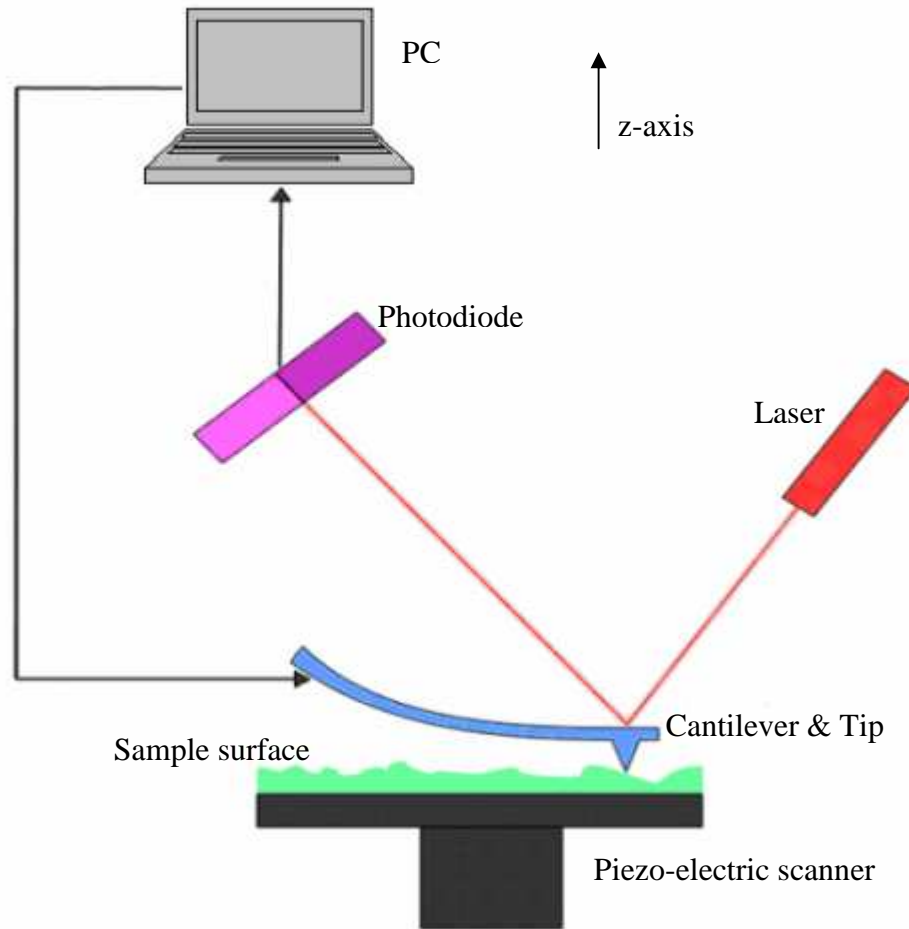


Figure 3.9: A modified schematic diagram of AFM. Original picture was taken from [9].

3.3.3: Structural analysis by XRD

In principle, a beam of x-rays is incident on a crystal and the repeating arrangement of atoms result in general scattering [10]. Most scattering results in destructive interference. However, the x-ray is diffracted if scattering at a certain angle is in phase with scattered rays from other atomic planes, which subsequently reinforce to each other giving constructive interference. Figure 3.10 shows the detailed mechanism of this process. Since each crystal has a different characteristic atomic structure, the x-rays are diffracted in a unique characteristic pattern.

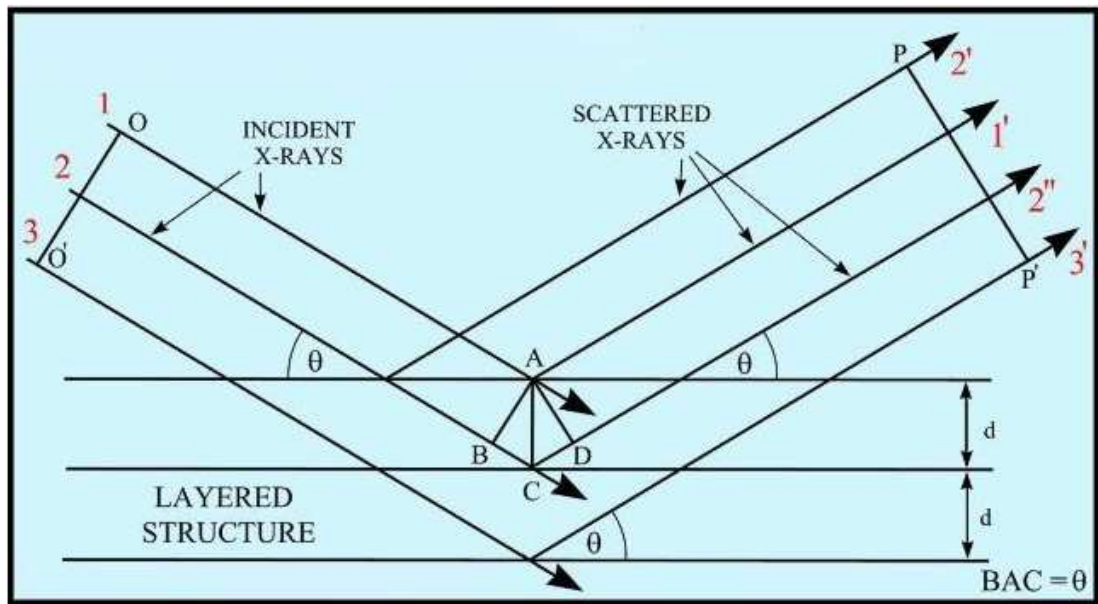


Figure 3.10: The x-ray diffraction in a crystal. This diagram is taken and modified from [11].

In this work, x-ray diffraction (XRD) measurements were carried out by Mr. Chris Standdon at University of Nottingham using a PANalytical system. The properties of cubic GaN samples have been investigated using $2\theta/\omega$ scanning. A description of $2\theta/\omega$ scanning can be found in [12]. Unique 2θ angles for cubic and hexagonal phases exist, which are normally used to identify the phase presents in GaN samples. Figure 3.11 shows the reported XRD data for (a) hexagonal GaN [13] and (b) cubic GaN [14] under $2\theta/\omega$ scanning. The peak intensity of (0002) hexagonal GaN occurs around 35° while the peak of (002) cubic GaN is around 40° . This result has been used as a main reference for observing the signature of hexagonal and cubic phases in our cubic GaN samples through the XRD measurement together with the PL measurement.

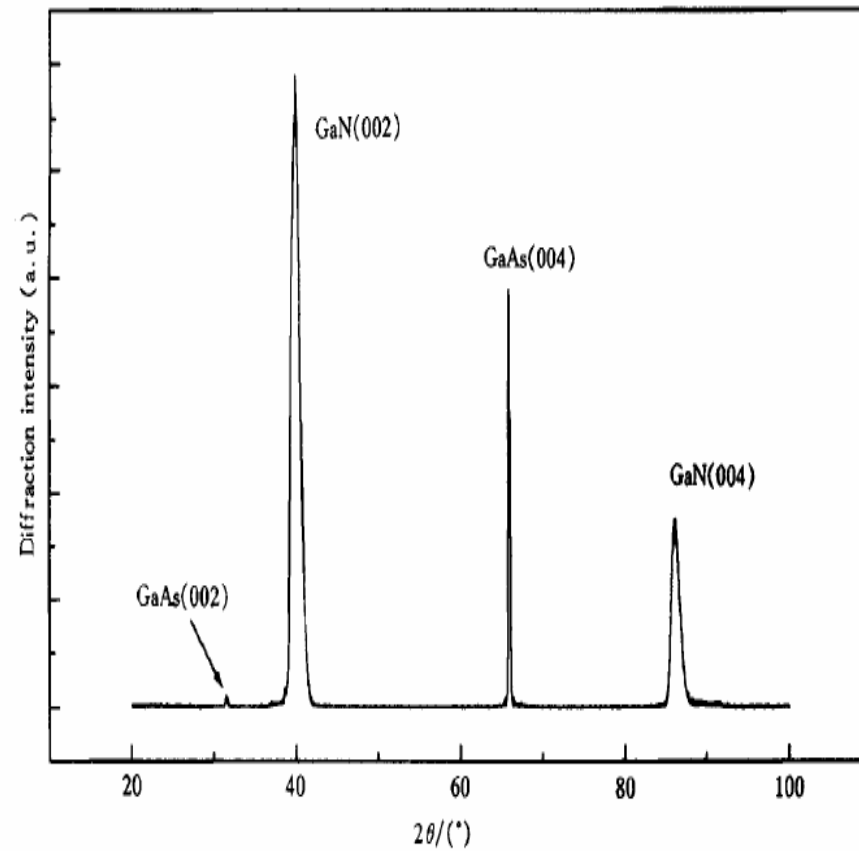
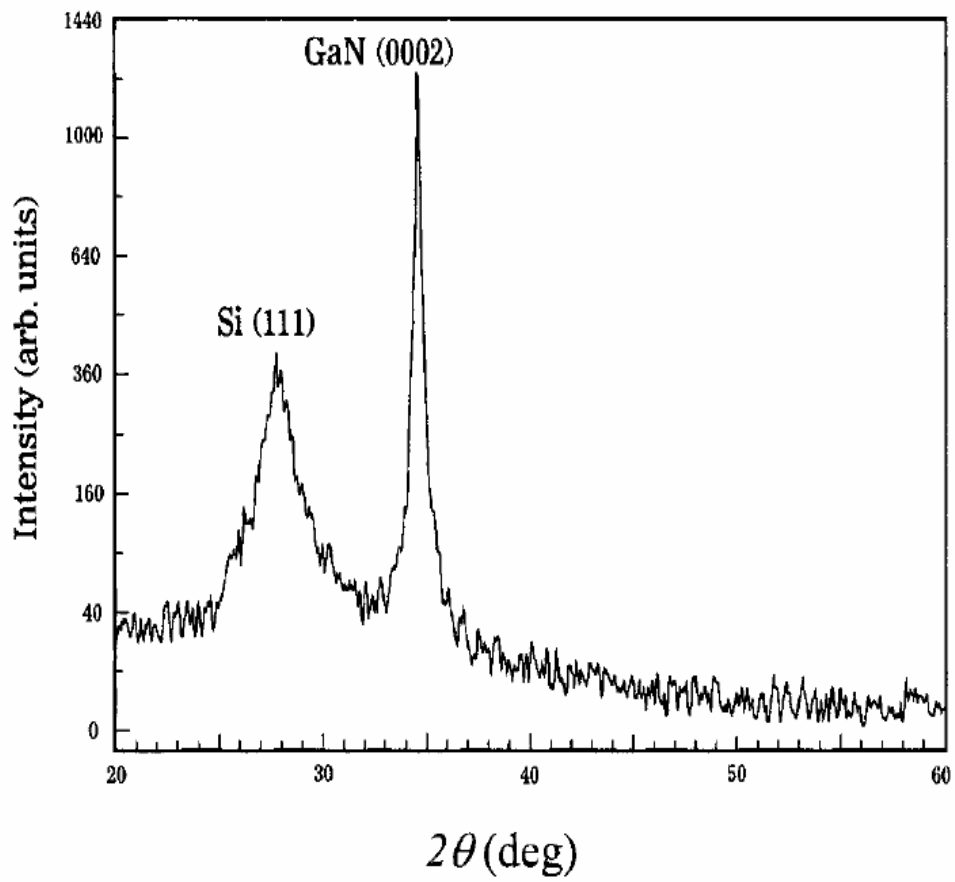


Figure 3.11: Reported data of XRD for GaN films (a) 2.5 μm thick hexagonal GaN grown on (111) Si substrate [13]. (b) 1.5 μm thick cubic GaN grown on (100) GaAs substrate [14].

3.3.4: Compositional analysis by SIMS

Compositional analysis of our cubic GaN samples was performed using Secondary ion mass spectroscopy (SIMS) measurement. The advantages of using SIMS over other methods, such as the Auger technique, are its sensitivity to very low concentrations of particles ($\approx 10^{18} \text{ cm}^{-3}$) and faster measurement. The basic principle of the SIMS technique is shown in Figure 3.12: a highly energetic primary ion beam is fired at a sample surface and leads to the ejection/sputtering of both neutral and charged (+/-) particles from the surface. Most particles are neutral and of no interest. However, the (+/-) particles compose an analytical signal that be measured with a mass spectrometer. Mass spectrometry reveals information about the atoms inside the sample.

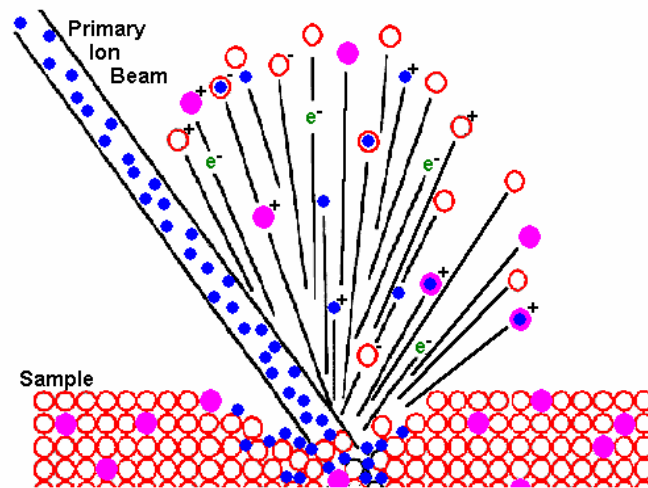


Figure 3.12: The bombardment of the sample surface by primary ions which knock secondary ions off from the surface. This picture is taken from [15].

In this work, the SIMS measurements were carried out at Loughborough Surface Analysis Ltd. The aim was to investigate the extent of arsenide diffusion into the GaN from GaAs substrate. The samples were measured under vacuum, and a liquid nitrogen trap was used to reduce the background from the system to as low a level as possible, which is about 10^{18} cm^{-3} . Cs^+ primary ion species with energy of 10keV were used in this work as they are more sensitive to arsenide than other ion species.

3.3.5: Electrical study by Hall effect

The electrical properties of cubic GaN samples were determined by Hall Effect measurement at room temperature. In this measurement, a current is supplied to the sample by the current source. Then, a magnetic field is applied perpendicular to the sample, which results in the Lorentz force that causes charge to accumulate at one side of the sample. This leads to a potential difference across the sample. This potential difference defines the Hall voltage, V_H , which is measured by a voltmeter. Figure 3.13 shows the experimental setup for the Hall Effect measurement.

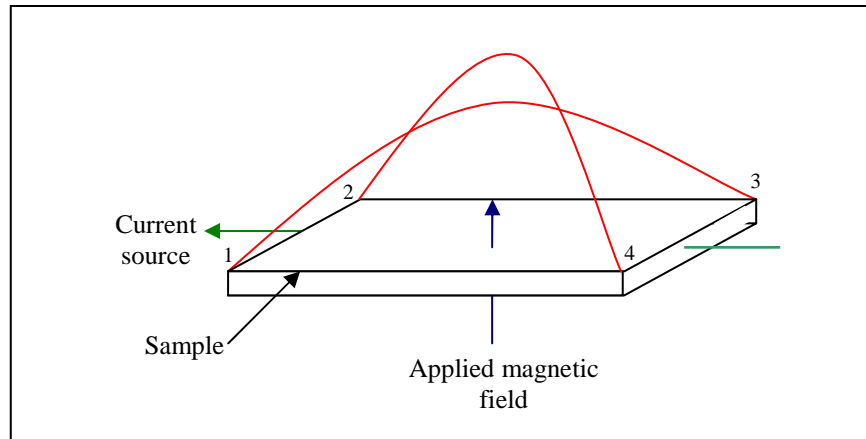


Figure 3.13: A schematic diagram of the Hall Effect measurement. There are four contacts at the corners of the sample. The red lines show the Hall voltage across different points with the variation of current and magnetic field polarities.

There are several problems one may encounter during this experiment. The most serious problem comes from poor contacts on the sample. To solve this problem, Indium wire was used for the contact and a sufficiently high temperature was applied to the sample to allow the indium to diffuse into the material. In this case, the contacts should be placed at the corners of the sample for better result. Besides, a non-symmetric shape of the samples could lead to error in the data. For these reasons, a number of repeated measurements were carried out to improve the accuracy of the results. The following sections will describe the details of measuring Hall voltage and resistivity so that the carrier density and mobility of the measured samples could be obtained.

3.3.5.1: Hall voltage measurement

The Hall voltage, V_H was measured by using the standard van der Pauw procedure. From Figure 3.13, there are four contacts at the corners of the sample. Eight measurements of Hall voltages at different points were measured with variation of polarities of the applied current and magnetic fields. For example, current was injected from 1 to 3 with a positive (P) magnetic field. Hence, the Hall voltage across 2 and 4 will be V_{24P} . With the same current, a negative (N) magnetic field was applied to the sample, thus giving V_{24N} . The same steps were continued for the values of V_{42P} , V_{42N} , V_{13P} , V_{13N} , V_{31P} , V_{31N} . The differences of the Hall voltages (each Hall voltage measured at the same current but difference magnetic field) were calculated, e.g $\Delta V_{24} = V_{24P} - V_{24N}$. The average of these values, V_H (from ΔV_{13} , ΔV_{31} , ΔV_{24} and ΔV_{42}) defines the conductivity of the sample. The sample is p-type if V_H gives positive sign and n-type if it is negative.

Using the value of the Hall voltage, V_H and the thickness of the sample, d , the carrier density in the sample was calculated by

$$n = 8 \times \left| \frac{I \times B}{q \times V_H \times d} \right| \quad (1)$$

where q is the elementary charge ($1.602 \times 10^{-19} \text{C}$). The applied magnetic field, B is 0.307T and the applied current, I is 0.01mA. From equation (1), the sheet carrier density is given by

$$n_s = n \times d \quad (2)$$

3.3.5.2: Resistivity measurement

In this measurement, the current was applied from two different contacts, which were parallel to each other. For example, current was injected from 1 to 2, I_{12} and the voltage across between 4 and 3, V_{43} was measured. This gives a resistance, $R_{12,43}$. Next, the opposite current polarity, I_{21} was applied to measure the value of V_{34} and

therefore the resistance is $R_{21,34}$. The same steps were repeated to find $R_{32,41}$, $R_{23,41}$, $R_{43,12}$, $R_{34,21}$, $R_{14,23}$ and $R_{41,32}$. In an ideal case, the vertical resistance, $R_{vertical}$ should be equal to horizontal resistance, $R_{horizontal}$. However, this condition was unachievable due to the limitations in the experiment. From the observation, the error in this measurement was found to be less than 3%, showing errors in the setup were already minimised. After measuring the resistances, the average of $R_{vertical}$ and $R_{horizontal}$ were calculated by

$$R_{vertical} = \frac{R_{12,34} + R_{34,12} + R_{21,43} + R_{43,21}}{4} \quad (3)$$

$$R_{horizontal} = \frac{R_{23,41} + R_{41,23} + R_{32,14} + R_{14,32}}{4} \quad (4)$$

Using the values of $R_{vertical}$ and $R_{horizontal}$, the sheet resistance, R_s was calculated by solving the van der Pauw equation by iteration as given as follow

$$\exp\left(\frac{-\pi R_{vertical}}{R_s}\right) + \exp\left(\frac{-\pi R_{horizontal}}{R_s}\right) = 1 \quad (5)$$

Knowing the value of R_s , the mobility of the majority carrier in the sample was calculated. Using the values of the sheet carrier density, n_s and the sheet resistance, R_s , the mobility, μ_m of the sample was calculated by

$$\mu_m = \frac{1}{qn_s R_s} \quad (6)$$

3.4: DEVICE PREPARATIONS ON CUBIC NITRIDES BASED TUNNEL DIODE

In this work, cubic nitride based tunnel device structures had been grown by MBE. The grown device structure is shown in Figure 3.14. The next step is that the devices need to be fabricated to form a number of small mesa structures. To do this, the devices have to be etched with in a suitable and controllable manner. However, III-nitrides cannot normally be simply etched by wet etching as they are chemically resistant materials. In this work, we used reactive ion etching (RIE) to etch our cubic III-nitride based devices. This technique uses reactive plasma to etch the materials.

The plasma etching is typically qualified by etching rate, etching uniformity, etching direction and selectivity of the material to be etched. In this work, the etching rate is approximately 600nm/min. After the etching, we deposited Ti-Al-Ti-Au metal layers on the top of the devices and annealed at 440°C while Ge-Au-Ni-Au metal layers was deposited on the bottom contact and annealed at 365°C. A brief description of the device fabrication is shown in Figure 3.15. This fabrication process was carried out by Dr. C. Mellor and Mr. Jas Chauhan.

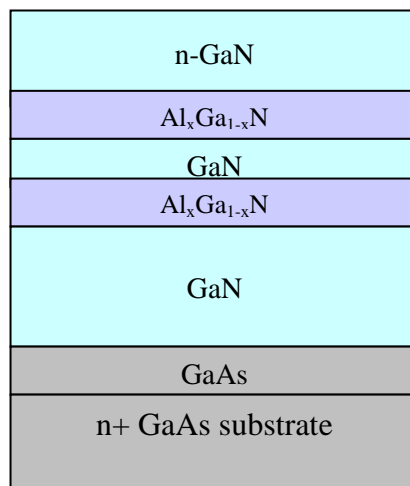


Figure 3.14: A schematic diagram of cubic Al_xGa_{1-x}N/GaN based tunnel diode.

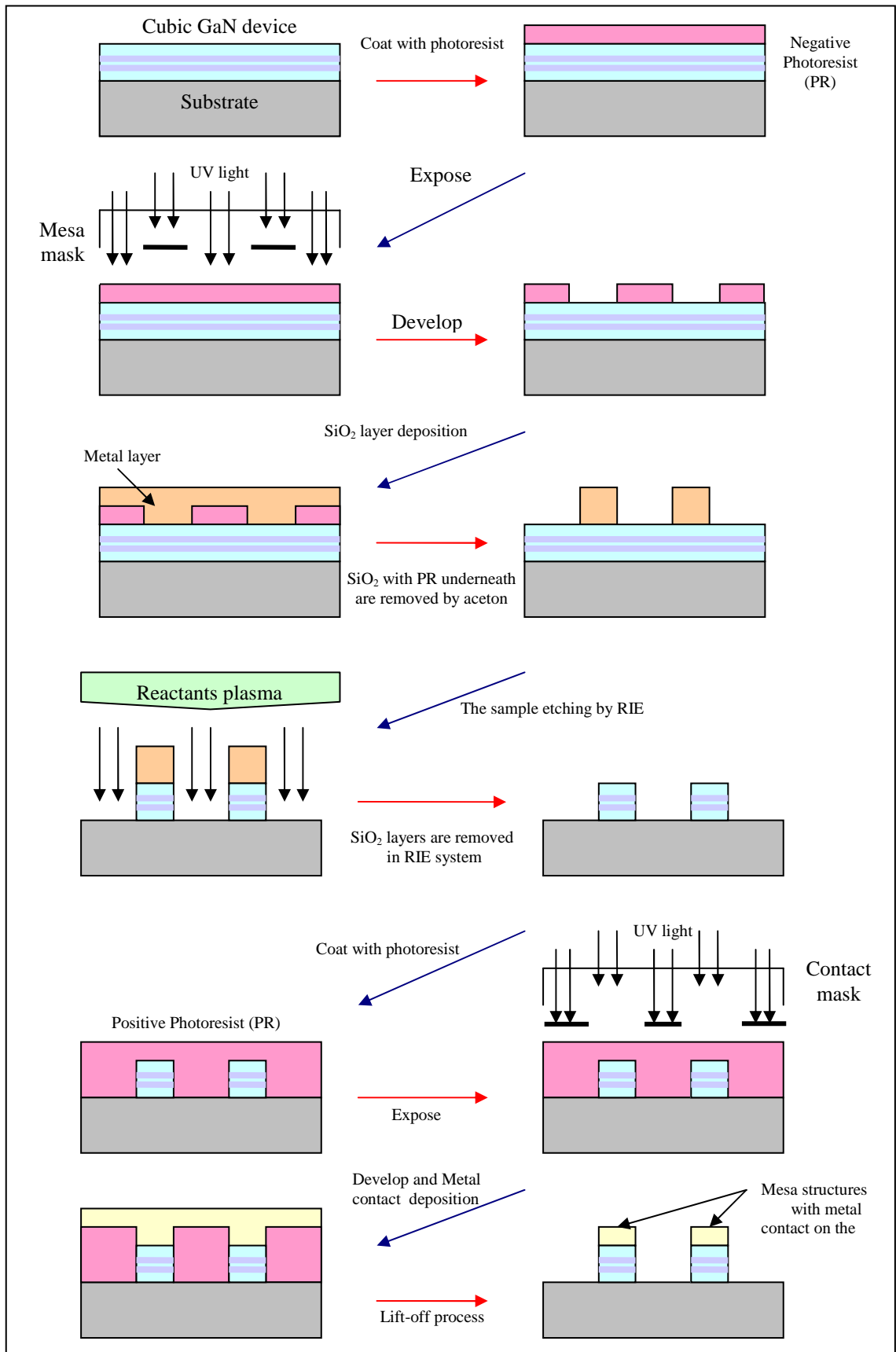


Figure 3.15: The fabrication process for forming smaller mesa-structures for cubic AlN/GaN based tunnel diode.

3.5: ELECTRICAL MEASUREMENTS ON CUBIC NITRIDES BASED TUNNEL DIODES

In this work, the vertical transport properties of cubic nitride based tunnel diodes were investigated by current-voltage (I - V) measurement. Figure 3.16 shows the electrical setup for the I - V measurement. A bias voltage was applied to the devices using a voltage source. In this setup, a potential drop was measured across a 20Ω resistor load to give the current. A digital multi-meter (DMM) recorded the voltage drop across the resistor as a function of applied voltage. This raw data was then calibrated by using Ohm's law in order to obtain the current-voltage characteristic for the device.

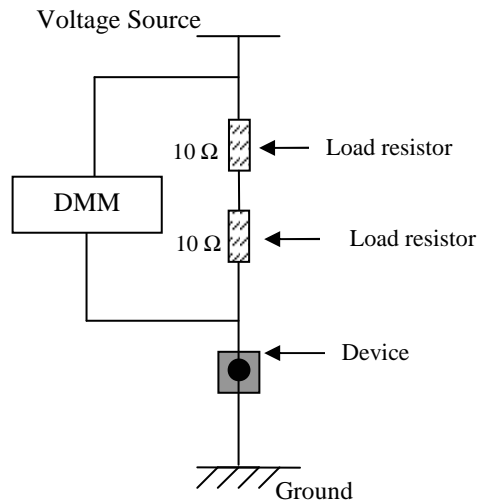


Figure 3.16: The circuit diagram for I - V measurement.

In addition to this work, a conductance measurement had been carried out on larger size of cubic based tunnel devices. In this measurement, the gradient current $\left(\frac{dI}{dV}\right)$ as a function of applied voltage, V was measured using a small modulation from a lock-in amplifier. From this technique, the gradient current can be measured directly without the interference of background noise. The schematic diagram of this measurement is shown in Figure 3.17.

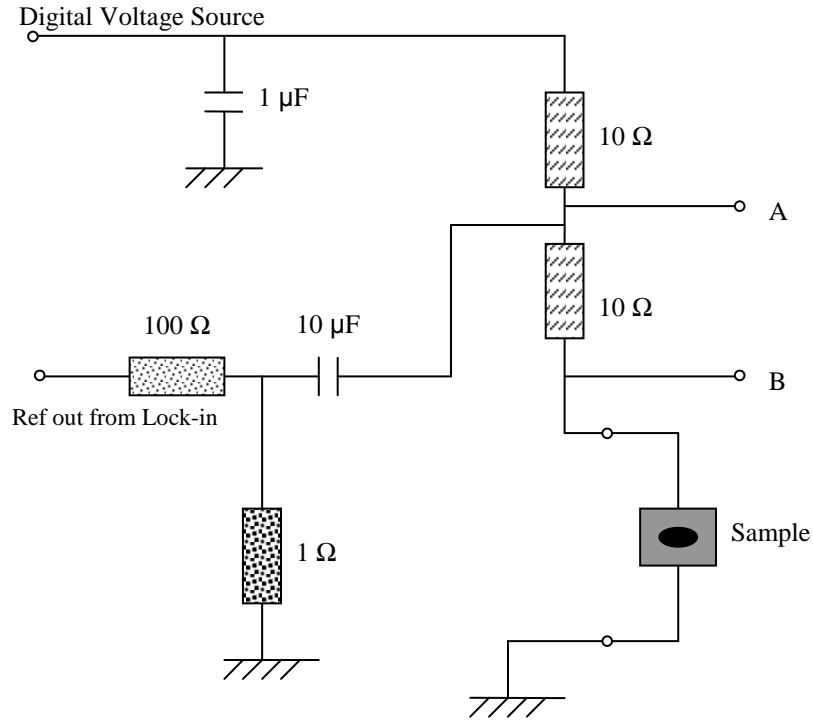


Figure 3.17: The schematic diagram for conductance measurement.

3.6: CONCLUSIONS

The description of the experimental tools and techniques used in this project has been presented. In summary, cubic GaN samples were grown by Molecular Beam Epitaxy (MBE). Next, the cubic samples have been characterised by PL, XRD, SIMS, AFM and Hall effect measurements. A brief explanation of the fabrication process for developing cubic nitride based tunnel diodes was presented. Finally, the vertical transport properties of the device have been studied by I - V and conductance $\left(\frac{dI}{dV}\right)$ measurements.

REFERENCES

1. T.S. Cheng, L.C. Jenkins, S.E. Hooper, C.T. Foxon, J.W. Orton, D.E. Lacklison, *Appl. Phys. Lett.*, (1995). **66**: p. 1509.
2. G. Feuillet, H. Hamaguchi, K. Ohta, P. Hacke, H. Okumura, S. Yoshida, *Appl. Phys. Lett.*, (1997). **70**: p. 1025.
3. Ching-Fu Lin, H-Chou Tseng, Hsin-Chu, Teng-Chi Yang, Koahsiung, United States Patent (2003). **US 6521470 B1**.
4. G.Ramírez-Flores, H. Navarro-Contreras, A. Lastras-Martínez, R. C. Powell, J.E. Greene, *Physical Review B*, 1994. **50**(12): p. 8433.
5. <http://uk.lowtemp.org/1-Woodcraft.pdf>.
6. <http://www.oxinst.com/products/low-temperature/opticaland-spectroscopy/optistatcf-v/Pages/optistatcf-v.aspx>.
7. I. Nomura, K. Kishino, A. Kikuchi, *Solid State Electronics* (1997). **41**: p. 283.
8. <http://en.wikipedia.org/wiki/Monochromator>.
9. http://en.wikipedia.org/wiki/Atomic_force_microscope.
10. Jr.,C.W. 3rd ed. *Material Science and Engineering: An Introduction* (1994), New York: John Wiley & Sons Inc.
11. <http://pubs.usgs.gov/of/2001/of01-041/htmldocs/xrpd.htm>.
12. Bennet, D.W., *Understanding Single-Crystal Crystallography* 2010: Wiley VCH.
13. H.Zhang, Z. Ye, B. Zhao, H. Liu, *Semicond. Sci. Technol.*, (2000). **15**: p. 649.
14. D. Xu , R. Wang , H. Yang , L. Zheng , J. Li, L. Duan, R. Wu, *Science in China Series A: Mathematics*, (1998). **42**: p. 517.
15. <http://pprco.tripod.com/SIMS/Theory.htm>.

CHAPTER 4: STUDIES OF CUBIC GaN

The aim of this work is to achieve large thickness (up to $\sim 50\mu\text{m}$) of cubic GaN with low hexagonal inclusions for use as free-standing substrates. Therefore, it is important to determine the optimal growth conditions for cubic GaN. In this work, MBE cubic GaN samples were grown on GaAs substrates using a variety of growth parameters. After the growth, these samples were characterised by photoluminescence (PL), X-ray diffraction (XRD) and Hall Effect measurements. The data from these measurements are reported in this chapter.

4.1: STUDIES OF OPTICAL PROPERTIES OF CUBIC GaN

In this work, PL measurement was carried out to observe the increase of hexagonal inclusions in undoped cubic GaN samples with the variation of growth parameters, including III/V ratio, thickness, growth rate and growth temperature. During the experiment, the top side of the samples were excited by the laser and spectra from the samples were measured. In addition to this work, some samples were also characterised by XRD measurement.

4.1.1: PL measurement on cubic GaN with the variation of III/V ratio

At the first stage of this work, thin, not intentionally doped, cubic GaN films were grown with similar thickness, approximately $0.800\pm 0.050\mu\text{m}$ under three main growth conditions; N-rich, Ga-rich and near stoichiometric conditions (with constant applied nitrogen flux). The growth details are described as follows: (1) under N-rich growth: Ga flux is less than active nitrogen flux (2) near stoichiometric growth: the Ga flux is slightly larger than the active nitrogen and they are almost equal to each other (3) under Ga-rich growth: the Ga flux is much larger than the active nitrogen flux and leads to the formation of Ga droplets on the surface. The growth rate was $0.45\mu\text{m}/\text{hour}$ and the growth temperature around 680°C .

Figure 4.1 shows the luminescence spectra for the samples at different growth conditions. The samples which were grown under Ga-rich and stoichiometric conditions show three significant well-resolved peaks at 3.10, 3.17, and 3.25eV. It is difficult to explain the origin of the first peak at 3.10eV. However, this value is somewhat close to the reported value for a free to bound excitonic recombination ($e'A$) at an additional acceptor level in cubic GaN [1]. The second peak observed around 3.17eV is almost similar to the reported energy for donor-acceptor (DA) pair transitions in cubic GaN [1, 2]. The third emission peak is at about 3.25eV and this peak may be attributed to excitonic emissions in cubic GaN [2-4]. Clearly, these three peaks are well resolved, showing an indication of high quality cubic GaN layers. On the other hand, the sample which was grown under N-rich conditions shows a stronger and broader peak around 3.23eV. This peak is due to the overlap of two broad lines from excitonic and DA pair transitions in cubic GaN and therefore causes a shift to lower energy.

There is a very weak signal around 3.47eV that may correspond to donor-bound exciton (D^0X) transitions in hexagonal GaN [5, 6]. Detailed investigation reveals that the hexagonal inclusions increase if the III/V ratio is far from unity. It had been demonstrated that higher nitrogen flux results in rough nitride surface. As been reported [7, 8], the surface roughness might be associated to the increase of the hexagonal content and this agrees with the result in Figure 4.1. On the other hand, as the III/V ratio approaches unity from N-rich side (increasing the Ga-flux), the hexagonal content reduces, which suggests that cubic GaN is grown better under this condition. A further increase in the Ga-flux results in Ga adatoms that are weakly bound to the surface and delocalised Ga-Ga metallic bonds [9]. These result in higher surface mobility that could improve the surface quality of the sample. Increasing the Ga flux still further leads to the formation of droplets, thus resulting in an increase in hexagonal content. This is consistent to what had been observed in [9].

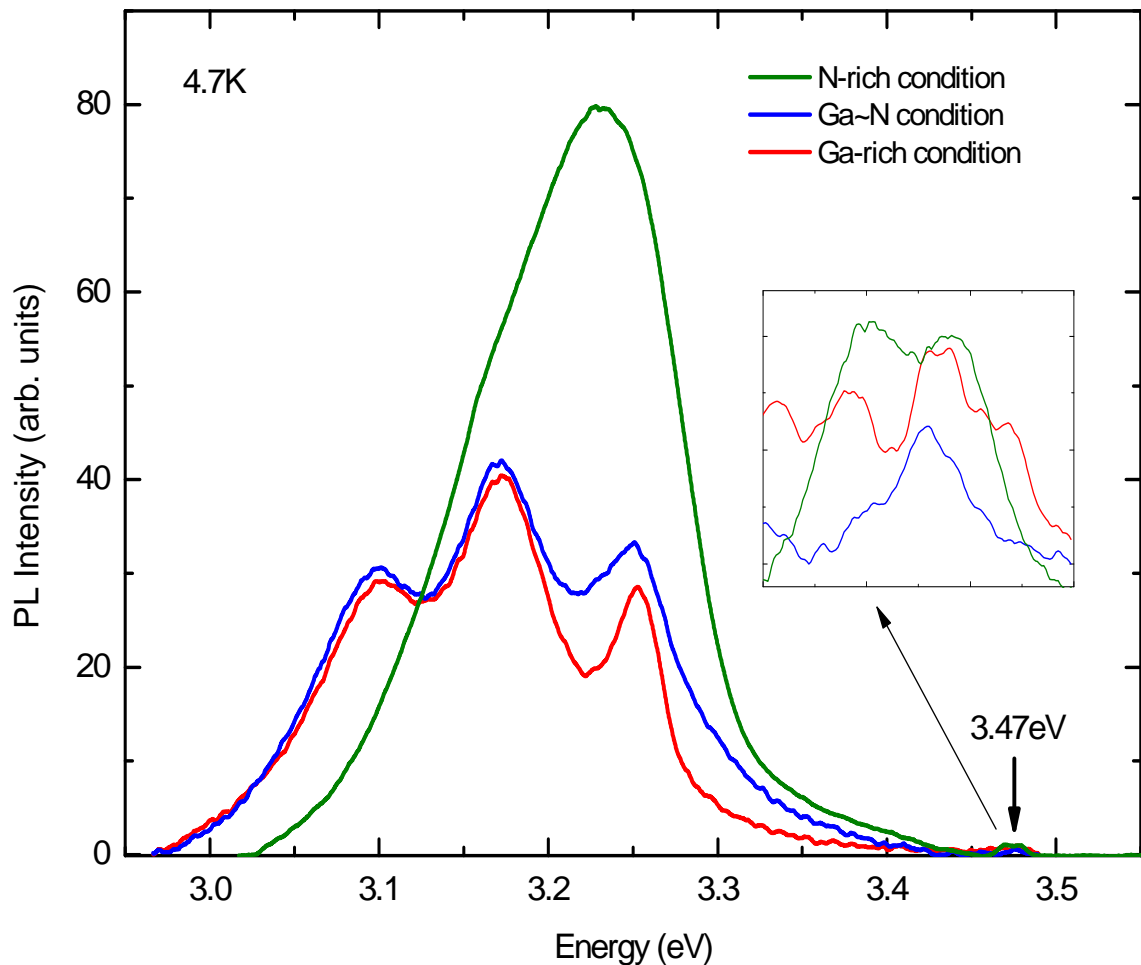


Figure 4.1: PL spectra for different samples grown with different III/V ratio. There are three clear peaks that are related to the emission in cubic GaN. Insert figure shows the hexagonal related emission around 3.47eV.

One interesting thing that had been observed in this study is that the hexagonal content still gives a signal at all even though hexagonal inclusions have a higher band gap than the surrounding cubic material. There are several possible reasons for this behaviour. Firstly, it could be due to the fact that hexagonal GaN can more easily crystallize into a better crystal structure with less defects compared to cubic GaN. Secondly, hexagonal grains may accumulate on the surface and direct excitation from the laser gives hexagonal PL. Another possibility is that electron-hole pairs are directly excited in the hexagonal material, but these become localised at defects and recombine to give the hexagonal related emission.

In this work, we also observe evidence of hexagonal content through XRD measurements. The XRD data for the sample which was grown under nearly

stoichiometric conditions is shown in Figure 4.2. Clearly, the peak of cubic GaN can be seen around 40° . However, there is no measurable signal of hexagonal GaN, which is expected around 35° . This shows that XRD is not sufficiently sensitive to detect very small hexagonal content in cubic GaN. The XRD measurements on the other two samples also give the same result.

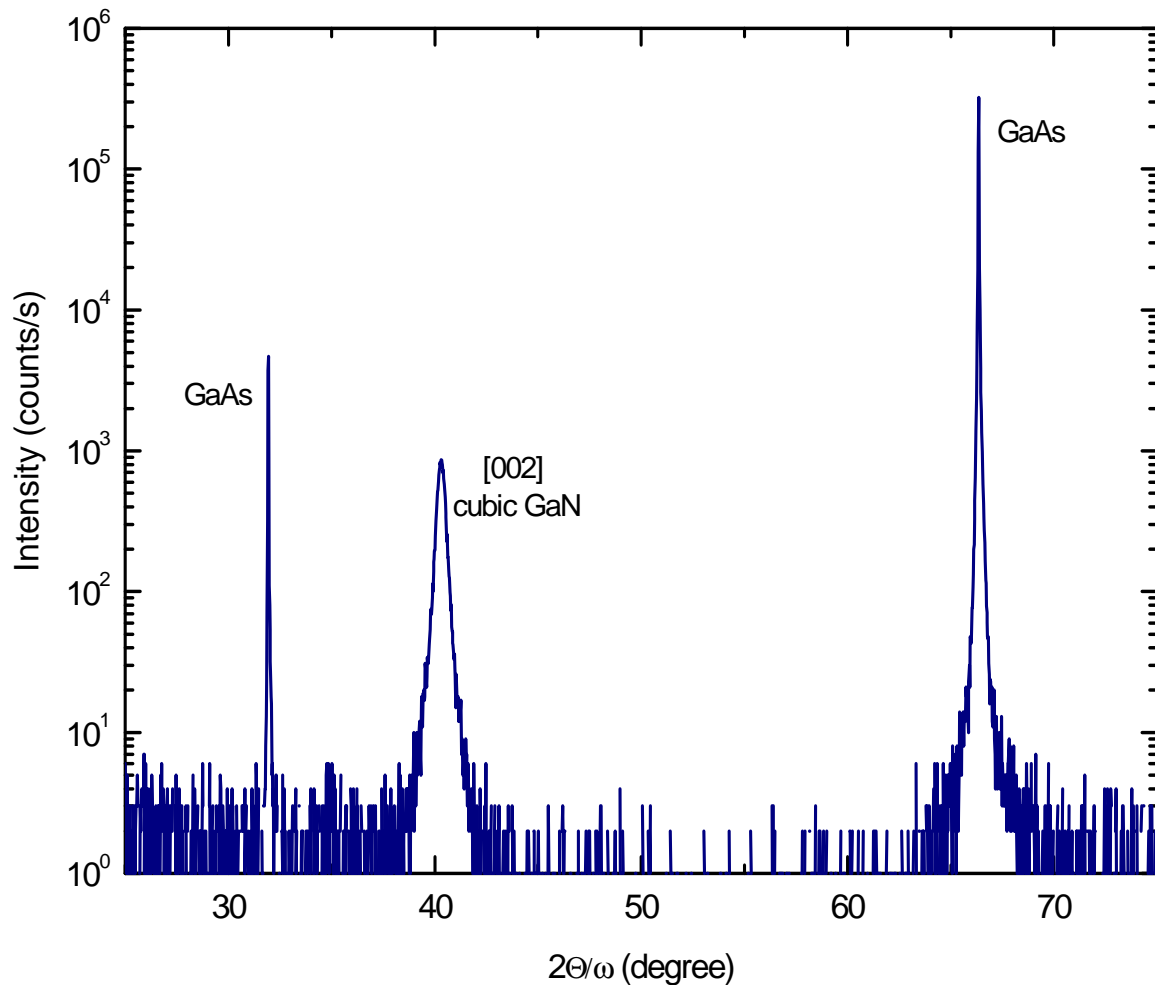


Figure 4.2: XRD data for the sample grown nearly under stoichiometric condition. The sample shows the cubic signal in [002] direction around 40° . The intensity of GaAs is coming from the GaAs substrate.

From the measurements, it is obvious that PL is much more sensitive to the hexagonal fraction than XRD for very small incorporation. This demonstrates the important point that we cannot rely on only one measurement technique in order to observe the existence of cubic and hexagonal phases in cubic GaN samples, as has

been done in other works, e.g [7]. At this point, we have demonstrated that cubic GaN is grown better under near stoichiometric growth. This result is used as a starting point for the subsequent growth of thick cubic GaN.

4.1.2: PL results for cubic GaN with the variation of growth rate

It has been reported that the growth rate is one of the crucial factors that could influence the amount of hexagonal content in cubic GaN. However, this subject is not widely studied and therefore will be investigated here. In this work, two samples of 2 μm thick undoped cubic GaN were grown at different growth rates; 0.4 $\mu\text{m}/\text{hour}$ and 0.8 $\mu\text{m}/\text{hour}$, respectively. The PL spectra for the samples are shown in Figure 4.3. It should be noted that the spectra do not show three well resolved peaks (as was observed in Figure 4.1) as the thickness of the cubic layer is increased. This issue will be discussed later.

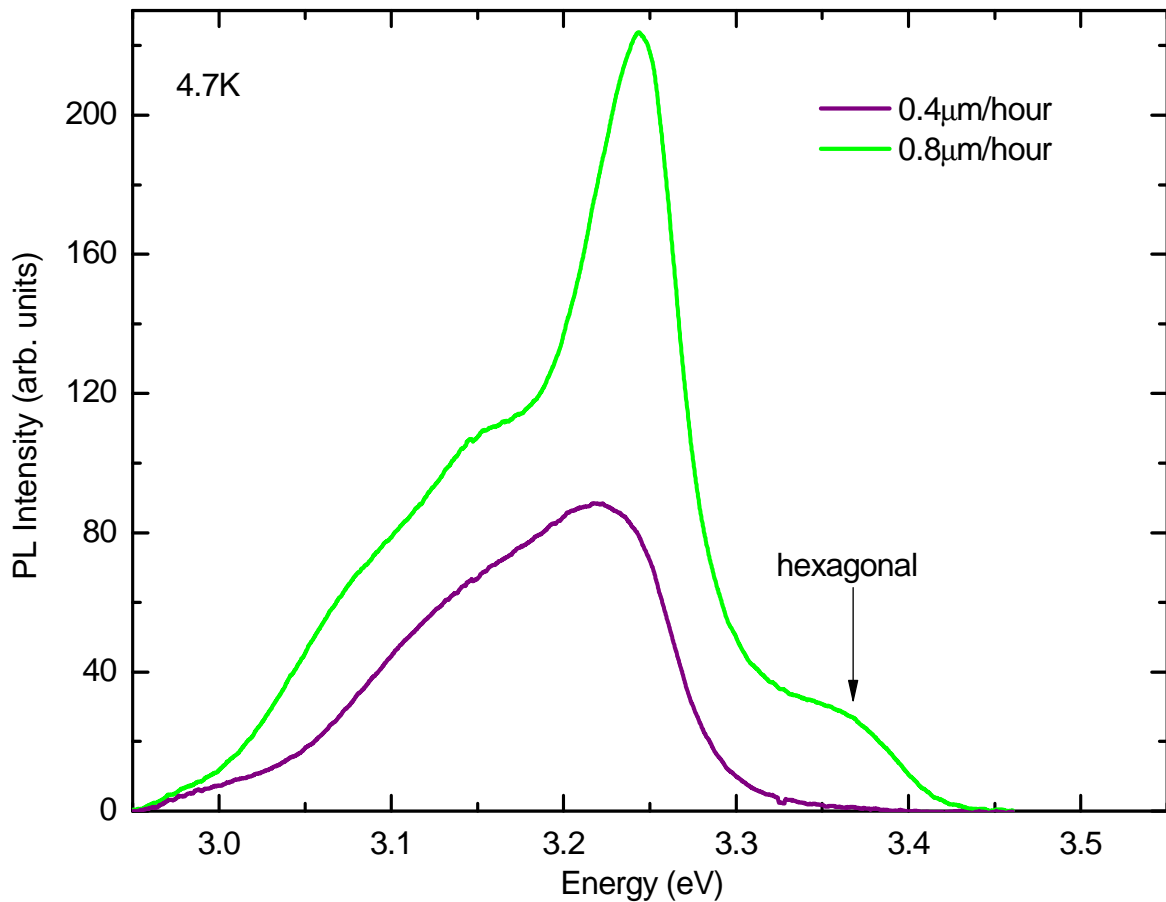


Figure 4.3: PL spectra for the cubic samples grown at different growth rates.

From the figure, it is clear that slower growth gives a broad signal that is due to the overlap of two broad signals from *DA* pair and excitonic recombinations in cubic GaN. The signal of hexagonal GaN is almost unseen in the spectra, showing that there are negligible hexagonal inclusions in the sample. When the growth rate becomes higher, the emissions that correspond to cubic GaN are more resolved but the signal of the hexagonal GaN is also stronger. This shows that the hexagonal inclusions start to evolve when the growth becomes faster.

To explain this behaviour, it might be worth considering mechanisms that occur during the growth: It was reported that faster growth decreases the surface mobility [10, 11], which leads to the increase in the hexagonal incorporation in cubic GaN. In addition, it is difficult to maintain the growth conditions for cubic GaN during fast growth which also increases the probability that hexagonal inclusions will grow in the sample.

From the observation, we see that slower growth is required for lower hexagonal content in cubic GaN. However, if the sample was grown over many hours to obtain a thick layer, there would be problems such as depletion of Ga and N fluxes. Such problems also occur even when growing thicker cubic GaN layers at reasonable growth rate. Therefore, we try to keep these conditions as optimal as possible so that the growth of hexagonal material in thick cubic GaN can be suppressed.

4.1.3: PL results for cubic GaN with the variation of wafer position

During the growth, a cubic sample is heated up from the centre of the back surface. Thus, the temperature of the centre part of the sample is much higher and gradually lowers towards the edge where it is clipped to the holder. As the temperature is non-uniformly distributed across the wafer, the density of the hexagonal fraction in cubic GaN might also vary between different positions across the wafer and therefore this will be investigated in this work.

In this work, an undoped cubic GaN wafer with thickness of $7.171\mu\text{m}$ was grown at 680°C . The wafer was then cut into pieces as shown in Figure 4.4(a). The perpendicular cleave edges of the sample indicates that the sample is cubic. The wafer was excited by a laser beam at different distances towards the edge, starting at the centre point. The PL spectra are shown in Figure 4.4(b). The spectra show a clear evidence of hexagonal related emission around 3.42eV that it gets stronger towards the edge. The origin of this emission could be due to free-to-bound transitions in hexagonal GaN [12]. On the other hand, broad PL lines at $\sim 3.25\text{eV}$ may associate to the overlapped emissions from excitonic emissions in cubic GaN and *DA* pair transitions in hexagonal GaN [12, 13].

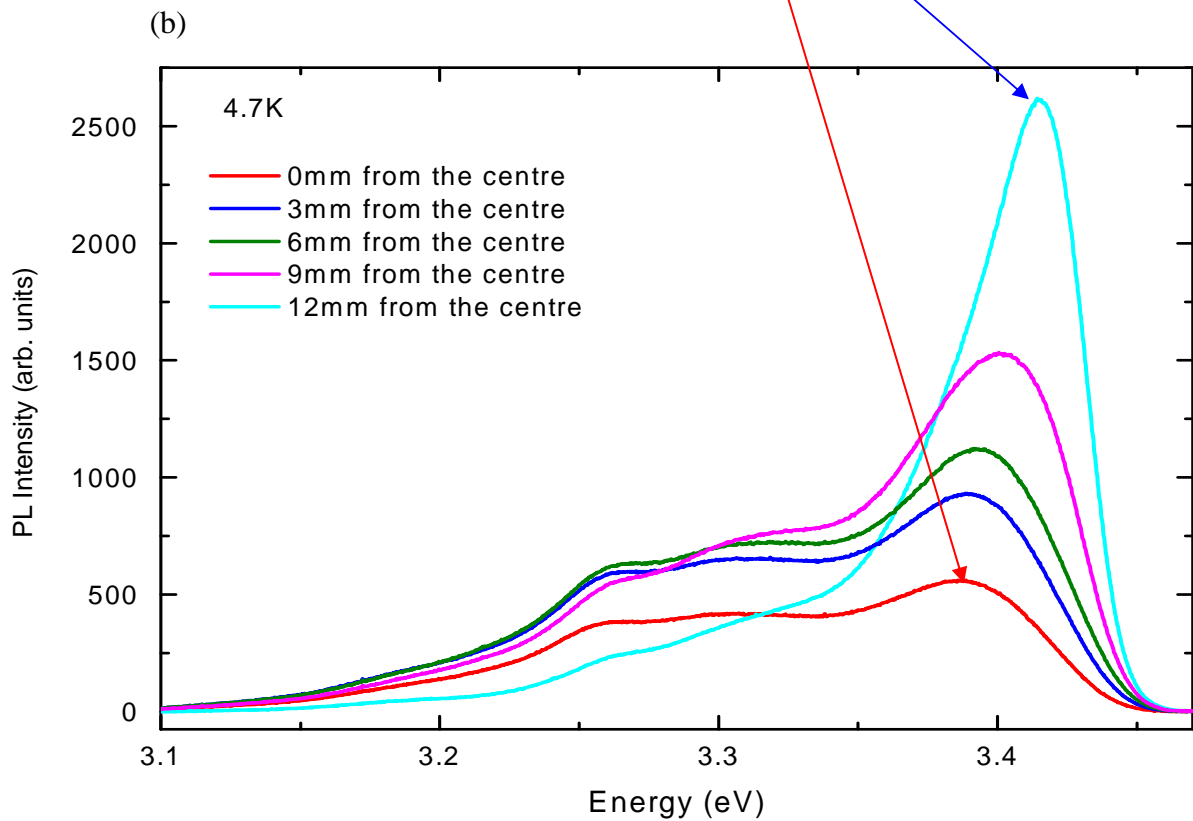
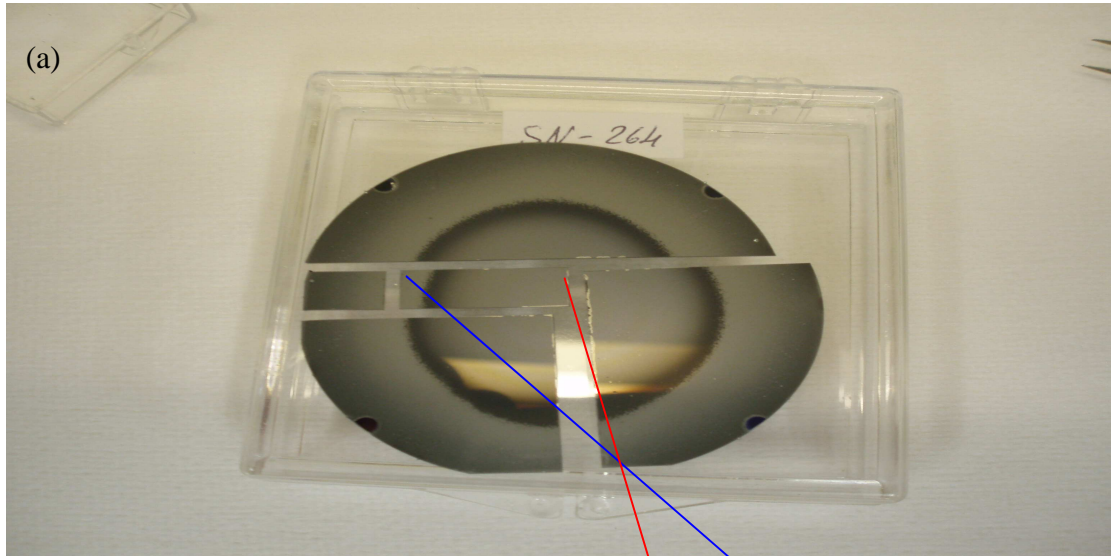


Figure 4.4: (a) A piece of wafer used for PL measurements (b) Dependence of PL intensity of hexagonal/cubic signals as a function of energy at different distance from the centre part of the wafer. Clearly, the PL due to hexagonal material is stronger towards the edge of sample.

At the centre, it can be seen that the cubic PL is almost comparable to the hexagonal PL. This part of the wafer has higher temperature during growth, which leads to

higher surface mobility, thus resulting in the reduction of hexagonal growth in the cubic sample [10, 11]. Furthermore, higher temperature also increases the interaction between the cubic GaN layer and cubic GaAs substrate [10]. Thus, the layer effectively inherits the cubic ‘mode’ from the substrate. If the growth temperature is too high then it causes re-evaporation of Ga and N atoms and therefore cubic GaN can no longer be grown.

Towards the edge, the temperature becomes lower which causes lower surface mobility and thus makes the hexagonal content increase. Further decrease in the temperature close to the edge leads to further reduction of the surface mobility which enhances the growth of the hexagonal phase. Hence, the hexagonal PL becomes even stronger and the luminescence from cubic GaN is considerably weaker. At this point, Ga droplets may form on the surface. The mechanism by which Ga droplet formation enhances the hexagonal inclusion in cubic GaN is not well understood but it has been experimentally observed [9]. This work shows that the centre part of the sample has better cubic crystalline quality and therefore should be used for further analysis and processing².

4.1.4: PL results for cubic GaN with the variation of thickness

Next, the increase of the hexagonal inclusions with the variation of cubic GaN thickness is investigated. In this work, a number of undoped cubic GaN samples were grown near stoichiometric condition with the growth rate of $\sim 0.4\mu\text{m}/\text{hour}$ and the growth temperature around 680°C . Figure 4.5 shows the dependence of the hexagonal PL intensity as the thickness of the cubic layer is changed. From the figure, the intensity of the spectra for thin samples is very weak. However, detailed investigation found that the samples show the three peaks that correspond to the emission in cubic GaN (*please refer to Figure 4.1*) and that the signal due to hexagonal GaN is negligible.

When the thickness increases to $\sim 1.9\mu\text{m}$, the sample starts to show a broad shoulder at lower energy around 3.25eV and this maybe due to the overlap of two broad

² Note that the samples used in section 4.11 and 4.12 were taken from the centre part of the wafer.

signals of excitonic recombination in cubic GaN and *DA* pair transition in hexagonal GaN [12, 13]. At higher energy, another broad signal is observed and it is probably caused by a mixture of various transitions in hexagonal GaN. When the layer was grown at $\sim 12.0\mu\text{m}$, the spectrum is apparently dominated by hexagonal related emission around 3.42eV. However, there is a broad signal with small magnitude around 3.32eV that could be due to emissions related to defects in hexagonal GaN [5].

Similar to the previous report [7], the result shows that the fraction of the hexagonal phase in cubic GaN increases with thickness. When the thickness is increased, the growth conditions, such as III/V ratio, growth rate and temperature, change with time. At this point, the optimal growth for cubic GaN can no longer be sustained, and therefore the growth of the stable phase (hexagonal) starts to increase in the sample.

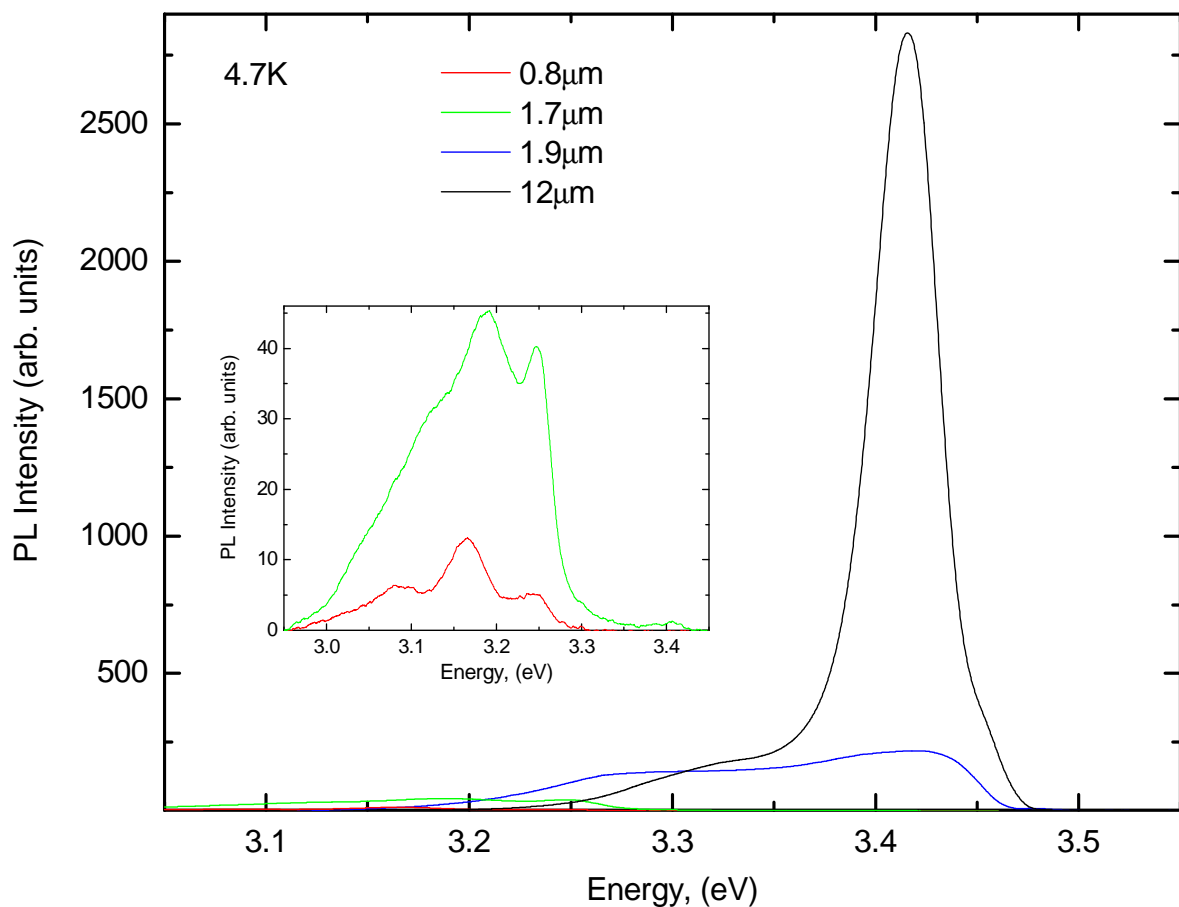


Figure 4.5: PL spectra for cubic GaN samples with different thicknesses. The signal due to hexagonal material is stronger when the thickness is increased. Insert figure shows the large scale for thinner cubic GaN.

Figure 4.6 shows the XRD data for the 12.0 μm thick cubic GaN sample. The peak in intensity related to cubic GaN is observed around 40°. However, there is a small peak at about 35° that probably comes from hexagonal inclusions in cubic GaN or might be due to the formation of (111) cubic GaN stacking faults. It should be noted that the signal of GaAs is observed; showing the penetration depth of XRD is more than 12.0 μm . Therefore data for the whole depth of GaN is collected, whereas the excitation light in the PL measurement penetrates only a few hundred nano-meters into the surface. The origin of a small peak in intensity at $\sim 37^\circ$ is not clear at this stage.

Comparing both measurements, certainly at 12.0 μm , the hexagonal signal is dominant in the PL while the XRD data shows cubic material is dominant. Again, this confirms how sensitive PL is to the hexagonal fraction, particularly when the thickness is increased. On the other hand, the XRD peak that could be related to hexagonal material is about three orders of magnitude smaller than that for cubic, indicating that the total amount of hexagonal content in the sample is still small. This implies that even small incorporation of hexagonal material near the surface results in a strong PL signal. Thus, we strongly propose that the quality of cubic GaN should be characterised through both measurements, especially for thicker layers, where the hexagonal content becomes higher.

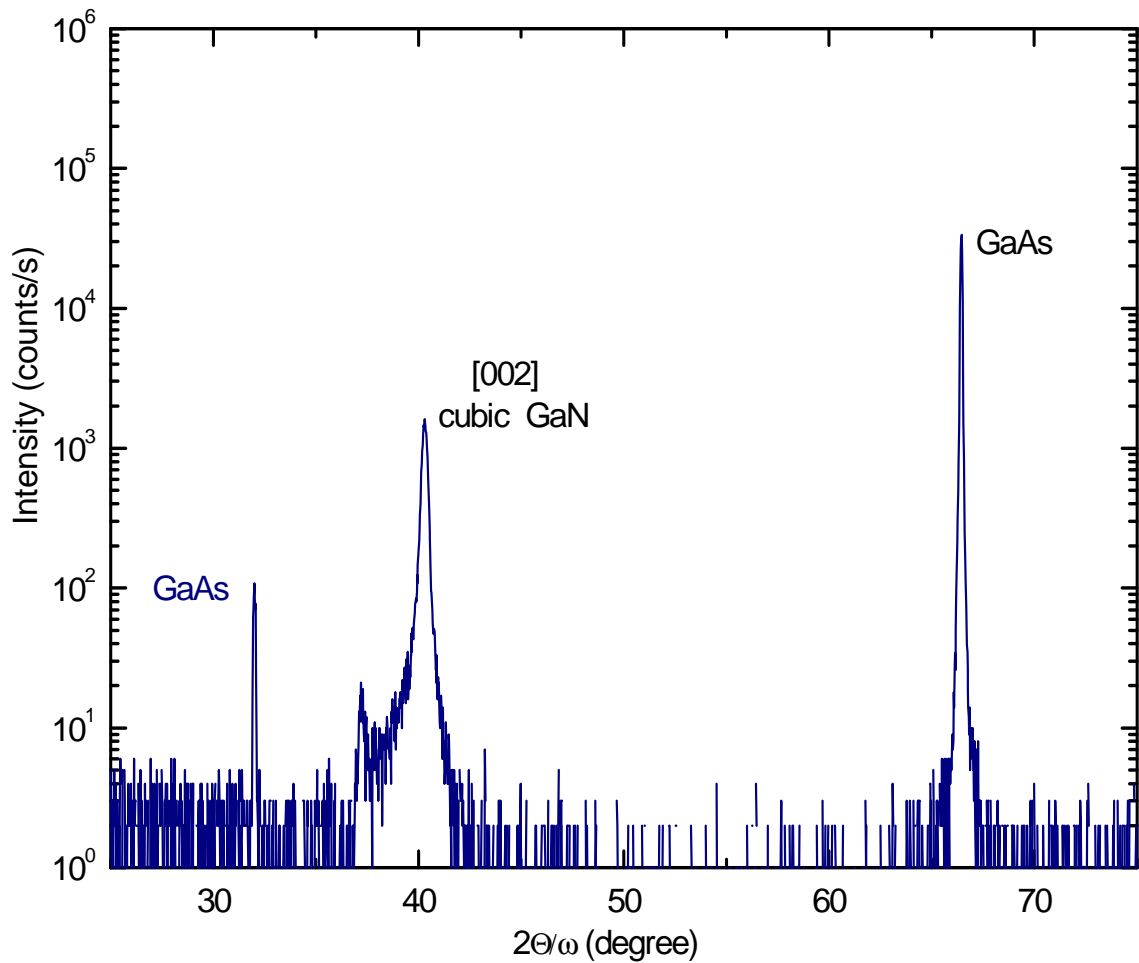


Figure 4.6: XRD data for 12.0 μm thick cubic GaN. The cubic signal in [002] direction is observed around 40°. The peak related to GaAs is coming from the GaAs substrate.

In this work, so far we have demonstrated that cubic GaN is grown better under near-stoichiometric conditions at near the centre of the wafer where the temperature is known and at moderate growth rate. By using these calibration results, we successfully grow thick cubic GaN with low hexagonal inclusions, as has been measured by PL and XRD. Now we will apply these techniques to the growth of bulk cubic GaN.

4.1.5: PL results for bulk cubic GaN

In this work, we aim to increase the thickness of cubic GaN so that it can easily be handled and processed thus making it a suitable substrate for device applications. To

achieve this target, bulk undoped cubic GaN samples were grown using a special approach, where two different growth rates were introduced during the growth. For the first 10 μm thickness, a cubic layer was grown at a slower rate of around 0.4 $\mu\text{m}/\text{hour}$ so that the growth of hexagonal material could be nearly suppressed. The growth rate was then increased to \sim 0.8 $\mu\text{m}/\text{hour}$ in order to build up the thickness of the sample while minimising the overall growth time.

At the initial stage in this work, PL measurement on a \sim 60 μm thick cubic sample was carried out. Like previous measurements, the top side the sample was excited by the laser and there was no luminescence that could be detected, even at higher energy. This is due to the fact that the penetration depth of the excitation light is limited to 0.1 μm depth and thus the data for whole depth of the cubic layer is not measured. In this work, we excited the edge of bulk cubic GaN with tiny laser spot so that the signal from cubic and hexagonal phases over the whole depth could be observed.

In this work, a \sim 50 μm thick cubic sample was carefully cleaved so that a smooth edge was obtained. The sample has cleavage perpendicular planes (similar to what had been observed in Figure 4.4a) which confirms that the sample is mostly cubic. A micro laser beam hit the edge surface and the PL spectra were measured for points between the GaAs/GaN to GaN/vacuum interfaces. Figure 4.7 shows the PL intensity as a function of energy at different depths. It can be seen that there are two small peaks that probably arise from the overlapped signals of excitonic emissions in cubic GaN and *DA* pair transitions in hexagonal GaN at \sim 3.28eV, and emissions related defects in hexagonal GaN at \sim 3.34eV. On the other hand, a strong signal which is due to hexagonal related emission around 3.4eV dominates the PL spectra. Further analysis of the spectra at the peak energy is presented in Figure 4.8.

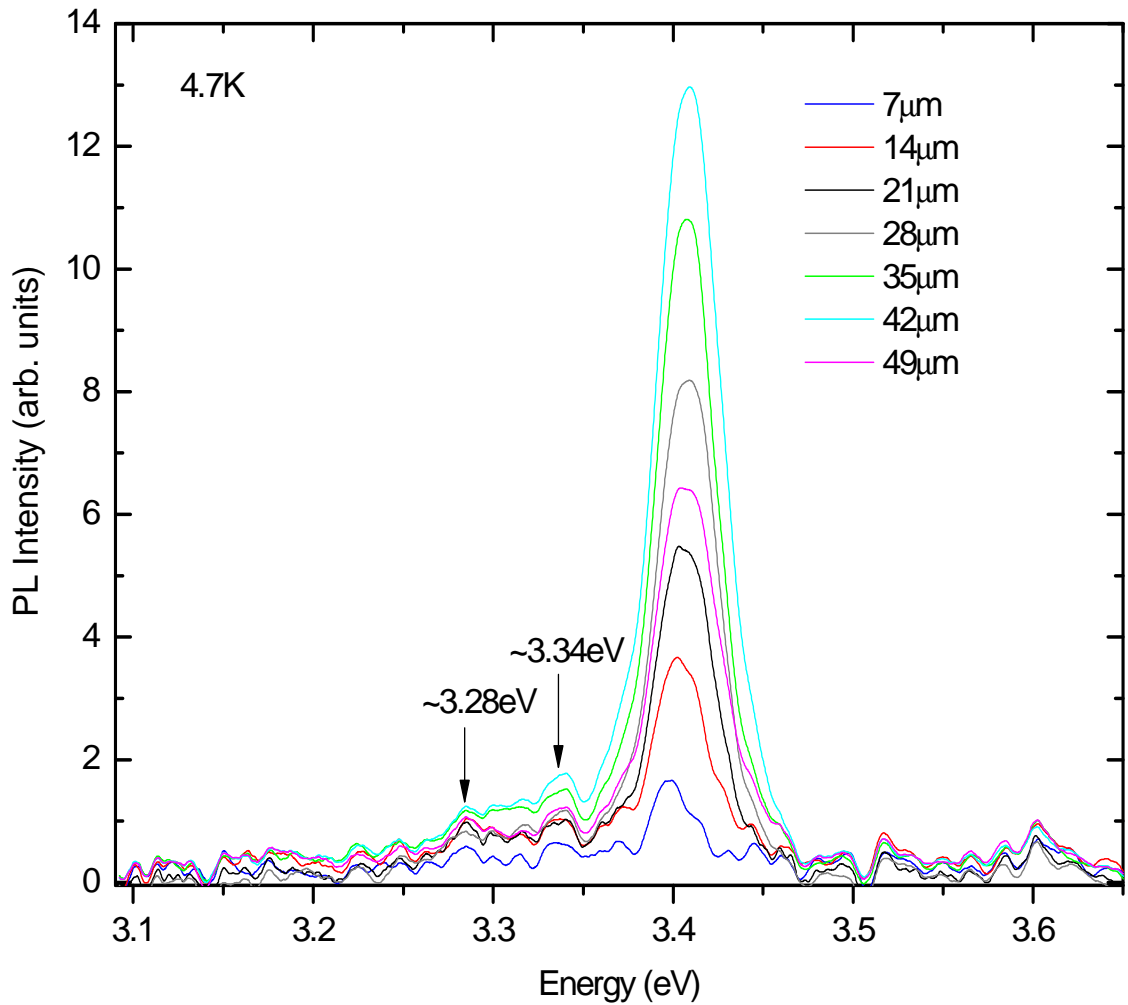


Figure 4.7: PL spectra with the variation of depth in $\sim 50\mu\text{m}$ thick cubic GaN (distances measured from GaAs/GaN interface). The spectra are clearly dominated by hexagonal related emission.

Figure 4.8 shows the increase of hexagonal PL (at the energy of 3.4eV) with the variation of depths. Apparently, the intensity increases with thickness and this correspondingly reflects that the hexagonal inclusions increase with thickness. However, at further distance towards the edge of the sample, the intensity reduces due to the finite spot size of the laser beam moving off the edge of the sample. The data from earlier Nuclear Magnetic Resonance (NMR) measurements [14] found that the average hexagonal content in our thick cubic GaN samples is about 10%. By using this result, the luminescence intensity is calibrated in order to estimate the approximate percentage of hexagonal material in the sample as a function of thickness [a detailed description of the PL calibration procedure is given in Appendix]. The result is shown in the same figure. From this observation, it is shown

that the hexagonal fraction is just a few percent close to the GaAs/GaN interface, which would therefore appear to be the best surface to use for further growth. In fact, even at 50 μm , the hexagonal fraction is less than 20%, which is much better than some thin layers in earlier works.

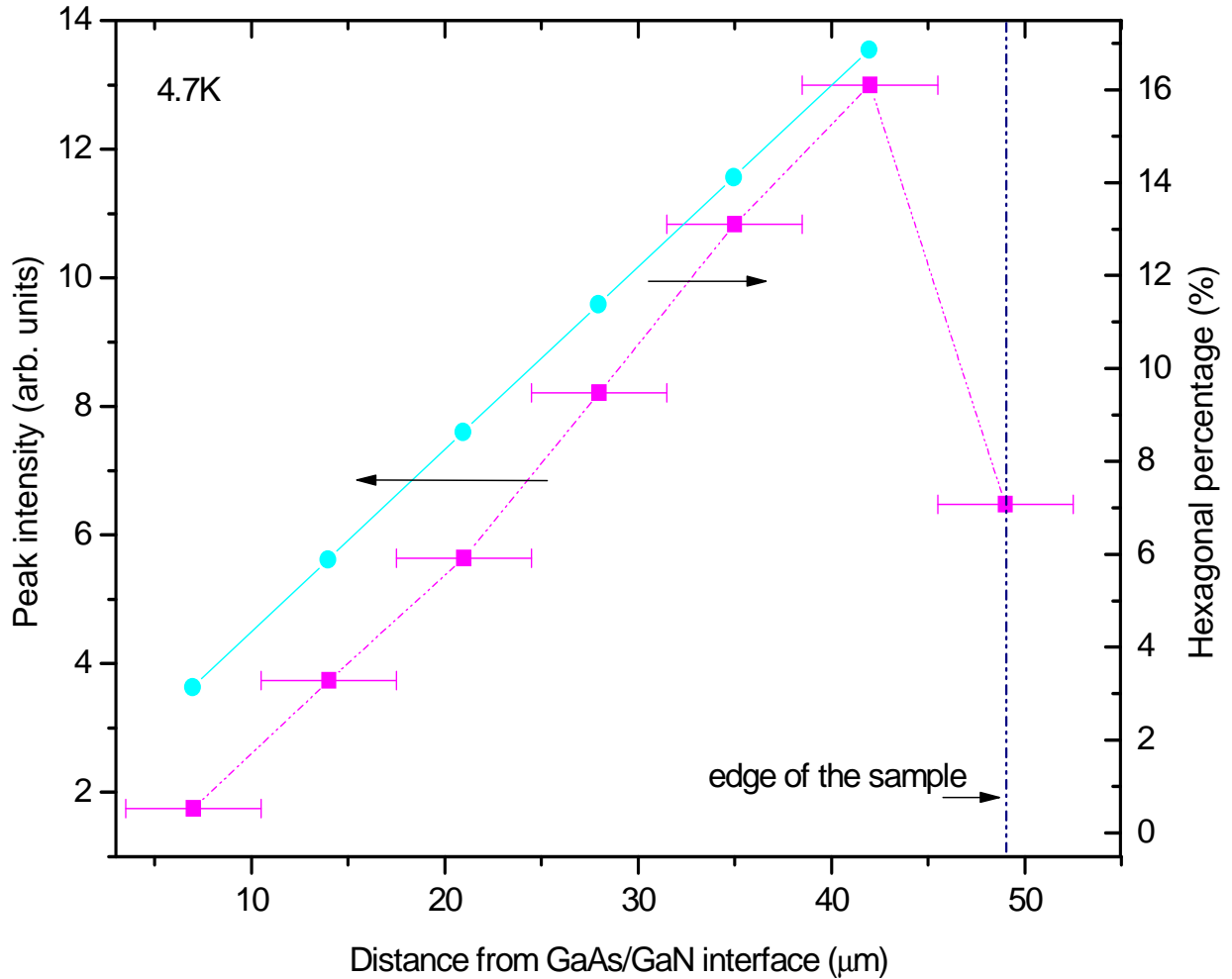


Figure 4.8: The PL intensity of hexagonal (dashed line with full-square) and the percentage of hexagonal inclusion (solid line with full-circle) as functions of depth for a $\sim 50\mu\text{m}$ thick cubic GaN. The point near GaAs/GaN interface corresponds to the start point.

So far in this work, we have successfully demonstrated a bulk cubic GaN layer with a relatively low hexagonal content for the first time. In this work, we also intend to investigate the fundamental properties of cubic GaN, which is presented in the following section.

4.2: THE ELASTO-OPTICAL STUDY ON CUBIC GaN

Up to now, there have been few studies reported on the fundamental properties of cubic GaN. The limitation arises from the difficulty of growing high purity cubic GaN due to its metastable structure. In different experiments, the published values of refractive index of cubic GaN are significantly inconsistent [15-17]. Besides this, data on elastic properties in cubic GaN are scarce and so far limited to only theoretical calculations [18].

In this work, the basic elastic and optical properties of thin bulk GaN (~1 μ m) on a GaAs substrate were measured using the picosecond acoustic technique. The low temperature values of the longitudinal sound velocity, S_{LA}^{GaN} elastic constant, c_{11} and refractive index, n of cubic GaN are determined. The measurements are also performed on hexagonal (wurzite) GaN for comparison. Assistance with the measurement and data analysis was provided by Prof. A.V. Akimov.

4.2.1: The effect of strain pulse on the reflectivity in cubic GaN

At the early stage of this work, the lattice constant of the cubic symmetry of the GaN, a was measured by XRD and the value is found to be 4.54 Å. We calculated the mass of a cubic cell from the molar mass of GaN, $m = 5.60 \times 10^{-22}$ g, which gives the density of the film, $\rho = 5.99$ g cm $^{-3}$. Next, the picosecond acoustic measurement is carried out with the variation of temperature, from 4.7 to 300K. The probe signal, $\frac{\Delta R(t)}{R_0}$ (R_0 is the reflectivity without strain pulses) as a function of the time delay, t between the probe and pump pulses had been measured at low temperature and the result is shown in Figure 4.9 The propagation of the strain pulses through the GaAs substrate occurred in a time $t_0 = l / S_{LA}^{GaAs} = 51$ ns, where $S_{LA}^{GaAs} = 4.8 \times 10^3$ ms $^{-1}$ is the longitudinal (LA) sound velocity in GaAs and $l = 245\mu$ m is the thickness of the GaAs substrate. For a convenience, $t_0 \approx 51$ ns is subtracted to give $t=0$ corresponding to the time when the strain pulse arrives at GaN layer. The measured signal consists of four peaks (1-4); two peaks (1 and 3) have $\Delta R(t) < 0$ while the other peaks (2 and 4) have $\Delta R(t) > 0$. Each peak is separated by the equidistant time interval $\Delta t = 193 \pm 7$ ps. In

the time interval $t = 75\text{-}200\text{ps}$, an oscillatory behaviour is clearly observed and the detail is given in Figure 4.10(a).

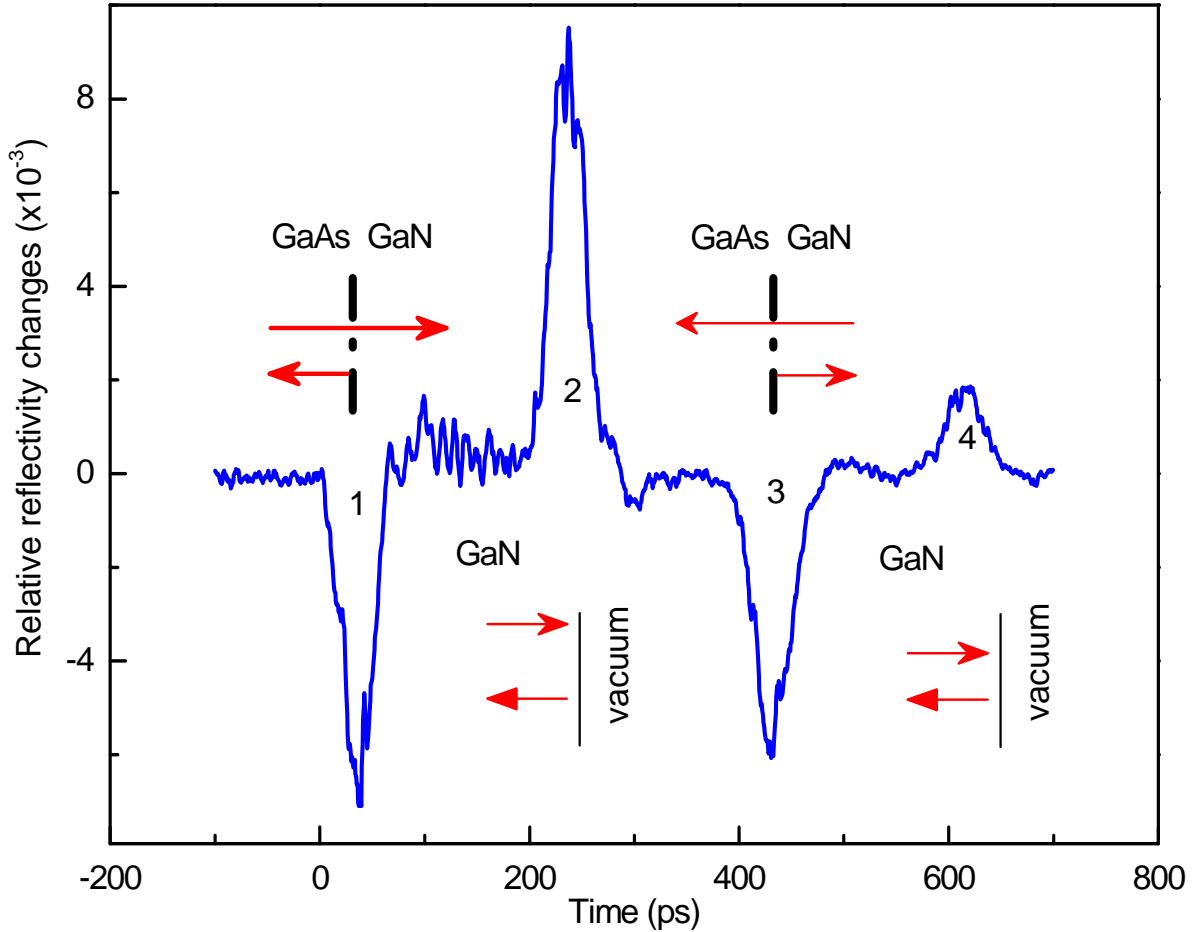


Figure 4.9: The change of the reflectivity of the cubic GaN film as a function of the time delay between the probe pulse and the arrival time of the strain pulse at the GaN film. The peaks labelled 1-4 show the strain pulse passing the related interfaces.

The effect of the strain pulse on the reflectivity, $\Delta R(t)$ (as shown in Figure 4.9) is commonly observed in various materials in earlier experiments. There are two well-known mechanisms that cause the change of the reflectivity, $\Delta R(t)$. Firstly, the dynamical change of film thickness is induced as the strain pulse passes the film interfaces. As a result, the interfering probe beams reflected from the two film interfaces experience a dynamical phase shift. Secondly, the strain in the material induces modulation of the refractive index. This causes coherent Brillouin oscillations of the probe signal while the strain pulse propagates between the film

interfaces. Figure 4.10(a) shows the oscillatory behaviour in between 75 and 200ps that exhibits the Brillouin oscillations when the strain pulse transverses the GaN film, from one interface to another. Figure 4.10(b) shows the Fourier transform of the temporal signal.

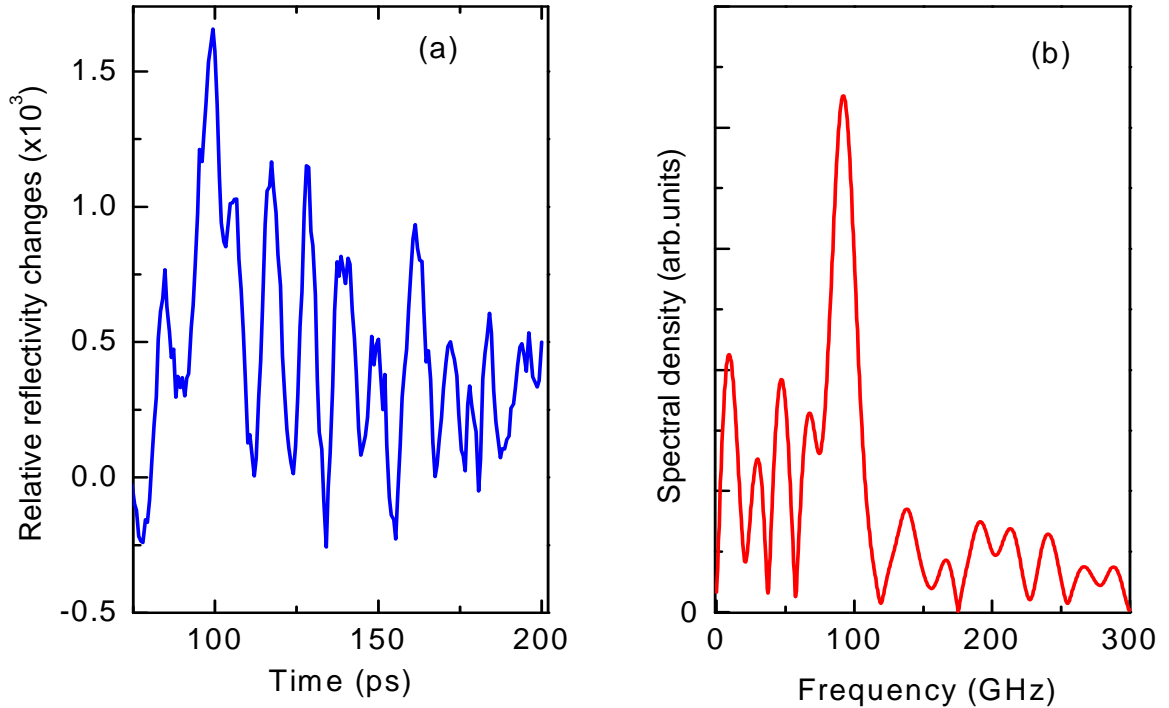


Figure 4.10: (a) The change of reflectivity from cubic GaN film as a function of the time delay. (b) The Fourier transform of the temporal signal.

4.2.2: Measuring sound velocity, elastic constant and refractive index in cubic GaN

From Figure 4.9, peaks 1 and 3 correspond to the time when the strain pulse passes the GaN/GaAs interface and peaks 2 and 4 correspond to the arrival of strain pulses at the GaN/vacuum interface. The amplitudes of pulses 1 and 3 with $\Delta R(t) < 0$ are almost identical, showing the negligible incoherent scattering at the GaN/vacuum interface. The difference in amplitudes of the pulses 2 and 4 with $\Delta R(t) > 0$ is due to the reflection of the strain pulse at the GaN/GaAs interface. Therefore, the ratio of the amplitudes for pulses 4 and 2 is equal to the reflectivity coefficient, R of the

longitudinal sound at the GaN/GaAs interface and R can be calculated using acoustic mismatch theory given by:

$$R = \left| \frac{Z^{GaN} - Z^{GaAs}}{Z^{GaN} + Z^{GaAs}} \right| \quad (2)$$

where Z^{GaN} and Z^{GaAs} are the acoustic impedances of GaN and GaAs, respectively.

It is well known that the value of Z^{GaAs} is given by $\rho^{GaAs} \mathcal{S}_{LA}^{GaAs} = 2.541 \times 10^6 \text{ g/cm}^2\text{s}$. The measured value of R is 0.24 ± 0.01 and from Equation (2), the value of sound velocity, \mathcal{S}_{LA}^{GaN} is $(6.9 \pm 0.1) \times 10^3 \text{ m/s}$ and the corresponding elastic constant, $c_{11} = (\mathcal{S}_{LA}^{GaN})^2 \rho^{GaN}$ is $285 \pm 8 \text{ GPa}$. The value for c_{11} from this measurement is in good agreement with the calculated value of c_{11} [18].

The strain pulse is a coherent excitation of vibrational modes of the crystal lattice (coherent phonons). Hence, there is scattering between photons and phonons that influences the Brillouin backscattering oscillations as shown in Figure 4.10(a). This oscillation is dominated by the momentum conservation law $\mathbf{k}_{\text{phonon}} = -2\mathbf{k}_{\text{photon}}$, where $\mathbf{k}_{\text{phonon}}$ and $\mathbf{k}_{\text{photon}}$ are the wave vectors of a phonon mode in the strain pulse and photon in the probe beam, respectively. Figure 4.10(b) shows the Fourier spectrum of Figure 4.10(a) and the oscillation frequency, f is found to be $91 \pm 2 \text{ GHz}$. By using this f , the value of refractive index in cubic GaN at low temperature is derived by:

$$n = \left(\frac{\lambda f}{2 \mathcal{S}_{LA}^{GaN}} \right)^2 + \sin^2 \alpha \quad (3)$$

where α is the angle of incidence of the probe beam.

Based on the experiment, $\lambda = 400\text{nm}$ and $\alpha = 20^\circ$. This gives $n = 2.63 \pm 0.04$ at 4.7K . The thickness of GaN film can be calculated by $d = \mathcal{S}_{LA}^{GaN} \Delta t = 1.33 \pm 0.04 \mu\text{m}$.

Furthermore, the dependences of \mathcal{S}_{LA}^{GaN} , c_{11} and n on temperature were investigated. From the experiment, the measured values did not change within the experimental

error although the temperature, T was increased up to 100K. However, higher temperature (above 100K) generates strong acoustic scattering in the GaAs substrate that causes the picosecond strain pulse not to reach the GaN film [19]. For comparison, a similar measurement was carried out on hexagonal GaN films (using sapphire substrates) over a wider temperature range from 4.7K to 250K. The sound velocity, S_{LA}^{GaN} for hexagonal GaN is found to be $(8.4 \pm 0.3) \times 10^3 \text{ ms}^{-1}$ and it does not depend on T within experimental error. This experiment reveals that the sound velocity in GaN varies considerably in different crystallographic structures.

4.2.3: The dependence of the refractive index on photon energy in cubic GaN

By knowing a precise value of the thickness, d from the picosecond acoustic measurement, the refractive index, n and its dependence on photon energy can be plotted by a standard optical reflectivity measurement. Figure 4.11 shows the reflectivity spectrum of the cubic GaN film measured at normal incidence at room temperature. The Fabry-Perot oscillations are clearly observed and the refractive index may be derived from the Bragg conditions for the wavelength λ_{\min} at the N^{th} order of the reflectivity minima: $N\lambda_{\min} = 2nd$.

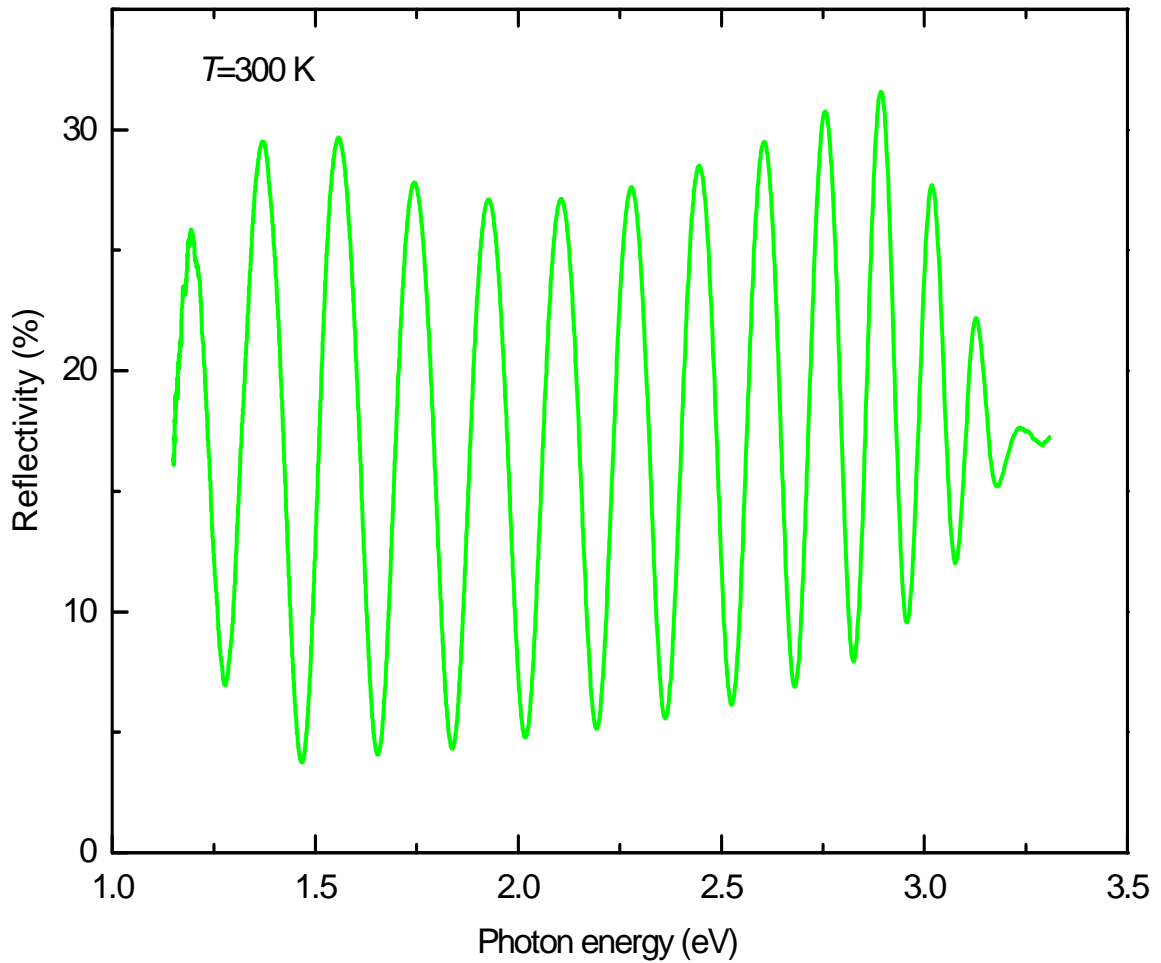


Figure 4.11: The Fabry-Perot oscillations in cubic GaN film at room temperature.

Figure 4.12 shows the dispersion curve for the derived refractive index at room temperature. This result agrees with the previous experimental observation at one energy by precise ellipsometric measurement [15]. For comparison, the derived refractive index from the picosecond acoustic measurement at 4.7K is included. The derived refractive index at low temperature with the photon energy $E = 3.09\text{eV}$ is smaller than at room temperature due to the blue shift of cubic GaN band gap when T decreases [20]. The measured values for elasto-optical properties in cubic GaN are summarised in Table 4.1.

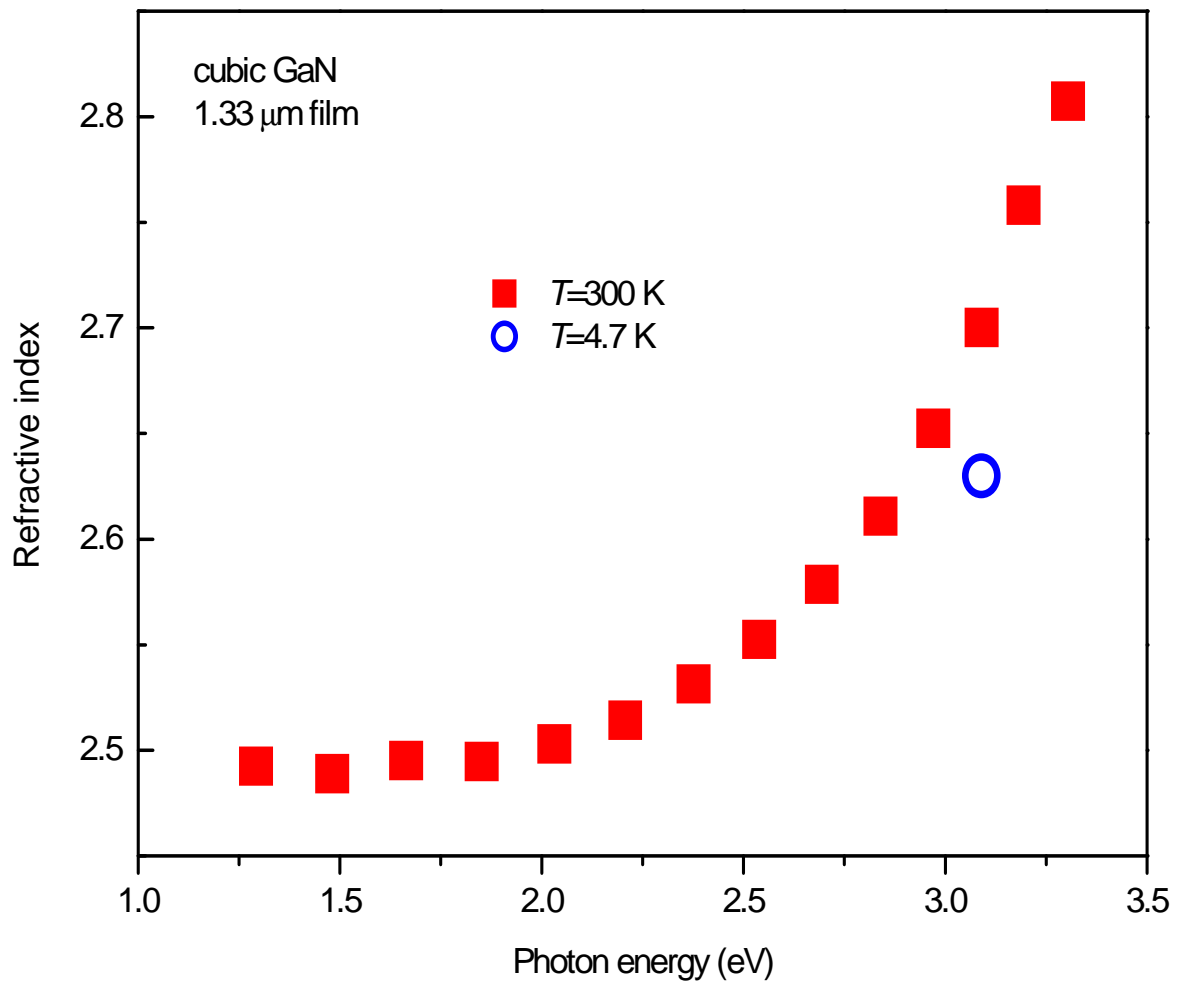


Figure 4.12: The dependence of the derived refractive index on photon energy for cubic GaN film at room temperature. The refractive index increases exponentially with the photon energy. The derived refractive index at low temperature is included for comparison.

Table 4.1: Elasto-optical parameters for cubic GaN. The respective values for hexagonal GaN are given for a comparison.

	<i>c-GaN</i>	<i>h-GaN</i>
Density (g/cm ³)	5.99	6.15
Longitudinal sound velocity, S_{LA}^{GaN} x10 ³ (m/s)	(6.9±0.1)	8.0[21]
Elastic constant, c_{11} (GPa)	285±8 287 [18]	
Refractive index at 3.09eV		
$T=300K$	2.07±0.04	
$T=4.7K$	2.63±0.04	2.54[22]

4.3: STUDIES OF ELECTRICAL TRANSPORT IN CUBIC GaN

While material quality remains an issue, the doping process is also important to improve/modify the conductivity in a semiconductor and make it useful for device applications. Nowadays, doping is required for constructing p-n and p-i-n junctions providing carriers for devices such as high electron mobility transistors (HEMTs) as well as for creating doped substrate such as n⁺ substrate for resonant tunnelling diodes (RTDs) and laser diodes (LDs). Due to the importance of doping in semiconductor devices, we investigate the electrical properties of cubic GaN samples with the variation of dopants and thickness. This work is described in the following section. The samples were measured by Hall Effect at room temperature.

4.3.1: Electrical properties in cubic GaN with the variation of dopants

At the early stage of this work, 0.5µm thick cubic GaN samples, doped with different types of dopants had been grown by MBE Gen-II system. Samples 1 and 2 are undoped samples. Samples 3 and 4 were doped with Carbon (C) and Manganese (Mn), respectively, while sample 5 was doped with Si donors. Table 4.2 shows the summary results for these samples.

Table 4.2: The electrical properties in cubic GaN samples doped with different dopants.

Sample	Thickness of cubic GaN (μm)	Dopant	Conductivity (type)	Carrier density (cm^{-3})	Mobility (cm^2/Vs)
1	~0.5	-	n	6.14×10^{19}	5.10
2	~0.8	-	n	6.40×10^{19}	5.85
3	~0.5	C	n	1.46×10^{20}	2.32
4	~0.5	Mn	p	1.81×10^{19}	2.33
5	~0.5	Si	n	1.13×10^{20}	3.59

The undoped cubic GaN samples are found to be n-type and this is likely due to the Oxygen (O) impurity that exists in the growth system. The electron concentration and mobility for the samples are approximately $6 \times 10^{19} \text{cm}^{-3}$ and $5 \text{cm}^2/\text{Vs}$, respectively. The electron concentration value is somewhat high and this implies the possibility of a high density of residual donors in our samples. However, this has been typically observed for the case of undoped hexagonal GaN [23, 24]. The mobility of carriers is found to be very low and this might be due to high impurity concentration [25] and intrinsic defects [26] that limit the carrier transport properties in the sample.

Carbon doped cubic GaN also showed n-type characteristic. Technically, Carbon has an amphoteric nature where it can be a donor or acceptor, respectively. However, from our observation, it is suggested that C atoms tend to be incorporated at Ga-sites in the sample and act as donors. This is perhaps due to the influence of the growth conditions. The sample has a high electron concentration of $1.46 \times 10^{20} \text{cm}^{-3}$ and low carrier mobility of $2.32 \text{cm}^2/\text{Vs}$, respectively. This is expected as high residual impurities and intrinsic defects already exist in the sample.

In this work, cubic GaN had been successfully doped with Mn. During the doping, the Mn atoms serve as an effective acceptor to compensate high residual donors in cubic GaN. Therefore, the hole concentration is found to be around $1.8 \times 10^{19} \text{cm}^{-3}$. The sample has low carrier mobility, which is about $2.3 \text{cm}^2/\text{Vs}$ but this is consistent with what had been normally observed in p-type GaN [27].

In other reports, p-type Mn doped cubic GaN with a thickness of 300nm had been characterised at room temperature. The hole density and mobility of the sample are about 10^{18}cm^{-3} and $300\text{cm}^2/\text{Vs}$, respectively [28]. This mobility value is much larger than that in our measured sample. It is suggested that the difference in growth methods and conditions used to grow the samples may lead to different intrinsic impurities and defects, consequently affecting the electrical properties.

Si doped cubic GaN shows n-type characteristics with carrier density and electron mobility about $1.137 \times 10^{20}\text{cm}^{-3}$ and $3.6\text{cm}^2/\text{Vs}$, respectively. From the measurement on undoped cubic GaN, these values are expected to be due to poor quality of the sample. However, the result is quite comparable to another experiment by As et al [29]. They reported that the maximum free electron concentration is around $5 \times 10^{19}\text{cm}^{-3}$ with an electron mobility of $75\text{cm}^2/\text{Vs}$.

4.3.2: Electrical properties in cubic GaN with the variation of thickness

In addition, we study the electrical properties of undoped cubic GaN with the variation of thickness. In this work, cubic GaN samples were grown by a homemade mini MBE system at University of Nottingham by Dr. S.V. Novikov. Figure 4.13 illustrates the structures with the thickness of the top layer, d . The measured values are tabulated in Table 4.3.

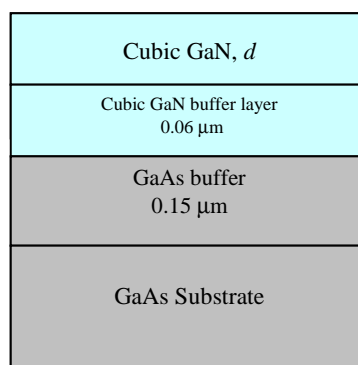


Figure 4.13: The sample structure with the variation of thickness, d .

Table 4.3: The electrical properties of undoped cubic GaN samples with different thickness, d obtained from the experiment.

Sample	Thickness of GaN (μm)	Conductivity	Carrier density (cm^{-3})	Mobility (cm^2/Vs)
MS-707	0.58	p-type	9.59×10^{18}	1.46
MS-717	1.20	p-type	1.74×10^{18}	1.80
MS-718	27.60	n-type	3.08×10^{18}	2.82
MS-730	30.00	p-type	1.45×10^{17}	12.38

The above table clearly shows that the electrical properties of the undoped cubic GaN samples vary with the thickness. The thin samples show p-type behaviour with a high carrier density but lower mobility. However, in previous measurement, the thin undoped MBE-Gen II samples showed n-type behaviour. The difference between the results is probably due to the different growth conditions in the different growth machines, which affect the unintentional incorporation of impurities and intrinsic defects during the growth process.

The sample with the thickness of $\sim 27\mu\text{m}$ shows n-type behaviour. Similar to the thin samples, this sample has high carrier density with low mobility. However, the $\sim 30\mu\text{m}$ thick sample shows p-type behaviour. The variation of these results can be explained by this fact: longer growth leads to fluctuation in Ga and N fluxes as well as the growth temperature with time. Equally, these effects may change the electrical properties of the sample.

The mobility values suggest impurity and defect densities in the thin cubic GaN are also high and this is similar to the case of the MBE Gen-II samples. For thicker cubic GaN, the residual impurities and defects are lower, which lead to higher mobility. This is consistent with our previous PL result shown in Figure 4.5, where the DA pair transitions are weaker as the thickness is increased. We cannot confirm if there is a dependence of thickness on the residual carrier density and mobility as we don't have enough statistics and data to explain this behaviour. However, we know that the samples could be grown under different conditions even for different pieces of the same wafer (refer to the earlier section on PL measurement across wafer in section 4.1.3).

4.4: PL RESULTS FOR CUBIC $\text{Al}_x\text{Ga}_{1-x}\text{N}$

In this work, some samples of undoped cubic $\text{Al}_x\text{Ga}_{1-x}\text{N}$ with different Al content, x and thickness have also been characterised. Table 4.4 shows the details of the samples.

Table 4.4: Detailed specification of cubic $\text{Al}_x\text{Ga}_{1-x}\text{N}$ samples with the variation of Al content, x and thickness.

Sample	Al composition	Thickness (μm)
SN-365	0.0	~7.400
SN-368	0.0	~5.967
SN-369	0.1	~0.500
SN-371	0.1	~0.502
SN-372	0.1	~5.860
SN-370	0.2	~0.482
SN-373	0.2	~0.485

Figure 4.14 shows examples of PL spectra for cubic GaN sample (SN-368) and cubic $\text{Al}_{0.2}\text{Ga}_{0.8}\text{N}$ (SN-370). Based on our observation on the optical properties of cubic GaN, peak at ~3.26eV is due to excitonic emissions and two peaks at higher energies may correspond to emissions in hexagonal GaN. On the other hand, a signal at ~3.97eV in cubic $\text{Al}_{0.2}\text{Ga}_{0.8}\text{N}$ is unidentified. It might be related to emission in cubic $\text{Al}_{0.2}\text{Ga}_{0.8}\text{N}$ or hexagonal $\text{Al}_{0.2}\text{Ga}_{0.8}\text{N}$. However we intend to speculate the origin of this peak.

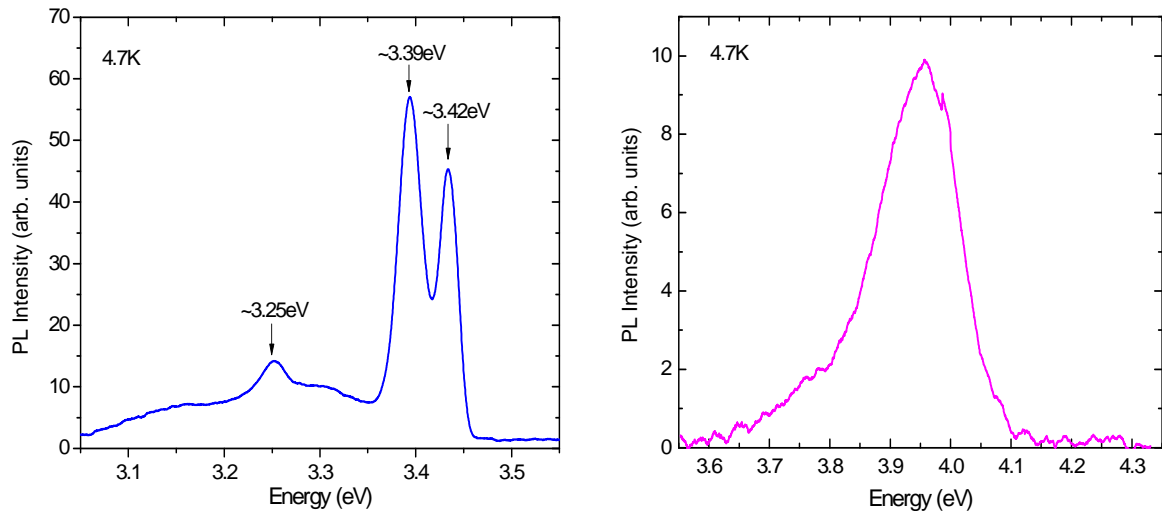


Figure 4.14: PL spectra for cubic GaN (SN-368) and cubic $\text{Al}_{0.2}\text{Ga}_{0.8}\text{N}$ (SN-370) at low temperature.

In the work, we intend to estimate the origin of the peak emissions that had observed in all samples in Table 4.4. Therefore we prepare a figure, that includes the calculated energy gap for hexagonal $\text{Al}_x\text{Ga}_{1-x}\text{N}$ and cubic $\text{Al}_x\text{Ga}_{1-x}\text{N}$ as a function of Al content, x at low temperature (lines) so that the origin of the emissions appear in PL spectra can be roughly defined. There were obtained by calculating the band gap energy of $\text{Al}_x\text{Ga}_{1-x}\text{N}$, given by

$$E_g(x) = (1-x)E_g(\text{GaN}) + xE_g(\text{AlN}) - bx(1-x) \quad (1)$$

where $E_g(c\text{-GaN}) = 3.3\text{eV}$ [30], $E_g(c\text{-AlN}) = 5.1\text{eV}$ [31]³ and $b=0.88\text{eV}$ [32]. For the hexagonal system, $E_g(h\text{-GaN}) = 3.5\text{eV}$ [33], $E_g(h\text{-AlN}) = 6.1\text{eV}$ [33] and $b=0.71\text{eV}$ [34]. Figure 4.15 shows the PL peak energy of cubic $\text{Al}_x\text{Ga}_{1-x}\text{N}$ with the variation of Al content and a summary of the results is tabulated in Table 4.5.

³ Up to now, there are very limited works reported on the energy gap for cubic AlN at low temperature. In fact, it was found that cubic $\text{Al}_x\text{Ga}_{1-x}\text{N}$ is shifted from direct to indirect bandgap when the Al content, x is above ~ 0.5 .

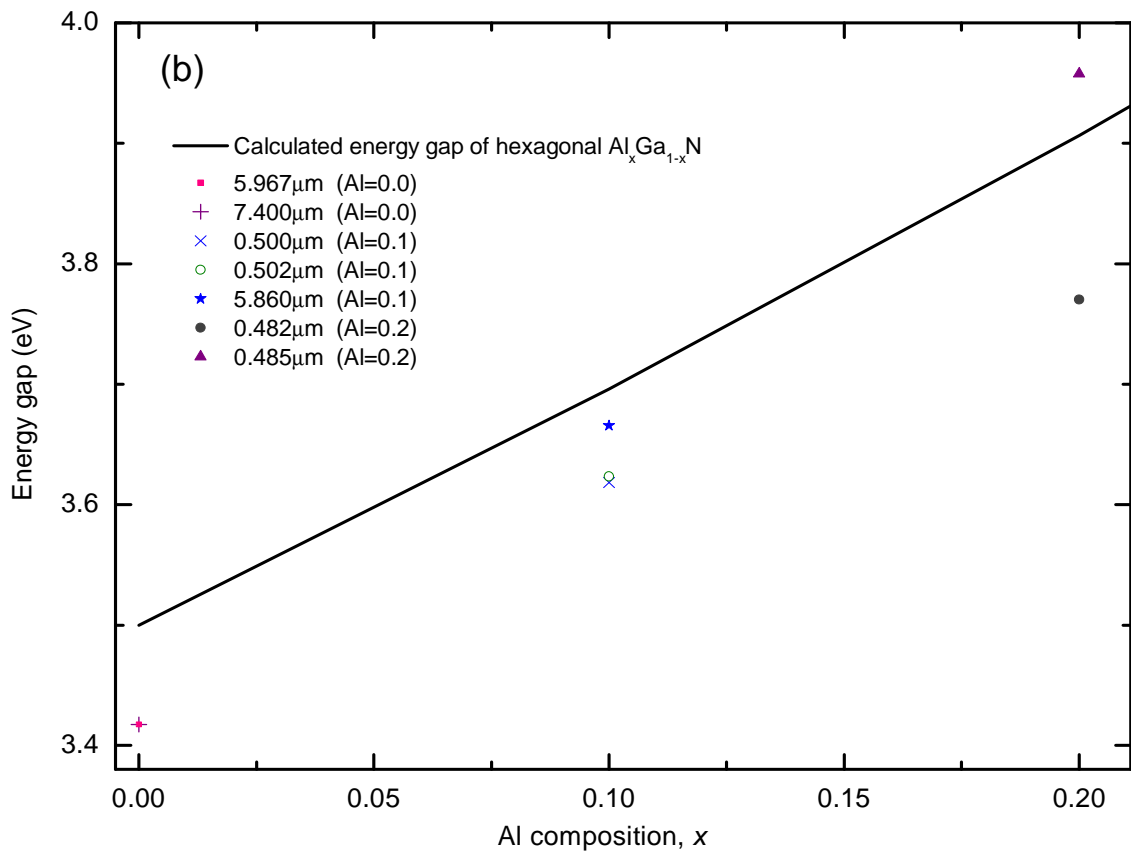
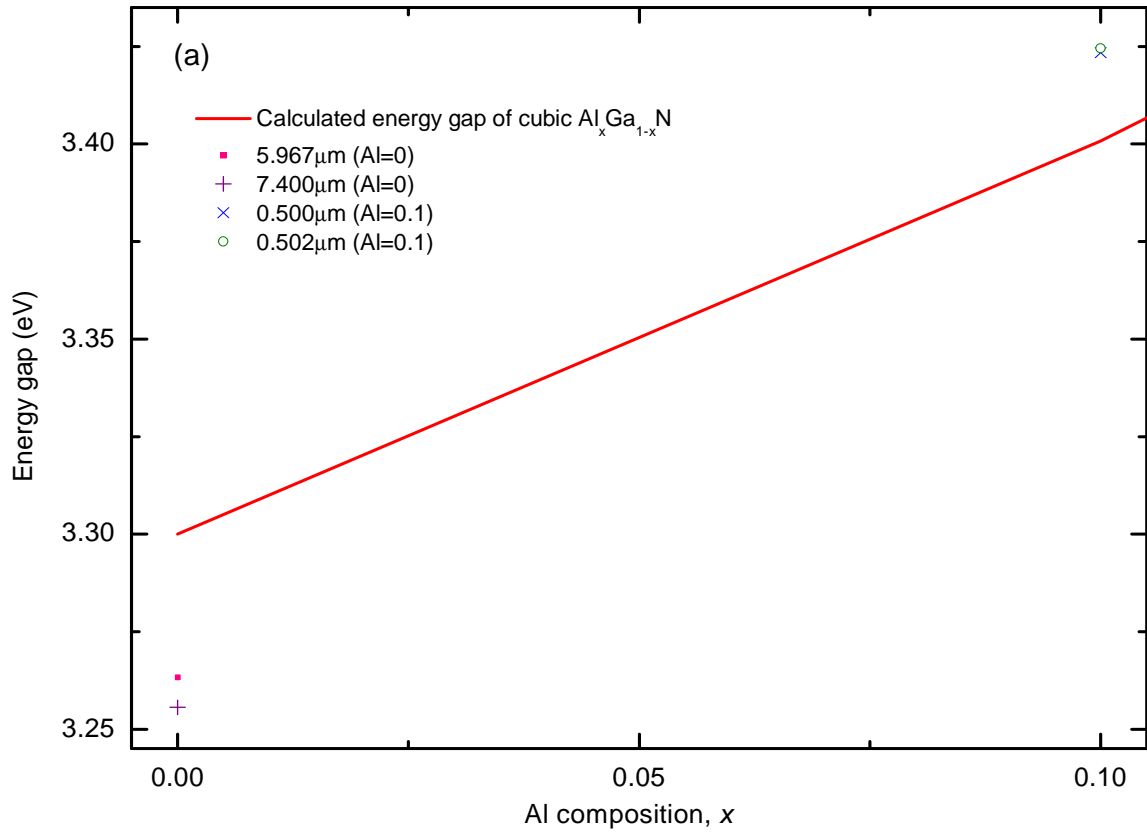


Figure 4.15: The PL peak energy of cubic $\text{Al}_x\text{Ga}_{1-x}\text{N}$ samples with the variation of Al content, x at 4.7K (a) PL peaks that could be due to emission from cubic $\text{Al}_x\text{Ga}_{1-x}\text{N}$ and (b) peaks that could be due to emission from hexagonal $\text{Al}_x\text{Ga}_{1-x}\text{N}$.

Table 4.5: Summary of the peak emission energies in different cubic $\text{Al}_x\text{Ga}_{1-x}\text{N}$ samples.

Sample	Thickness (μM)	Energy emission in Cubic $\text{Al}_x\text{Ga}_{1-x}\text{N}$ (eV)	Energy emission in Hexagonal $\text{Al}_x\text{Ga}_{1-x}\text{N}$ (eV)
GaN	5.967	3.26	3.42
GaN	7.400	3.26	3.42
$\text{Al}_{0.1}\text{Ga}_{0.9}\text{N}$	0.500	3.42	3.62
$\text{Al}_{0.1}\text{Ga}_{0.9}\text{N}$	0.502	3.42	3.62
$\text{Al}_{0.1}\text{Ga}_{0.9}\text{N}$	5.860	-	3.67
$\text{Al}_{0.2}\text{Ga}_{0.8}\text{N}$	0.482	-	3.77
$\text{Al}_{0.2}\text{Ga}_{0.8}\text{N}$	0.485	-	3.96

As can be seen from Figure 4.14 and Table 4.5, the peak emissions in our samples are defined by using the plotted lines for cubic and hexagonal $\text{Al}_x\text{Ga}_{1-x}\text{N}$. From this observation, the thick cubic GaN samples show two peak energies that might be attributed to hexagonal and cubic emissions, respectively. Similar behaviour is also observed for thin cubic $\text{Al}_{0.1}\text{Ga}_{0.9}\text{N}$ samples but for the thick cubic $\text{Al}_{0.1}\text{Ga}_{0.9}\text{N}$ sample, the spectrum is mainly governed by the hexagonal peak. This is consistent with the case for cubic GaN, where hexagonal inclusions increase as the thickness is increased.

When the Al content, x rises up to 0.2, the spectra are strongly dominated by hexagonal signal although the samples are thin. The result seems to show that the increase of hexagonal inclusions in cubic $\text{Al}_x\text{Ga}_{1-x}\text{N}$ is also influenced by the Al content, x . This is probably due to the difficulty of maintaining the growth of cubic $\text{Al}_x\text{Ga}_{1-x}\text{N}$ when the Al content is increased. Furthermore, the miscibility gap between AlN and GaN also increases with Al content, x . In this case, the bond between Al-N becomes stronger and they possibly prefer to grow in the thermodynamically stable hexagonal phase. However, more data and results are required in order to find the precise explanation for this behaviour.

4.5: CONCLUSIONS

In this work, we found that the increase of hexagonal inclusions in cubic GaN is influenced by III/V ratio, position of the wafer and growth rate. Although the hexagonal content increases with the thickness, a bulk cubic GaN has been successfully grown with a low average of hexagonal inclusion around 10% and just a few percent at interface. Based on this work, we propose that both PL and XRD measurements are required for characterising cubic GaN.

In this work, the fundamental properties of cubic GaN have also been investigated. The elasto-optical parameters of a cubic GaN film at low temperature were measured by picosecond acoustic measurements. From the result, the sound velocity is found to be $6.9 \pm 0.1 \text{ kms}^{-1}$ with the elastic constant = $285 \pm 8 \text{ GPa}$ and the refractive index = 2.63 ± 0.04 in cubic GaN. These values differ considerably from those for hexagonal GaN film.

In the electrical investigation, it was found that the undoped cubic GaN samples could be n- or p-type depending on growth conditions. From the measurement, C-doped and Si-doped cubic GaN show n-type characteristic, whereas p-type GaN:Mn was successfully demonstrated. These samples have high electron concentration but low mobility, probably due to poor quality of the samples. Besides, the electrical properties of undoped cubic GaN vary with the thickness and this might be due to fluctuations in growth condition during long growth.

In addition to this work, we extended the growth technology of cubic GaN to cubic $\text{Al}_x\text{Ga}_{1-x}\text{N}$. The optical properties of cubic $\text{Al}_x\text{Ga}_{1-x}\text{N}$ with the variation of Al content, x were studied. From our observation, hexagonal PL starts to dominate the spectra when the Al content, x is increased; probably due to the difficulty of sustaining the growth of cubic $\text{Al}_x\text{Ga}_{1-x}\text{N}$ and also the miscibility gap mechanisms.

The next chapter describes the processing of the bulk cubic GaN to make it as a suitable substrate for device applications. In this project, we intend to grow a device structure on a free standing cubic GaN substrate, using the surface that was in contact with GaAs substrate as the interface has only few percent of hexagonal content.

REFERENCES

1. J. Wu, H. Yaguchi, K. Onabe, R. Ito, Y. Shiraki, *Appl. Phys. Lett.*, (1997). **71**: p. 2067.
2. G. Feuillet, F. Widmann, B. Daudin, J. Schuler, M. Arley, J.L. Rouviere, N. Pelekonos, O. Briot, , *Materials Science and Engineering B*, (1997). **50**: p. 233.
3. D.J. As, F.S. C. Wang, B. Schttker, K. Lischka, *Appl. Phys. Lett.*, (1997) **70** p. 1311.
4. A. Philippe, C.B.-C. M. Vernay, G. Guillot, J. Hübner, B. Daudin, G. Feuillet, *Material Science and Engineering B* (1999). **59** p. 168.
5. R. Liu, A. Bell, F.A. Ponce, *Appl. Phys. Lett.*, (2005). **86**: p. 021908.
6. G.D. Chen, M. Smith, J.Y. Lin, H.X. Jiang, *J. Appl. Phys.*, (1995). **79**: p. 2675.
7. H. Tsuchiya, K. Sunaba, T. Suemasu, F. Hasegawa, *J. Cryst. Growth*, (1999). **198/199**: p. 1056.
8. B. Daudin, G. Feuillet, J. Hubner, Y. Samson, F. Widmann, A. Philippe, C. Bru-Chevallier, G. Guillot, E. Bustarret, G. Bentoumi, A. Deneuveille, *J. Appl. Phys.* , (1998). **84**: p. 2295.
9. L.W. Sung, H.H. Lin, C.T. Chia *J. Cryst. Growth*, (2002). **241**: p. 320.
10. C.H. Wei, Z.Y., Xie, L.Y. Li, Q.M. Yu, J.H. Edgar, *J. Electronic Materials*, (2000). **29**: p. 317.
11. M. Funato, M. Ogawa, T. Ishido, Sz. Fujita, *Phys. Stat. Sol. (a)* (1999). **176** p. 509
12. A.V. Andrianov, D.E. Lacklison, J.W. Orton, D.J. Dewsnip, S.E. Hooper, C.T. Foxon, *Semicond. Sci. Technol.*, (1996). **11**: p. 366.
13. L. Eckey, J.-C. Holst, P. Maxim, R. Heitz, A. Hoffman, I. Broser, B.K. Meyer, C. Wetzel, E.N. Mokhov, P.G. Baranov, *Appl. Phys. Lett.*, (1996). **68**: p. 415.
14. S.V. Novikov, N.M. Stanton, R.P. Campion, C.T. Foxon, A.J. Kent, *J. Cryst. Growth*, (2008). **310**: p. 3964.
15. U. Köhler, D.J. As, B. Schöttker, T. Frey, K. Lischka, *J. Appl. Phys.*, (1999). **85** p. 404.
16. A. Vidal, G. Ramirez-Flores, H. Navarro-Contreras, A. Lastras-Martinez, R.C. Powell, J.E. Greene, *Appl. Phys. Lett.* , (1996). **68**: p. 441.
17. E. Lin, B.N. Sverdlov, S. Strite, H. Morkoc, A.E. Drakin, *Electron. Lett.*, (1993). **29**: p. 1759
18. A.F. Wright, *J. Appl. Phys.*, (1997). **82** p. 2833.
19. W. Chen, H.J. Maris, Z.R. Wasilewski, S.I. Tamura, *Philos. Mag. B* (1994). **70**: p. 687.
20. Y.P. Varshini, *Physica (Amsterdam)* (1967). **34**: p. 149.
21. U. Özgür, C.-W. Lee, H.O. Everitt *Phys. Rev. Lett.*, (2001). **86** p. 5604.
22. A. Billeb, W., Grieshaber , D. Stocker, E. F. Schubert, *Appl. Phys. Lett.* , (1997). **70** p. 2790.
23. B-C. Chung, M. Gershenson, *J. Appl. Phys.*, (1992). **72**: p. 651.
24. C. Wetzel, T. Suksi, J.W. Ager III, E.R. Weber, E.E. Haller, S. Fischer, B.K. Meyer, R.J. Molnar, P. Perlin, *Phys. Rev. Lett.*, (1997). **78**: p. 3923.
25. N. G. Weimann, L. F. Eastman, *J. Appl. Phys.*, (1998). **83**: p. 3656.
26. E. Valcheva, T. Paskova, B. Monemar, *Journal of Physics: Condensed Matter*, (2002). **14**: p. 13269.

27. C. C. Yu, C. F. Chu, J.Y. Tsai, S.C. Wang, *Material Science and Engineering B*, (2001). **82**: p. 82.
28. S.V. Novikov, K.W. Edmonds, L.X. Zhao, A.D. Giddings, K.Y. Wang, R.P. Campion, C.R. Staddon, M.W. Fay, Y. Han, P.D. Brown, M. Sawicki, B.L. Galagher, C.T. Foxon, *J. Vac. Sci. Technol. B*, (2005). **23**: p. 1294.
29. D.J. As, T. Simonsmeier, J. Busch, B. Schöttker, M. Lübbers, J. Mimkes, D. Schikora, K. Lischka, W. Kriegseis, W. Burkhardt, B.K. Meyer, *MRS Internet J. Nitride Semicond. Res.* , (1999). **4S1** p. G 3.24.
30. K.H. Ploog, O. Brandt, H. Yang, A. Trampert, *Thin Solid Films* (1997). **306**: p. 231.
31. T. Suzuki, H. Yaguchi, H. Okumura, Y. Ishida, S. Yoshida, *Jpn. J. Appl. Phys.* , (2000). **39**: p. L497.
32. S. Berrah, A. Boukortt, H. Abid, *Semiconductor Phys. Quantum Electronics & Optoelectronics*, (2008). **11**: p. 59.
33. N. Nepal, J. Li, M.L. Nakarmi, J.Y. Lin, H. X. Jiang, *Appl. Phys. Lett.* , (2005). **87**: p. 242104.
34. Z. Dridi, B. Bouhafs, P. Ruterana, *Semicond. Sci. Technol.* , (2003). **18**: p. 850.

CHAPTER 5: PROCESSING OF CUBIC GaN SUBSTRATE

In chapter 4, bulk cubic GaN with low hexagonal content of about 10% has been successfully demonstrated. The size of the layer is ideal for easier handling and processing in an attempt to produce a suitable commercial cubic GaN substrate for device applications. It is also reported that hexagonal inclusions in cubic GaN increase with thickness. Therefore, growing a device or structure on the surface that was in contact with GaAs substrate would seem preferable as it has only few percent of hexagonal content. However, defects due to strain and arsenic (As) inclusions are already generated at the interface between GaN and GaAs substrate. Thus this interface layer needs to be removed so that a cubic device/structure can grow better on top of it.

In this chapter, we report studies on bulk cubic GaN through Secondary Ion Mass Spectroscopy (SIMS), Photoluminescence (PL), X-ray diffraction (XRD) and Atomic Force Microscopy (AFM) measurements. At the end of this work, a device grown on a free standing cubic GaN substrate is demonstrated and its optical properties will be presented.

5.1: COMPOSITIONAL ANALYSIS FOR CUBIC GaN

In this work, the As concentration in our cubic GaN samples were investigated through SIMS measurement. At the first stage in this work, the GaAs substrate had been chemically etched from the samples in order to obtain free standing cubic layers. Figure 5.1 shows the SIMS result for the samples before and after the etching process, corresponding to the data from different sides of the samples. As the penetration depth of the SIMS measurement is limited to $\sim 2.5\mu\text{m}$, a thin cubic GaN layer ($\sim 2\mu\text{m}$) with GaAs substrate was used to estimate the As and N profiles close to the interface which one might obtain with a thicker ($\sim 12\mu\text{m}$) cubic layer.

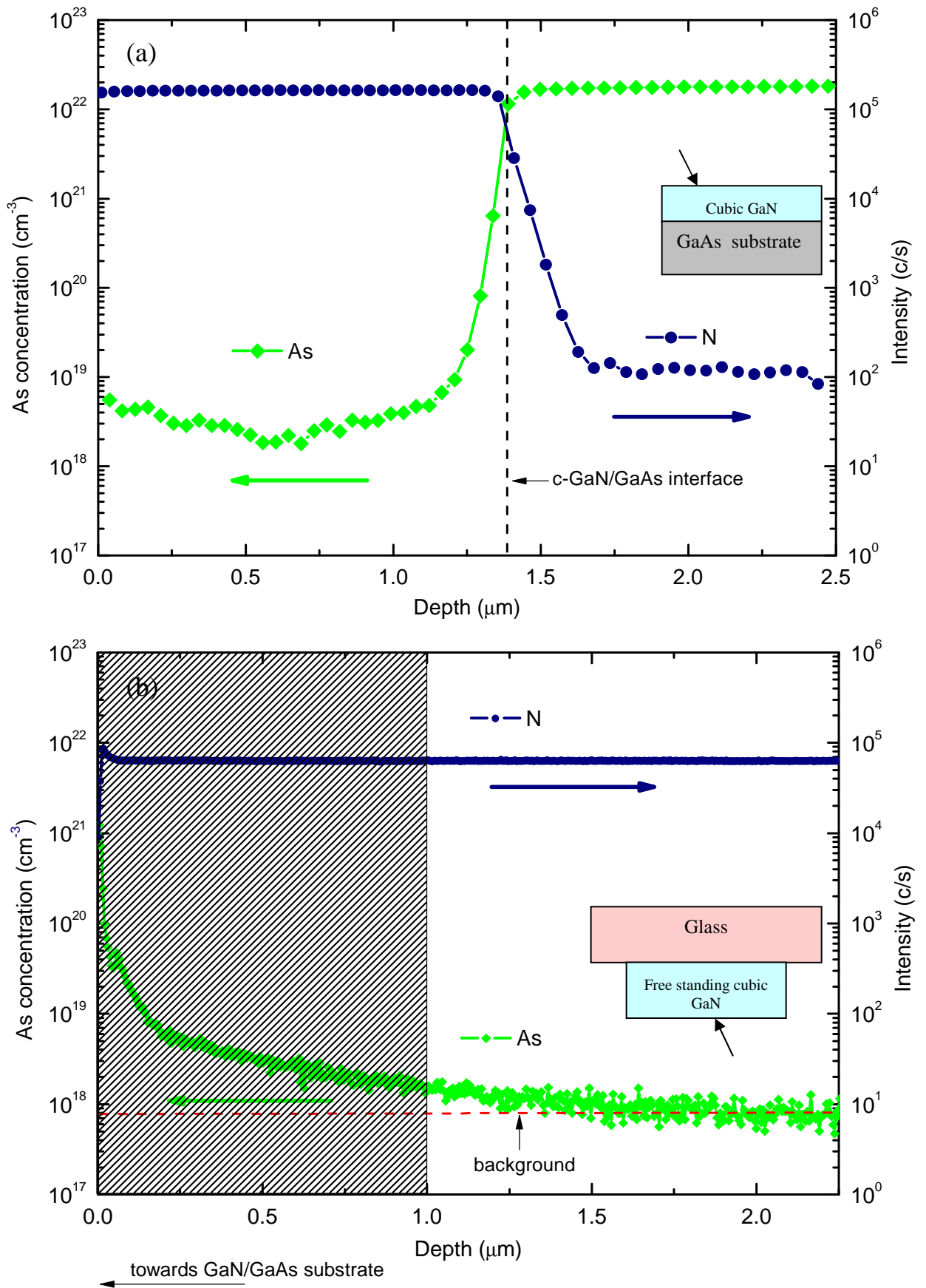


Figure 5.1: SIMS data in cubic GaN samples for different probe directions (a) Thin c-GaN before etching (b) Thick c-GaN after etching. The shaded area needs to be removed by polishing.

From Figure 5.1(a), it is clearly shown that the As density starts to be higher at the interface and towards the GaN/GaAs substrate. The contrary dependence is observed for N density. After the etching, the SIMS measurement is directed to the surface of the thick cubic GaN that was in contact with GaAs substrate and the result is shown in Figure 5.1(b). The N density remains constant, however there is a high quantity of As inclusions at the interface. Therefore, the shaded area indicates a micrometer layer that needs to be removed from the sample by the polishing process in order to reduce the As content to the SIMS background level.

Figure 5.2 shows the XRD data for the free standing $\sim 12\mu\text{m}$ thick cubic GaN layer. The peak in intensity that corresponds to cubic GaN is observed around 40° . Apart from that, a small peak can be seen about 35° . As reported before, this peak could be attributed to hexagonal inclusions or, more probably, to the stacking faults of (111) cubic GaN. In this measurement, the data for the whole depth of the layer had been collected (please refer to Figure 4.6 for comparison). As there is no measurable signal from GaAs observed we can infer that the GaAs substrate was successfully removed from the layer.

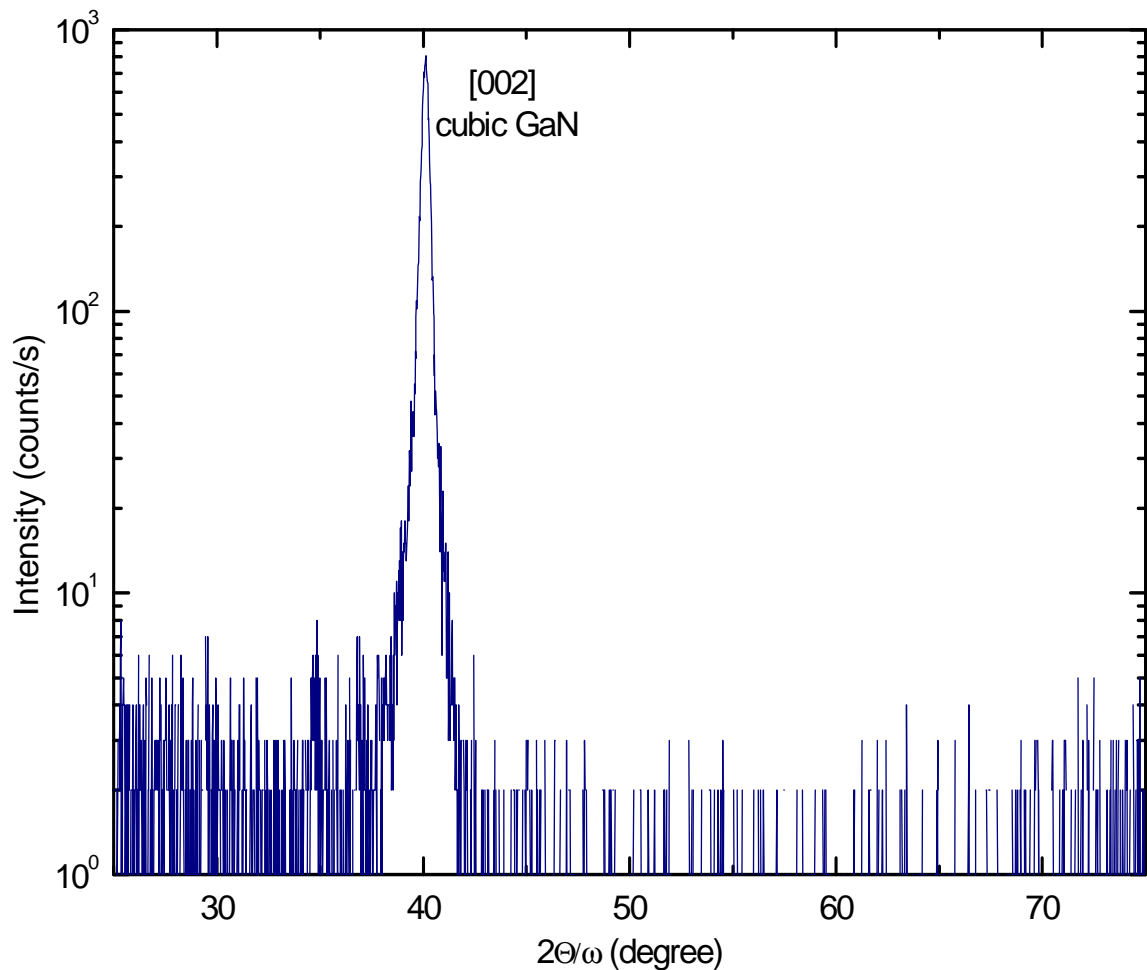


Figure 5.2: XRD data for a free standing thick cubic GaN layer. Clearly, no peak related to GaAs is observed.

5.2: OPTICAL STUDIES FOR CUBIC GaN

In this work, the optical investigation on $\sim 12\mu\text{m}$ thick cubic GaN in contact with the GaAs substrate was carried out⁴. The evidence that this material is mostly cubic had been observed through XRD measurement (*please refer to Figure 4.6*). The sample surface that faces away from the GaN/GaAs interface was polished and excited for optical study. Figure 5.3 shows PL spectra for the sample with the variation of polishing time. Obviously, the hexagonal-related emission gives a strong signal around 3.42eV. This peak could be attributed to free to bound transitions [1]. On the other hand, there is a broad signal with small magnitude around 3.3. We suggest that

⁴ It is risky if we use the free standing sample at this stage as the sample may crack and fall off from the holder during low temperature PL measurement. Note that the wax that holds the sample to the holder is not effective at lower temperature.

this may correspond to the overlapped broad signals between excitonic emissions in cubic GaN and *DA* pair transitions in hexagonal GaN. The inset figure also shows the PL peak as a function of the thickness (note that the polishing rate was about 3 μ m/hour).

It can be seen that the hexagonal PL is significantly reduced after 30 minutes of polishing and continues decreasing at a slower rate on the subsequent times. This is consistent with our previous work, where the percent of the hexagonal content decreases towards the GaN/GaAs interface. However, it should be noted that we intend to polish the surface that was in contact with GaAs substrate, as shown in Figure 5.1(b). If we polish the surface for many hours, we may end up by having the surface with higher hexagonal content (the previous study showed the interface between GaN/GaAs substrate has only few percent of hexagonal material and that this increases towards the GaN surface). Hence, we need to polish the samples for the right amount of time so that the As inclusions and defective material on the surface can be minimised and at the same time the hexagonal content can be minimised. In this work, we polished our cubic GaN substrate for ~2hours.

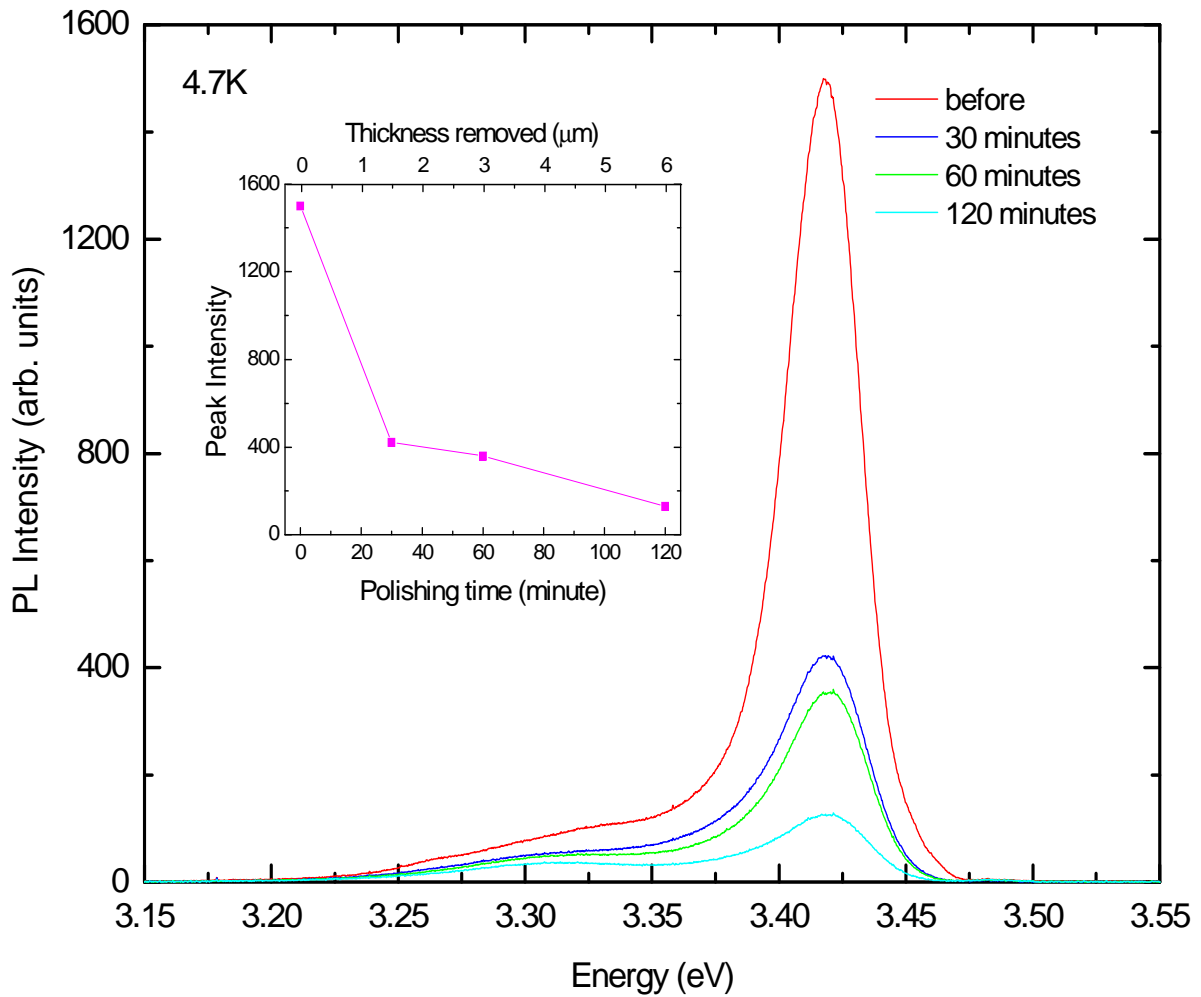


Figure 5.3: PL spectra for polished cubic GaN at different polishing times. Clearly, the hexagonal peak around 3.42eV decreases with time.

5.3: SURFACE MORPHOLOGY STUDIES FOR CUBIC GaN

It has been reported that a rough substrate surface may enhance the formation of stacking faults in cubic GaN [2]. When [111] stacking faults are generated, the growth of hexagonal material could easily occur in the same orientation. For this reason, a smoother surface substrate is required so that the formation of hexagonal material in the subsequent growth on the substrate can be minimised.

In this work, the capability of using the polishing process to reduce the roughness on the nitride surface is examined. As for the first investigation, the top side of a $\sim 12\mu\text{m}$

thick cubic GaN sample mounted on the GaAs substrate was polished⁵ and its surface morphology was measured by AFM for various polishing time. Figure 5.4 shows the value of root mean square (RMS) roughness as a function of removal thickness. Similar to the dependence of hexagonal PL on the thickness, the surface roughness of the sample is considerably reduced when the thickness has been reduced by about $1.5\mu\text{m}$ and continues decreasing at a slower rate for subsequent polishing. This result supports the hypothesis from many reports that there is correlation between the roughness and hexagonal PL [3, 4].

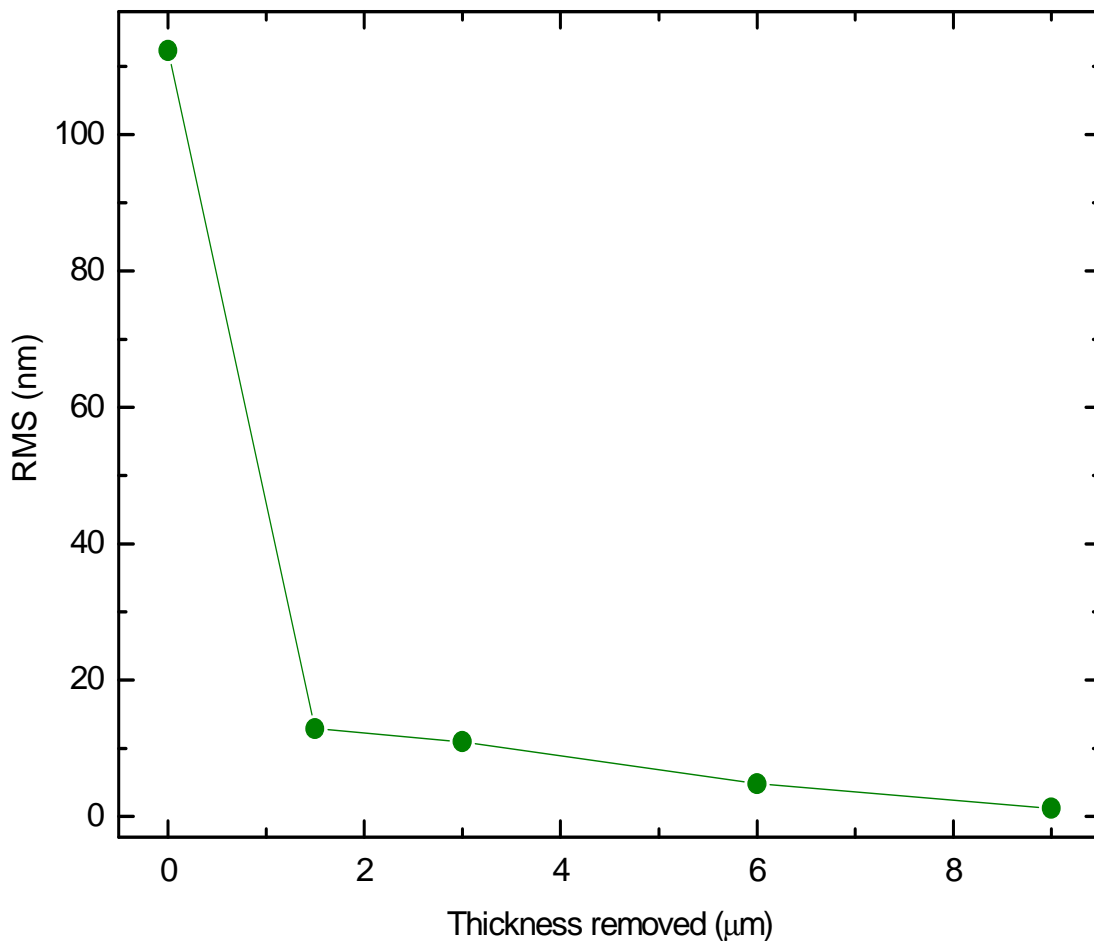


Figure 5.4: Dependence of the value of root mean square (RMS) roughness with the variation of removal thickness.

⁵ It is risky if we use free standing layer as AFM measurement is typically damage/change the surface and potentially crack the sample.

Now, we characterise the surface morphology for a polished free standing $\sim 50\mu\text{m}$ bulk cubic GaN substrate. The polishing time took around 2 hours, correspondingly about $6\mu\text{m}$ layer had been taken off from the sample. It should be noted that the surface that was previously in contact with the GaAs substrate is measured. Figure 5.5(a) shows the AFM image of our cubic substrate while Figure 5.5(b) shows a commercial hexagonal substrate. From the comparison, it is found that the RMS roughness for the polished cubic substrate is lower ($\sim 1.8\text{nm}$) than hexagonal, which is about 2.6nm . This shows the surface quality of our substrate reaches the standard of the commercial one and it could therefore be used as an appropriate substrate for device applications, like LEDs and LDs.

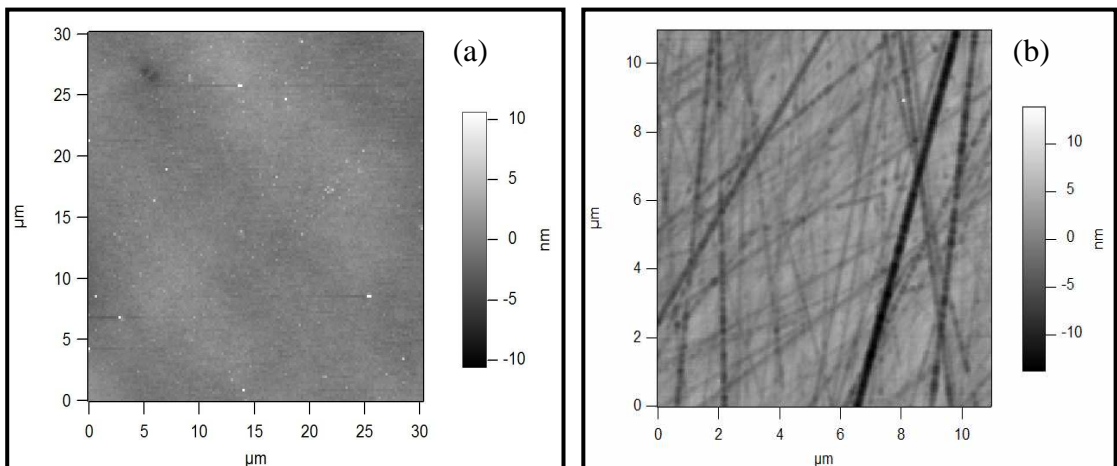


Figure 5.5: AFM images of the surface of (a) polished cubic GaN substrate and (b) commercial hexagonal substrate.

5.4: GROWTH OF DEVICE ON CUBIC GaN SUBSTRATE

To my knowledge, there are no reports which have ever demonstrated the growth of a device on a free standing cubic GaN substrate. In this project, our unpolished and polished free standing cubic GaN substrates were sent to Sharp Laboratories of Europe. In that laboratory, cubic nitride based devices were grown on top of the substrates and the structures were characterised by few measurements.

In this work, a simple LED with 2.5nm cubic $\text{In}_x\text{Ga}_{1-x}\text{N}$ ⁶ active layer was grown on the cubic GaN substrates, respectively. We estimated the In composition in the cubic $\text{In}_x\text{Ga}_{1-x}\text{N}$ layer could be around 10%. The device structure is shown in Figure 5.6.

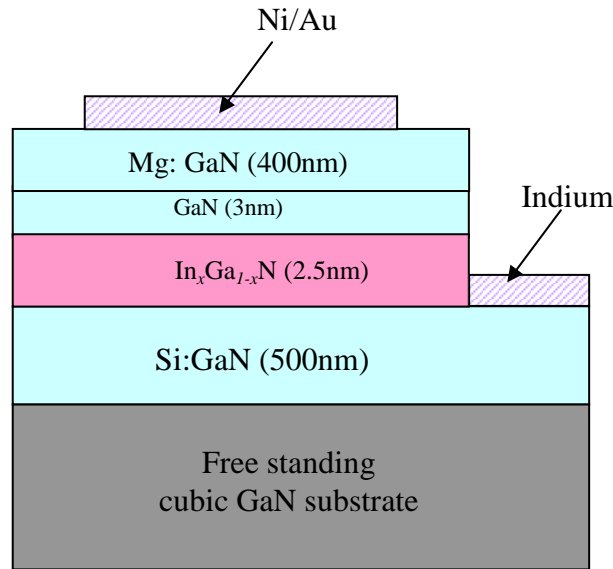


Figure 5.6: Cubic $\text{In}_x\text{Ga}_{1-x}\text{N}$ LED structure grown on unpolished/polished free standing cubic GaN substrates.

Next, the optical properties of the cubic based devices grown on the unpolished and polished free standing cubic GaN were investigated. Figure 5.7 shows PL spectra for the device structure at 15K. An emission peak around 3.2eV is clearly observed in both structures. We suggest that this peak is due to emission from cubic GaN as the penetration depth is about 0.1 μm .

The device grown on the polished substrate gives much brighter PL than that grown on the unpolished substrate. In fact, the peak emission from the polished structure is narrower, indicating that the polished free standing cubic GaN substrate promotes higher material growth quality to the device than the unpolished substrate does.

⁶ The amount of Indium incorporation, x cannot be measured due to too many unknown factors/parameters.

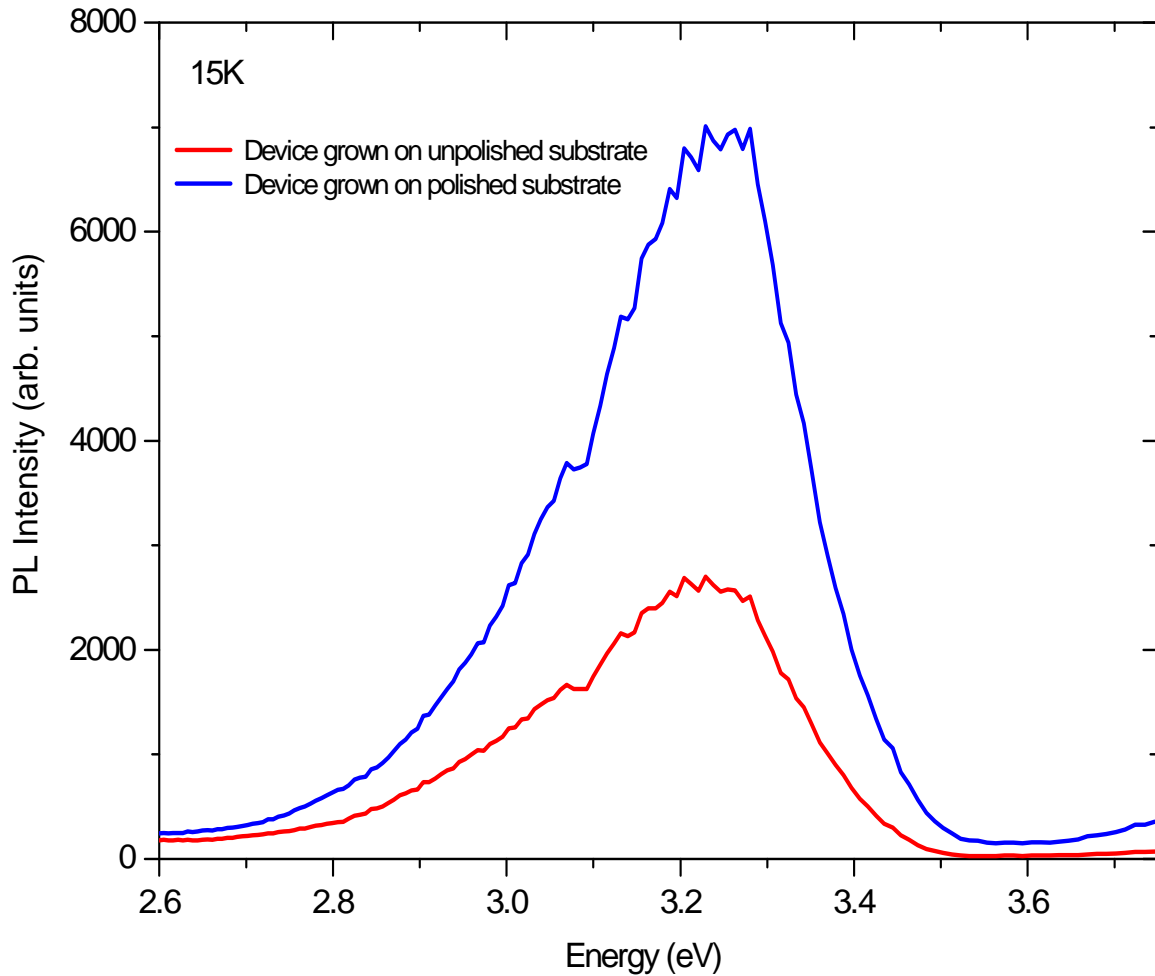


Figure 5.7: PL spectra for $\text{In}_x\text{Ga}_{1-x}\text{N}$ LED structures grown on unpolished and polished free standing cubic GaN substrates.

Subsequently, the current-voltage (I - V) characteristic for the structures was measured. The result is shown in Figure 5.8. Clearly, the device which was grown on the polished substrate shows better performance than that grown on the unpolished substrate. For forward bias, it can be seen that the turn on voltage for the device on the polished substrate is almost comparable to the normal reported value for III-V nitride-based LED [5, 6] in contrast to the device on the unpolished substrate. This might be due to poor doping in the unpolished structure. For reverse bias, there is a high leakage current for the device grown on the unpolished substrate, indicating the possibility of high defect density in the structure [7, 8].

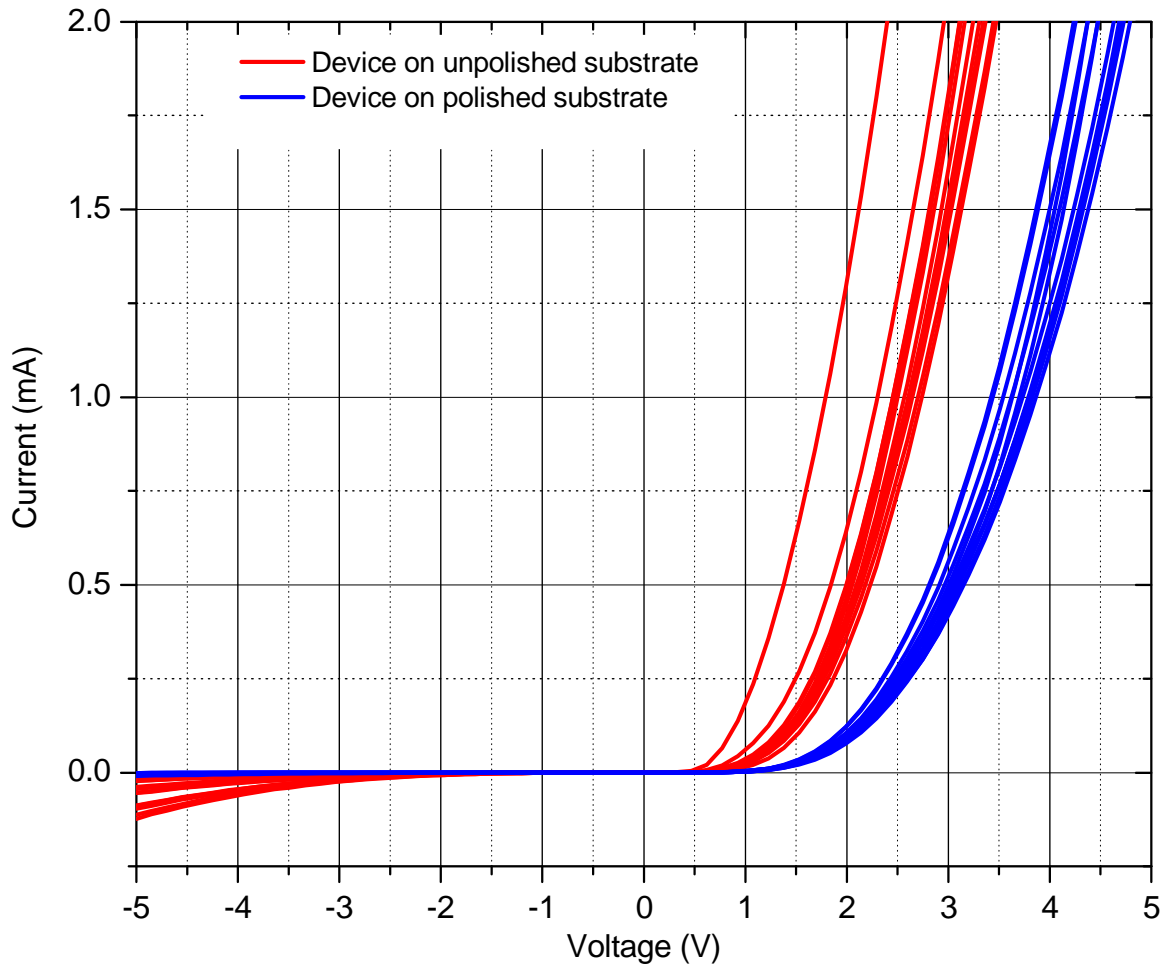


Figure 5.8: Current-voltage characteristics for $\text{In}_x\text{Ga}_{1-x}\text{N}$ LED structures grown on unpolished and polished free standing cubic GaN substrate.

Detailed investigation on electroluminescence (EL) measurements found that increasing the $\text{In}_x\text{Ga}_{1-x}\text{N}$ well width by a factor of 10 improves the LED brightness. Figure 5.9 shows a room EL spectrum for a device with 30nm $\text{In}_x\text{Ga}_{1-x}\text{N}$ well, which was grown on a polished free standing cubic GaN substrate. Obviously, there is a strong peak emission around 460nm that can be attributed to the emission in the cubic $\text{In}_x\text{Ga}_{1-x}\text{N}$ well layer. The emission peak is in excellent agreement with the EL peak that had been observed in InGaN MQWs LED at room temperature [5]. This shows that a working $\text{In}_x\text{Ga}_{1-x}\text{N}$ LED device grown on free-standing cubic GaN substrate has been demonstrated for the first time.

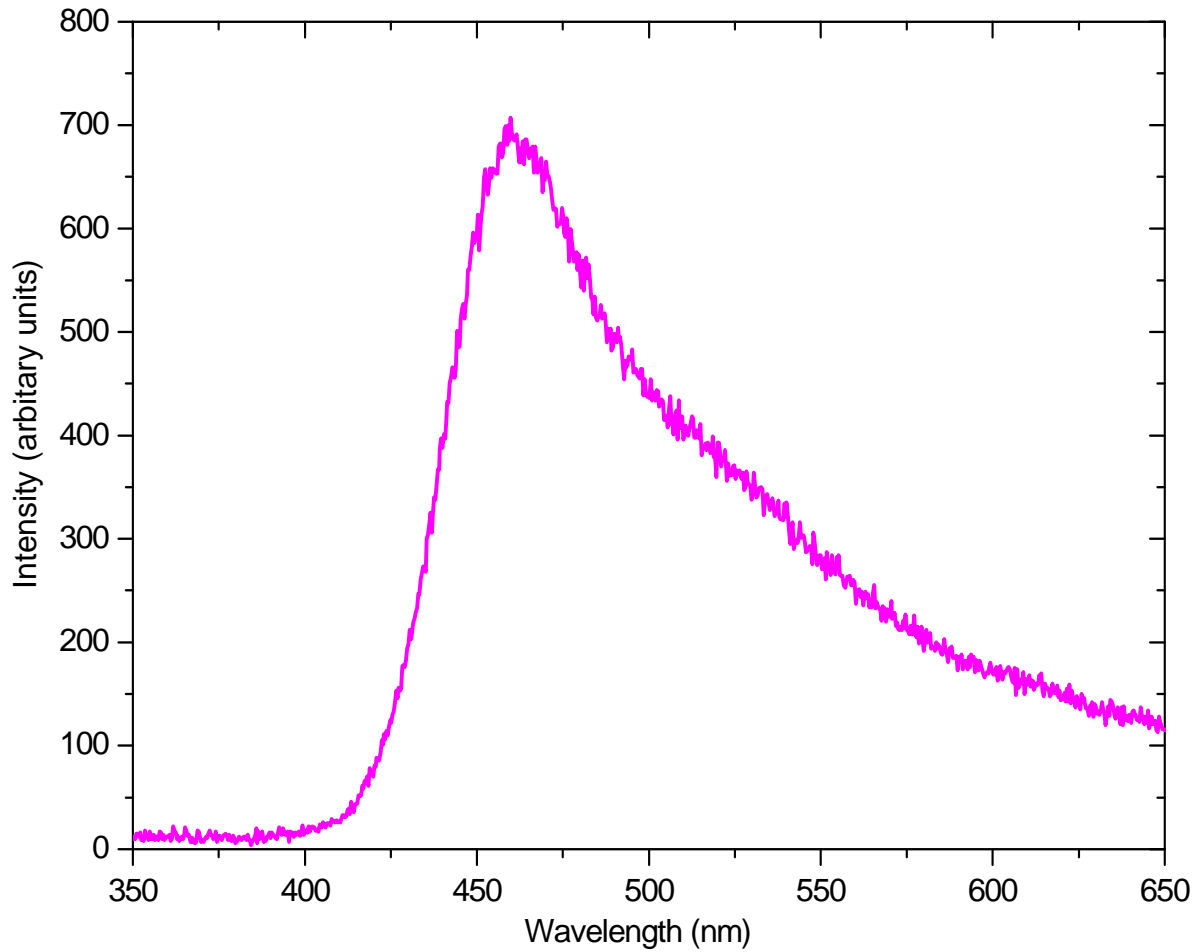


Figure 5.9: EL spectrum for In_xGa_{1-x}N LED grown on polished free standing cubic GaN substrate. The emission wavelength of the In_xGa_{1-x}N LED structure is around 460nm.

5.5: CONCLUSIONS

It has been demonstrated that the polishing process reduces the As inclusions and defective materials on the surface of the cubic GaN layers. We had polished our cubic GaN substrates for 2 hours in order to minimise the As inclusions, defective material and low hexagonal content on the surface. In this work, the first working InGaN LED device grown on a polished free-standing cubic GaN substrate has been demonstrated. Additionally, the polished cubic GaN substrate improves the quality of the grown device as has been measured by luminescence and *I-V* characteristics.

REFERENCES

1. A.V. Andrianov, D.E. Lacklison, J.W. Orton, D.J. Dewsnip, S.E. Hooper, C.T. Foxon, *Semicond. Sci. Technol.*, (1996). **11**: p. 366.
2. C.H. Wei, Z.Y. Xie, L.Y. Li, Q.M. Yu, J.H. Edgar, *J. Electronic Materials*, (2000). **29**: p. 317.
3. H. Tsuchiya, K. Sunaba, T. Suemasu, F. Hasegawa, *J. Cryst. Growth*, (1999). **198/199**: p. 1056.
4. B. Daudin, G. Feuillet, J. Hubner, Y. Samson, F. Widmann, A. Philippe, C. Bru-Chevallier, G. Guillot, E. Bustarret, G. Bentoumi, A. Deneuveille, *J. Appl. Phys.*, (1998). **84**: p. 2295.
5. C. Mo, W. Fang, Y. Pu, H. Liu, F. Jiang, *J. Cryst. Growth*, (2005). **285**(312).
6. A. Dadgar, M. Poschenrieder, J. Blaßing, K. Fehse, A. Diez, A. Krost, *Appl. Phys. Lett.*, (2002). **80**: p. 3670.
7. X.A Cao, J.A. Teetsov, F. Shahedipour-Sandvik, S.D Arthur, *J. Cryst. Growth*, (2004). **264**(172).
8. P. Kozodoy, J.P. Ibbetson, H. Marchand, P. T. Fini, S. Keller, J. S. Speck, S. P. DenBaars, U. K. Mishra, *Appl. Phys. Lett.*, (1998). **73**: p. 975.

CHAPTER 6: CUBIC NITRIDES BASED RESONANT TUNNELLING DIODE

As has been mentioned in the earlier part of this thesis, the absence of internal piezoelectric fields makes cubic GaN interesting for vertical transport devices. Without the existence of such fields, problems with charge trapping that contributes to the irreproducibility of the current-voltage (I - V) result does not exist. Moreover, the theoretical modelling of tunnel devices would be made much simpler. On the other hand, due to the difficulty of growing cubic nitrides, there have been no studies on cubic nitride based resonant tunnelling structures reported so far. Considerable progress in cubic GaN and AlGaN growth has been demonstrated in this project and therefore we intend to transfer this technology to develop a working cubic nitride based tunnel diode for the first time.

At the beginning of this chapter, a brief introduction to basic principles of operation of double barrier resonant tunnelling diodes (DBRTDs) is presented. As published data on cubic nitride tunnel diodes are not available at present, reports on the hexagonal (wurtzite) $\text{Al}_x\text{Ga}_{1-x}\text{N}/\text{GaN}$ DBRTDs are reviewed pointing out the problems caused by the internal fields, threading dislocations etc and therefore the vertical transport properties in cubic device may be anticipated. Next, the theoretical analysis of the tunnelling process in cubic $\text{Al}_x\text{Ga}_{1-x}\text{N}/\text{GaN}$ resonant tunnelling structures will be discussed. From this understanding, detailed calculations of tunnelling current-voltage (I - V) characteristics of a cubic based tunnel diode with the variation of band offset, well width, barrier composition, and barrier thickness will be presented. Through this calculation work, an optimal design of cubic $\text{Al}_x\text{Ga}_{1-x}\text{N}$ DBRTD is proposed, promising the feasibility of fabricating and characterising the tunnel device. Based on the designed structure, we will demonstrate for the first time, a working cubic $\text{Al}_x\text{Ga}_{1-x}\text{N}/\text{GaN}$ DBRTD.

6.1: TUNNELLING PROCESS IN DEVICE STRUCTURE

In the classical regime, only an electron that has sufficient kinetic energy will pass over a potential barrier, while electrons with lower energy will be reflected back. On the other hand, quantum mechanics allows a finite probability for electrons with lower energy than the barrier height to tunnel through the barrier. This fundamental concept is significantly observed in the *resonant tunnelling diode* (RTD) structure. An RTD is basically a quantum well sandwiched between two tunnel barriers with doped contacts on either side to form Fermi seas of electrons, as is shown in Figure 6.1(a). The red arrows show the width of the resonant level, Γ in the well and the barriers and well widths are d_b and d_w , respectively. When a low voltage bias is applied to the device a small current flows. The current comes from various mechanisms such as non-resonant tunnelling, thermionic emission over the barriers, scattering assisted tunnelling process and leakage current through the surface states all of which contribute to the background current. Increasing the bias voltage (Figure 6.1(b)) raises the emitter relative to the resonant level in the well and gives a maximum current when the conduction band in the emitter region corresponds to the resonant level. At this stage, more electrons are injected from the emitter region to the quantum well and therefore a peak current in the current-voltage (I - V) characteristic is obtained. Further increasing the voltage (Figure 6.1(c)) brings the resonant level below the emitter level and therefore reduces the current. This process produces a *negative differential resistance* (NDR) property in the I - V characteristic as shown in Figure 6.1(d). The current will rise up again due to the background effects and when the second resonant level (not shown in the figure) approaches the emitter level.

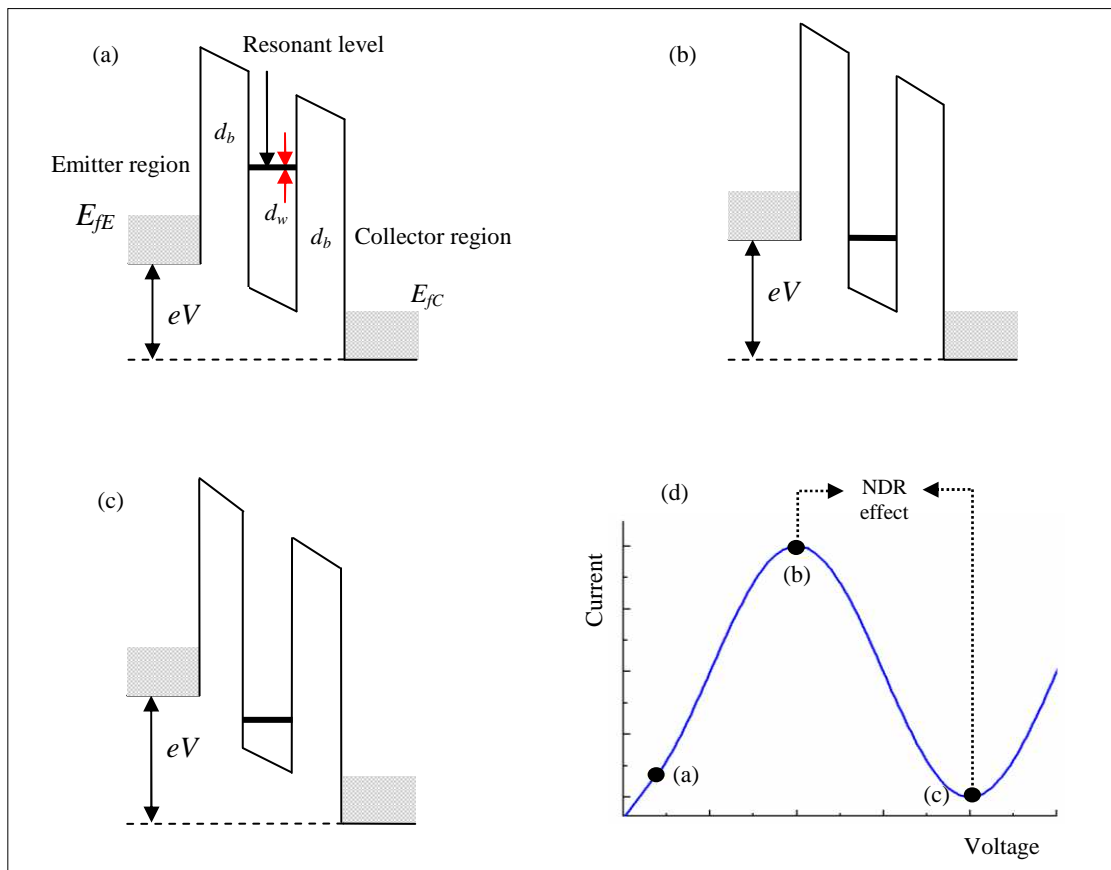


Figure 6.1: (a)-(c) illustrate the changes of the band structure with the variation of applied voltage, V . The width of resonant level, Γ is indicated by the red arrows. (d) shows the dependence of current on applied voltage, V .

Due to their NDR characteristics, RTDs are useful for high-speed switching, high frequency oscillators, multi level logic and other applications. Moreover, their structure is quite simple thus making them easy to fabricate. In most cases, the quality of an RTD is typically described by the ratio of currents at the peak and valley (PVR). In the following section, a survey of published results on hexagonal AlN/GaN DBRTDs (double barrier resonant tunnelling diodes) is presented. From the survey, we can speculate the tunnelling properties in cubic nitride based DBRTDs structures.

6.2: STUDIES OF WURTZITE NITRIDES TUNNELLING DIODES

In 2001, Kikuchi et al reported the tunneling properties of two types of MBE grown RTD structures; double barrier and superlattice barrier type AlN/GaN RTDs [1]. The DBRTD had a 0.75nm GaN quantum well with 1nm AlN barriers, while the superlattice RTD consisted of six 1nm AlN barriers with five 1nm GaN quantum wells. At room temperature, the double barrier structure showed evidence of the NDR effect at 2.4V with peak current density and PVR values of 930mA/cm² and 3.1, respectively. In the superlattice barrier AlN/GaN RTD structure, the NDR effect was observed at 1.6V with the peak current density around 142A/cm² and the peak-to-valley ratio (PVR) was three times higher than that of the DBRTD. A year later, the same group published a controversial result, where the PVR value of a high quality AlN/GaN RTD structure was found to be 32 with a NDR voltage of 2.4V and a peak current density of 180A/cm² [2]. This PVR value seems unrealistic as high background defect density is readily expected in III-nitrides system. In fact, the authors did not report the reproducibility of the result on the same device, which suggests that the NDR feature might also be due to current instability or breakdown of the device. Moreover, they only demonstrated the *I-V* measurement on the positive bias (started from 0V), which might hide the evidence of the hysteresis at negative bias.

The group of Belyaev et al [3-6] found that the appearance of the NDR effect in *I-V* characteristics for MBE AlN/GaN RTD was dependent on the direction of voltage sweep. The NDR peak and voltage changed for consecutive sweeps. The hysteresis was also observed in *C-V* measurements. From these observations, they suggested that the non-reproducible result arises from the polarization effect and the existence of defects in the device that lead to charge trapping. In low temperature measurements, the NDR effect was clearly observed around 0.8V with peak current nearly 0.044μA with an increasing voltage sweep but the feature was not seen for the reverse bias direction [5]. Nonetheless, the authors suggested that the NDR feature was associated with current instabilities due to the problem with the charge trapping instead of true tunneling process.

Realizing defects could influence the performance of nitride based RTDs, Bayram et al [7] had grown some AlN/GaN DBRTD structures by MOCVD with different dislocation densities. Unsurprisingly, they reported that the device performance decreased in devices with higher defect density. Their best device exhibited room temperature NDR effect at 4.7V with a peak current density of 59kA/cm^2 and a PVR value of 1.6. This PVR value however, was still lower than the best MBE tunnel structures, which suggests that MBE is the most suitable growth method for producing high quality nitride based RTDs. Although the device was grown with low defect density, the result was not reproducible in the subsequent measurements due to charge trapping and strong hysteresis, which might be enhanced by strong polarization fields.

Even though the nitride based RTD devices were fabricated by different methods in different experiments, it seems that the NDR effect of the tunnel devices only occurs once, during the first bias scan. This is attributed to charge trapping effects which may be related to the large polarization effect in hexagonal III-V nitrides. Reproducing the result is challenging and therefore there have been a number of attempts to address this issue. Since the charge trapping is found to be more significant at high reverse bias, Belyaev et al. proposed that the carriers could be released from the traps by applying a large forward bias [5, 6]. On the other hand, Golka et al. demonstrated that the NDR peak can be partially recovered by annealing the sample at 350°C [8]. In another report, this group managed to restore the NDR effect by applying at least -3V to the device when sweeping from negative to positive bias [9]. However, the effect disappeared when the device was swept in opposite direction, (from positive to negative bias).

Based on this survey, it is clear that the NDR effect in wurtzite nitride based resonant tunnel diodes is irreproducible. Most of the authors suggested that this problem may be associated with the charge trapping phenomenon. While the material quality remains an issue, the main reason for the charge trapping phenomenon is because of strong polarization effects in wurtzite structures grown on the *c*-axis. These effects could also lead to highly asymmetric *I-V* characteristic and complicate the modelling and design of the devices. By contrast, growing the tunnelling device on non-polar (001) cubic $\text{Al}_x\text{Ga}_{1-x}\text{N}/\text{GaN}$ is an approach which eliminates such internal fields. As

a result, the calculation of tunnelling is more straight-forward and the tunnelling properties in the device would be more reproducible. Nevertheless, due to the huge challenge of growing cubic nitride materials, no studies have yet demonstrated cubic $\text{Al}_x\text{Ga}_{1-x}\text{N}/\text{GaN}$ based RTD.

Despite this issue, in this project, we have demonstrated impressive progress in the growth of cubic GaN. Using this technology, it is expected that the growth of a high quality cubic $\text{Al}_x\text{Ga}_{1-x}\text{N}/\text{GaN}$ ($x < 0.2$) tunnelling structure is possible and therefore will be demonstrated. Before the growth, it is practical to find an optimal design of cubic $\text{Al}_x\text{Ga}_{1-x}\text{N}/\text{GaN}$ DBRTD that can then be fabricated and tested. In this work, the I - V characteristics of cubic $\text{Al}_x\text{Ga}_{1-x}\text{N}/\text{GaN}$ DBRTD have been calculated with the variation of band offset, well-width, barrier composition and barrier thickness parameters. In the following section, the theoretical calculation on the vertical transport properties in the cubic nitrides structure is presented.

6.3: MODELLING OF CUBIC NITRIDE TUNNELLING DEVICE

At the first stage of this work, the confined state energy level, E_{pk} (*resonant level*) in the quantum well was found by solving the Schrödinger equation, using the effective mass approximation (EMA) and taking into account the different masses in the well and barrier regions. In our calculation, the effect of non-parabolicity and strain on the EMA are neglected. These effects had been experimentally observed for the case of hexagonal $\text{Al}_x\text{Ga}_{1-x}\text{N}/\text{GaN}$ heterostructures, however the effects are found to be less significant in lower quality materials [10, 11]. It is generally accepted that the quality of cubic nitrides is lower than typical hexagonal structures [12] and therefore, if the magnitudes are assumed similar in cubic GaN, then the effects should be even less. The calculated value of E_{pk} is adopted in the calculation of the tunnelling I - V characteristic using the Tsu-Esaki model [13]. This model describes the electrical transport properties of a finite superlattice from the tunnelling point of view.

6.3.1: Theoretical Calculation of Resonant Level in Quantum Well

Consider a finite depth double barrier structure as shown in Figure 6.2. An electron with an energy E , lower than a potential depth V_0 , is confined inside the well. The wave function of the electron, $\psi(z)$ inside the well is defined in a similar manner to the case for infinite depth as shown below.

$$\psi(z) = C \begin{cases} \cos \\ \sin \end{cases} (kz) \quad \left. \begin{array}{l} \text{even} \\ \text{odd} \end{array} \right\} \text{function.} \quad (6.1)$$

Here, the lowest (first) bound state in the well is an even function (*cosine function*) and k is the wave number inside the well.

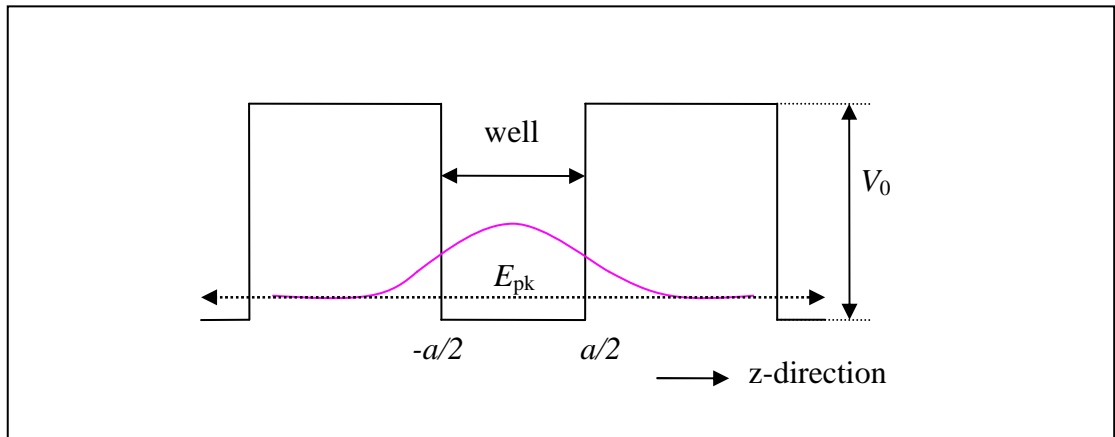


Figure 6.2: Schematic diagram of the wave function of electron at the first bound state energy, E_{pk} in the quantum well with finite barrier layers at the conduction band. The well width and potential depth are given as a and V_0 , respectively.

The wave function outside the well is given by the Schrödinger equation,

$$-\frac{\hbar^2}{2m_b} \frac{d^2}{dz^2} \psi(z) + (V_0 - E)\psi(z) = 0, \quad (6.2)$$

where m_b is the effective mass for the barrier layers and $E < V_0$. Solving the Schrödinger equation above gives

$$\psi(z) = D \exp(\pm \kappa z), \quad (6.3)$$

where κ is the imaginary part of the wave number. The sign of κ is chosen so that the argument of the exponential is always negative.

As shown in Figure 6.2, the wave functions inside and outside the well, $\psi(z)$ have to be matched at the boundaries; $z = a/2$ and $z = -a/2$. Using equation (6.1) and (6.3), the matching condition at $z = \frac{1}{2}a$ gives

$$\psi\left(\frac{a}{2}\right) = C \begin{Bmatrix} \cos \\ \sin \end{Bmatrix} \left(\frac{ka}{2}\right) = D \exp\left(\frac{\kappa a}{2}\right). \quad (6.4)$$

Equally, taking the derivative of equation (6.4) yields

$$\left. \frac{d\psi}{dz} \right|_{z=a/2} = Ck \begin{Bmatrix} -\sin \\ \cos \end{Bmatrix} \left(\frac{ka}{2}\right) = -D\kappa \exp\left(\frac{\kappa a}{2}\right). \quad (6.5)$$

However, equation (6.5) does not conserve current if the heterostructure has two different effective masses. Therefore, the matching boundary condition in this equation needs to be modified. For this case, the matching of derivative in equation (6.5) becomes

$$\frac{1}{m_w} \left. \frac{d\psi}{dz} \right|_{z=a/2} = \frac{1}{m_b} \left. \frac{d\psi}{dz} \right|_{z=a/2}. \quad (6.6)$$

This change also modifies the wave numbers. The wave numbers inside the well, k and outside the well, κ are then given by:

$$k = \frac{\sqrt{2m_0 m_w (E - E_c^w)}}{\hbar}, \quad \kappa = \frac{\sqrt{2m_0 m_b (E_c^b - E)}}{\hbar} \quad (6.7)$$

with m_w and E_c^w are the effective mass and the bottom of conduction band inside the well, respectively. Similarly, m_b and E_c^b are the corresponding parameters outside the well. Here, the depth of the well, V_0 is found to be $E_c^b - E_c^w = \Delta E_c$.

The boundary condition in equation (6.6) gives

$$\frac{Ck}{m_w} \begin{Bmatrix} -\sin \\ \cos \end{Bmatrix} \left(\frac{ka}{2} \right) = -\frac{D\kappa}{m_b} \exp \left(\frac{\kappa a}{2} \right). \quad (6.8)$$

Equation (6.8) is then divided by equation (6.4) at $\psi(a/2)$ to give

$$\sqrt{\frac{m_w}{m_b} \left(\frac{2m_0 m_w V_0}{\hbar^2 k^2} - 1 \right)} - \begin{Bmatrix} \tan \\ -\cot \end{Bmatrix} \left(\frac{ka}{2} \right) = 0. \quad (6.9)$$

Using k from equation (6.7), the matching condition can also be written as

$$\left(\sqrt{\frac{m_w}{m_b} \left(\frac{V_0}{(E - E_c^w)} - 1 \right)} \right) - \begin{Bmatrix} \tan \\ -\cot \end{Bmatrix} \left(\sqrt{\frac{a^2 m_0 m_w (E - E_c^w)}{2\hbar^2}} \right) = 0. \quad (6.10)$$

In this work, we find the value of energy, E that satisfies equation (6.10). This energy is equal to E_{pk} . Once this energy is obtained, the values of k and κ can be found through equation (6.7). These values are then used in equations (6.1) and (6.3) to plot the wavefunction $\psi(z)$, throughout the double barrier structure. For simplicity of the calculation, only the first (lowest) bound state energy will be calculated in this work.

Figure 6.3 shows an example of the calculated probability of electron density distribution, $|\psi|^2(z)$ in a cubic $\text{Al}_{0.1}\text{Ga}_{0.9}\text{N}/\text{GaN}$ double barrier heterostructure with the energy, E_{pk} approximately 0.16eV. If the energy in the emitter region corresponds to this energy, the probability for an electron to tunnel the barrier will reach a maximum, thus giving a maximum current in the I - V characteristic.

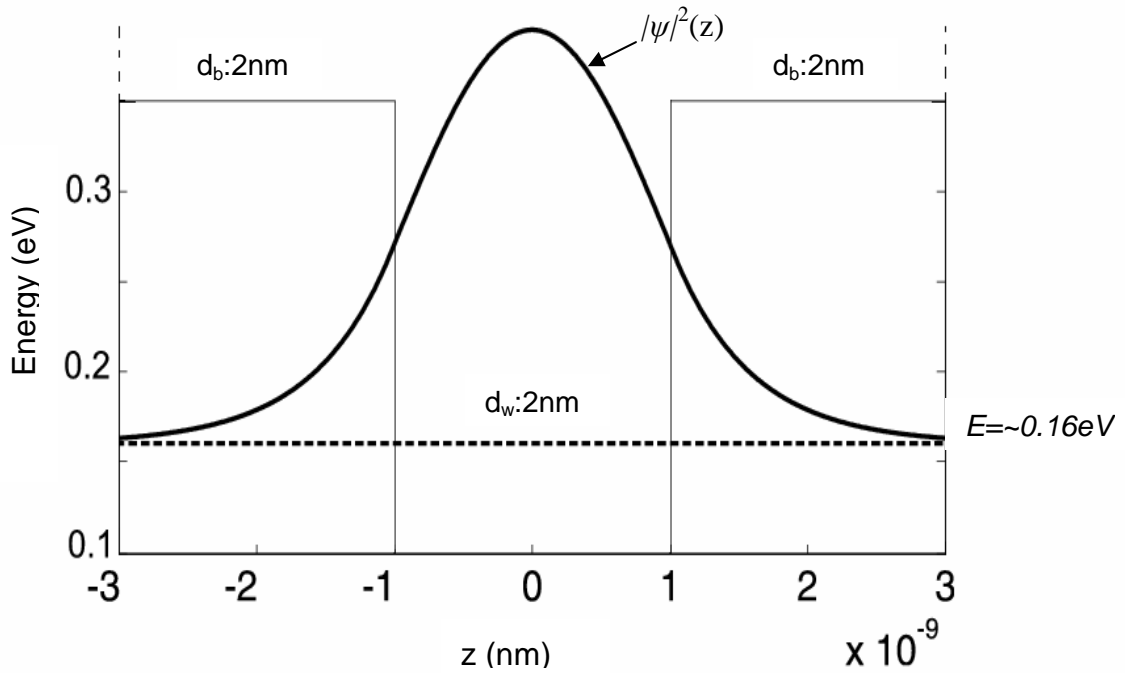


Figure 6.3: The calculated distribution of electron wave function at the first energy bound state in $\text{Al}_{0.1}\text{Ga}_{0.9}\text{N}/\text{GaN}$ double barriers structure.

It should be noted that the probability of the tunnelling event is always described by the transmission coefficient as a function of energy, $T(E)$. Therefore, $T(E)$ is strongly influences the tunnelling properties of the RTD. In the following section, the calculation of $T(E)$ is presented.

6.3.2: Theoretical Calculation of Transmission Coefficient

Consider an electron tunnelling through a single finite barrier with a potential, V_0 and the barrier width of a , as shown in Figure 6.4. The wave function, $\psi(z)$ changes as the electron moves from region 1 to 3. This shows that the wave number, k is also changing between different regions.

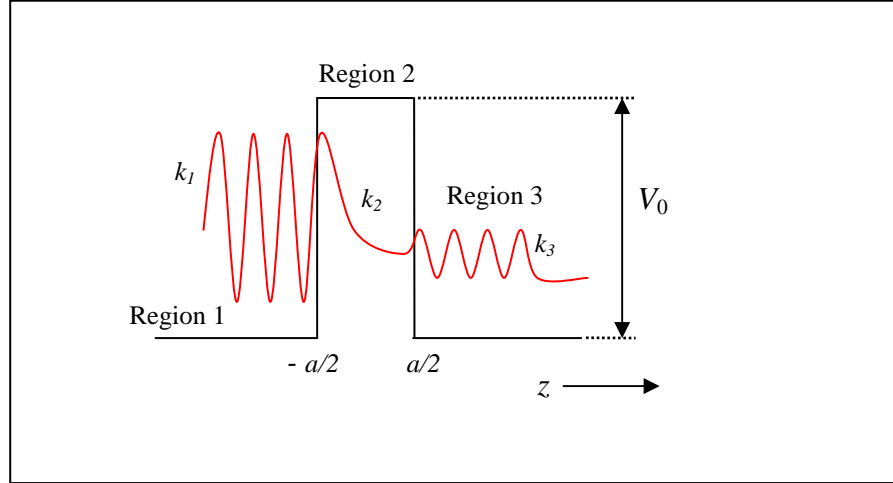


Figure 6.4: A schematic diagram of the tunnelling of electron through a single barrier. The wave function of the electron changes as it moves towards different regions.

The potential in regions 1 and 3 is zero. So, $k_1 = k_3$. Using a transfer matrix technique (see [14] for more details), the transmission amplitude, t^7 is given by

$$t = \frac{2k_1 k_2 e^{-ik_1 a}}{2k_1 k_2 \cos k_2 a - i(k_1^2 + k_2^2) \sin k_2 a} \quad (6.12)$$

When $E > V_0$, the individual transmission coefficient $T = |t|^2$ is expressed as

$$T = \frac{4k_1^2 k_2^2}{4k_1^2 k_2^2 + (k_1^2 + k_2^2)^2 \sin^2 k_2 a} = \left[1 + \frac{V_0^2}{4E(E - V_0)} \sin^2 k_2 a \right]^{-1}, \quad (6.13)$$

where $k_2 = [2m(E - V_0)/\hbar^2]^{1/2}$ and the reflection coefficient, $R = 1 - T$.

In the case of $E < V_0$, the usual replacement $k_2 \rightarrow i\kappa_2$ is made. Therefore, $\sin k_2 a = \sin i\kappa_2 a = i \sinh \kappa_2 a$ and transmission coefficient or transmission probability becomes

⁷ It is the ratio of the amplitudes of transmitted and incident waves.

$$T = \frac{4k_1^2 \kappa_2^2}{4k_1^2 \kappa_2^2 + (k_1^2 + \kappa_2^2)^2 \sinh^2 \kappa_2 a} = \left[1 + \frac{V_0^2}{4E(V_0 - E)} \sinh^2 \kappa_2 a \right]^{-1}. \quad (6.14)$$

If the energy is equivalent to the top of the barrier, $E=V_0$, the transmission becomes

$$T(E = V_0) = \left[1 + \frac{ma^2 V_0}{2\hbar^2} \right]^{-1}. \quad (6.15)$$

For the simplicity of the calculation, this work focuses only on the case for $E < V_0$. Hence, equation (6.14) is used in further calculation.

Consider an electron travelling through finite barriers of thickness a in a double barrier structure. When the electron is trapped in the well, it tries to escape to the left and the right sides. For a convenient understanding, the transmission probability to the left is given by T_L and to the right is T_R . Assuming the structure is symmetric, the transmission amplitudes for both directions are identical.

The velocity of the electron in the resonant state in the well is given by v and the distance of a round trip is $2a$. Thus, the electron tries to escape by hitting the left barrier $v/2a$ times per second. The probability of electron transmission through the left barrier is T_L per event, giving the average escape rate at $vT_L/2a$. The same thing also happens at the right barrier, hence giving the total average escape rate, $v(T_L+T_R)/2a$. This equation is multiplied by \hbar to convert the expression into energy. Thus, the full width at half maximum (FWHM), Γ of the resonant peak is given by

$$\Gamma = \frac{\hbar v}{2a} (T_L + T_R) \quad (6.16)$$

Clearly, Γ decreases as a , is increased. From a more detailed mathematical analysis see [14]. The transmission coefficient as a function of energy can be approximated by

$$T(E) \approx T_{pk} \left[1 + \left(\frac{E - E_{pk}}{\frac{1}{2}\Gamma} \right)^2 \right]^{-1}, \quad (6.17)$$

where T_{pk} reaches unity at the resonant state in the well.

6.3.3: Theoretical Calculation of Tunnelling Current in DBRTD

In this work, the tunnelling current-voltage (I - V) characteristic of $\text{Al}_x\text{Ga}_{1-x}\text{N}/\text{GaN}$ DBRTD is calculated numerically using Tsu-Esaki model, which was originally developed to describe the mechanism of tunnelling transport in a finite superlattice structure in the $\text{Al}_x\text{Ga}_{1-x}\text{As}/\text{GaAs}$ system. The tunnelling current density in the tunnelling structure is given by

$$J_{RT} = \frac{qm_e^* k_b T}{2\pi^2 \hbar^3} \int_{E_c}^{\infty} dE \left[T(E) \ln \left(\frac{1 + \exp(E_{fE} - E) / k_b T}{1 + \exp(E_{fC} - E) / k_b T} \right) \right], \quad (6.18)$$

where E_{fE} and E_{fC} are the Fermi levels in the emitter and collector regions, respectively (please refer to Figure 6.1). In this case, E_{fC} is equal to $E_{fE} - eV$ (V is the applied voltage). The integral equation describes the density of electron distribution as a function of E . Using the dependence of quasi Fermi level on electron concentration, E_{fE} is estimated at around 0.09eV.

Equation (6.18) indicates that the tunnelling current, J_{RT} has strong $T(E)$ dependence. From equation (6.17), it is found that the transmission through $\text{Al}_x\text{Ga}_{1-x}\text{N}$ barriers depends on their thickness, d_b and height (which is determined by the aluminium fraction, x). The larger is $T(E)$, the higher is the peak current density. However, the lifetime in the well decreases and from the uncertainty principle, the width, Γ of the resonant level in the quantum well increases, resulting in a broader resonant peak. On the other hand, if the barrier width/height of the tunnelling structure is designed to be larger, the resonant peak becomes narrower but the peak current is lower. These considerations show that designing an optimal performance of tunnelling device needs to achieve a compromise between peak current and

resonant width, which will be addressed in the later section. Details of the method of calculation used in this work are presented in Appendix I.

6.4: MODELLING OF CUBIC $\text{Al}_x\text{Ga}_{1-x}\text{N}/\text{GaN}$ DBRTD

In this work, the tunnelling I - V characteristics in $\text{Al}_x\text{Ga}_{1-x}\text{N}/\text{GaN}$ double barrier resonant tunnelling diode (DBRTD) have been calculated as a function of variation of band offset, well width, barrier composition, and barrier thickness. At the end of this calculation, an optimal design of cubic $\text{Al}_x\text{Ga}_{1-x}\text{N}/\text{GaN}$ DBRTD is suggested, promising the feasibility of fabricating and characterising the tunnel device.

Figure 6.5 shows a cubic $\text{Al}_x\text{Ga}_{1-x}\text{N}/\text{GaN}$ DBRTD designed structure with undoped c-GaN well width of d_w , sandwiched between undoped $\text{Al}_x\text{Ga}_{1-x}\text{N}$ barrier widths of d_b . This structure is clad by thicker n-doped cubic GaN layers for emitter and collector contacts.

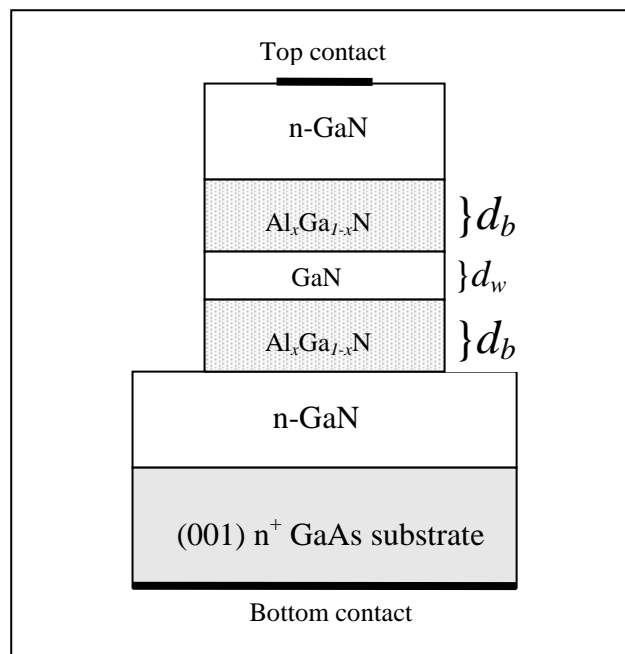


Figure 6.5: A schematic of cubic $\text{Al}_x\text{Ga}_{1-x}\text{N}/\text{GaN}$ tunnel diode.

In this calculation, the material parameters for cubic GaN at 300K are assumed as follows; electron effective mass, $m^* = 0.15m_0$ [15] and energy gap, $E_g = 3.2\text{eV}$ [16]. For cubic AlN, $m^* = 0.25m_0$ [17] and energy gap, $E_g = 5.94\text{eV}$ [18]. It has been reported that cubic AlN has an indirect band gap around 5.34eV at X-valley [19]. However, the resonant tunnelling process is significant in direct gap semiconductor, while non-resonant tunnelling via indirect gap gives background [20]. These parameter values vary slightly at 77K; however, the changes do not impinge the occurrence of the tunnelling. The band gap for cubic $\text{Al}_x\text{Ga}_{1-x}\text{N}$ were estimated using Vegard's Law, (assuming negligible bowing parameter) and their effective mass was determined using linear interpolation between the AlN and GaN values. For the ease of the calculation, only tunnelling through the first (lowest) resonant level in the quantum well is considered.

6.4.1: Numerical Calculation of Resonant Energy in DBRTD structure

Figure 6.6 shows the probability electron density distribution, $|\psi(z)|^2$ in cubic $\text{Al}_x\text{Ga}_{1-x}\text{N}/\text{GaN}$ double barriers structure with different Al fraction, which determines their barrier height. The well and barrier widths are given as 1nm and 2nm, respectively. As the barrier height is increased, the electron state in well is more confined and so, the width of the resonant level, Γ is smaller. Consequently, the coupling of the electrons to the plane wave decreases, and therefore reduces the probability of electron to tunnel through the barrier layers. On the other hand, lower barrier height increases the electron coupling and broadens the Γ but increases the tunnelling probability.

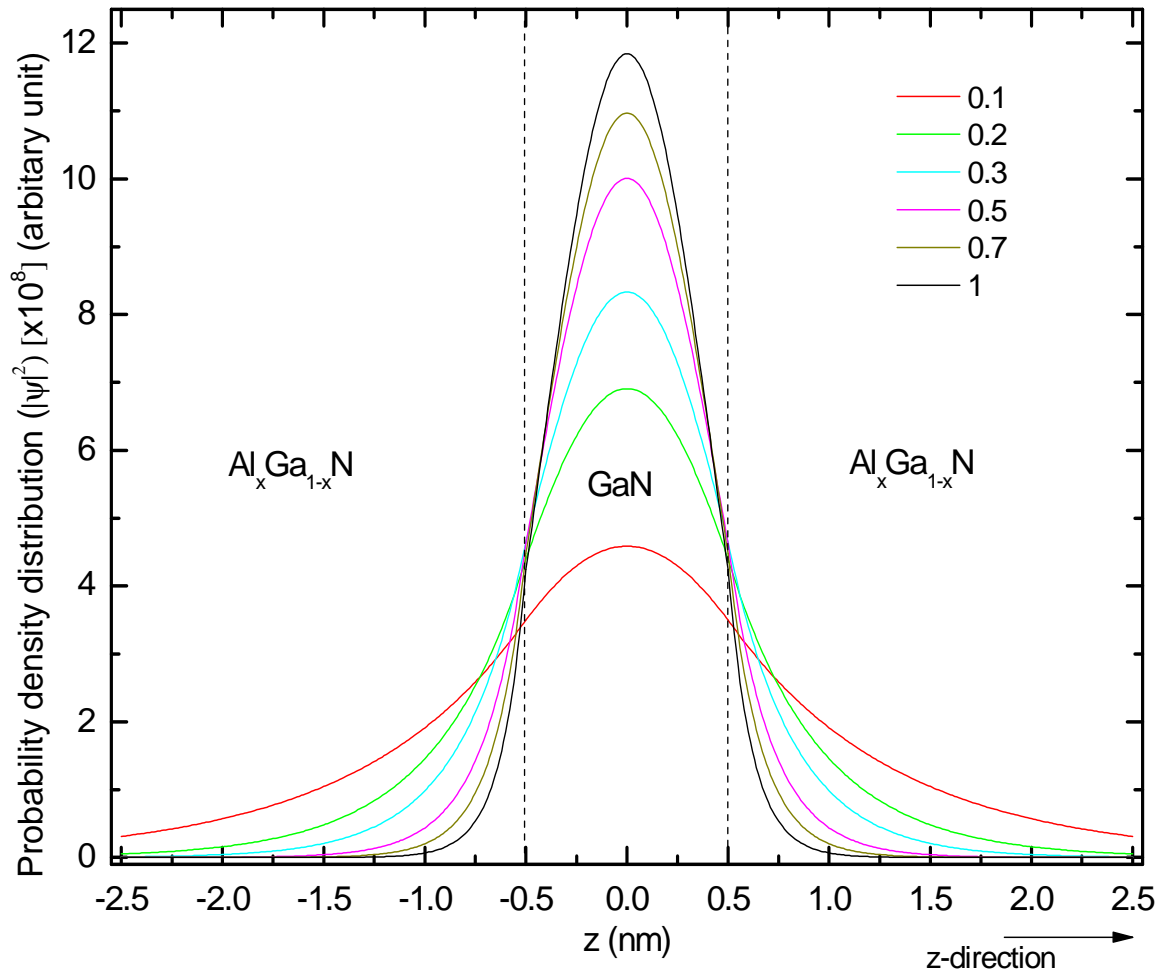


Figure 6.6: The calculated distribution of probability electron density at the conduction band for different Al composition, x of cubic $\text{Al}_x\text{Ga}_{1-x}\text{N}$ barrier layers.

Figure 6.7 shows the first resonant energy (lowest) in GaN well layer as a function of well width for a cubic $\text{Al}_{0.3}\text{Ga}_{0.7}\text{N}/\text{GaN}$ double barrier structure. The resonant energy, E_{pk} shows negative parabolic dependence with well width and this agrees with the experimental data for cubic $\text{Al}_x\text{Ga}_{1-x}\text{N}/\text{GaN}$ MQWs structures [21].

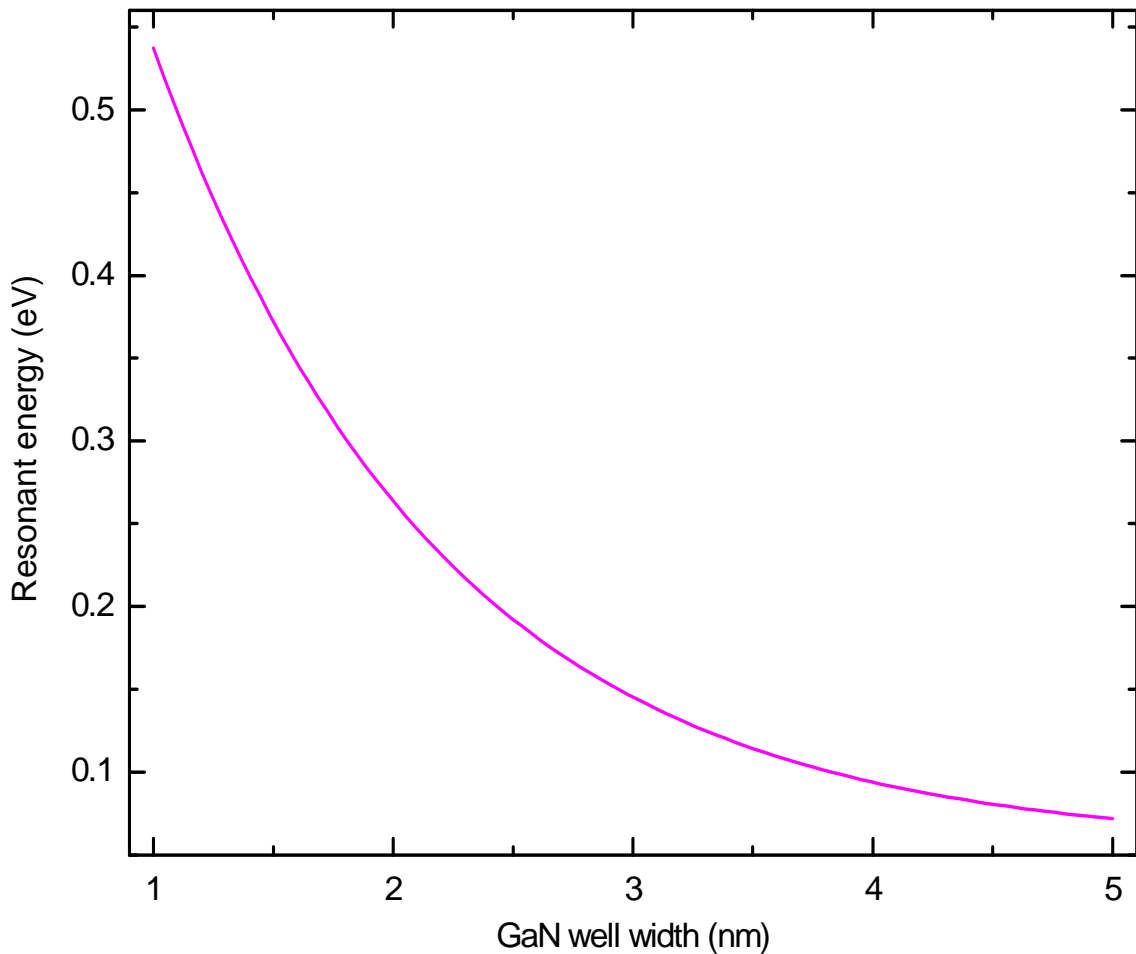


Figure 6.7: The calculated resonant energy level in the well as a function of well width.

6.4.2: Numerical Calculation of Tunnelling Current in $\text{Al}_x\text{Ga}_{1-x}\text{N}/\text{GaN}$ DBRTD

Until now, a large ambiguity in the value of the band offset for cubic $\text{Al}_x\text{Ga}_{1-x}\text{N}/\text{GaN}$ still remains. For this reason, the tunnelling transport property will be studied in the device using different values of the band offset in the calculation. The value of the band offset is determined by the values of electron affinities for different materials, which are GaN and $\text{Al}_x\text{Ga}_{1-x}\text{N}$ in our case. So far, the complete set of values for both materials in cubic structure is not available. Therefore the electron affinities in the stable phase, which is hexagonal (wurtzite) material, will be used as a first approximation. Table 6.1 shows the reported values of the electron affinity for GaN and AlN. In this case, the band offset of AlN/GaN at the conduction band is estimated at a given values of the electron affinity of GaN and AlN.

Table 6.1: List of the values of electron affinities for GaN and AlN from literature.

Electron affinity for GaN, χ_{GaN} , (eV)	Electron affinity for AlN, χ_{AlN} , (eV)	Conduction band offset ($\chi_{\text{GaN}} - \chi_{\text{AlN}}$), (eV)
3.4 [22]	1.9 [23]	1.5
4.1 [24]	1.9 [23]	2.2
4.1 [24]	0.6 [25]	3.5

Based on the figures in Table 6.1, we estimated the band offset for $\text{Al}_x\text{Ga}_{1-x}\text{N}/\text{GaN}$ using a process of linear interpolation. Figure 6.8 shows the tunnelling I - V characteristic of $\text{Al}_{0.3}\text{Ga}_{0.7}\text{N}/\text{GaN}$ DBRTD with different values of the conduction band offset. The conduction band offset of AlN/GaN , which is 1.5eV gives the band offset of $\text{Al}_{0.3}\text{Ga}_{0.7}\text{N}/\text{GaN}$ of 0.45eV, 2.2eV gives 0.66eV and 3.5eV gives 0.54eV, respectively.

In the figure, Curve 1 represents the conduction band offset of $\text{Al}_{0.3}\text{Ga}_{0.7}\text{N}/\text{GaN}$ for 0.45eV; curve 2 for 0.66eV and curve 3 for 0.54eV. The well and barrier widths are equal to 1nm. The NDR effect occurs at different voltages due to the different resonance energy, E_{pk} for each band offset. Clearly, it shows that the peak current is found to be smaller as the conduction band offset is higher. The increase in the band offset, which increases the barrier height, provides stronger carrier confinement in the well. Thus, the resonant width, Γ is more defined but there is a reduction of the electron tunnelling and consequently the peak current. However, our results show that the width of the resonance, Γ is only slightly lowered as the band offset is increased, indicating a very weak effect of the band offsets on the resonance width. For the rest of calculation, the value of 2.2eV for the AlN/GaN band offset will be adopted as this value is widely used in other work, e.g [26].

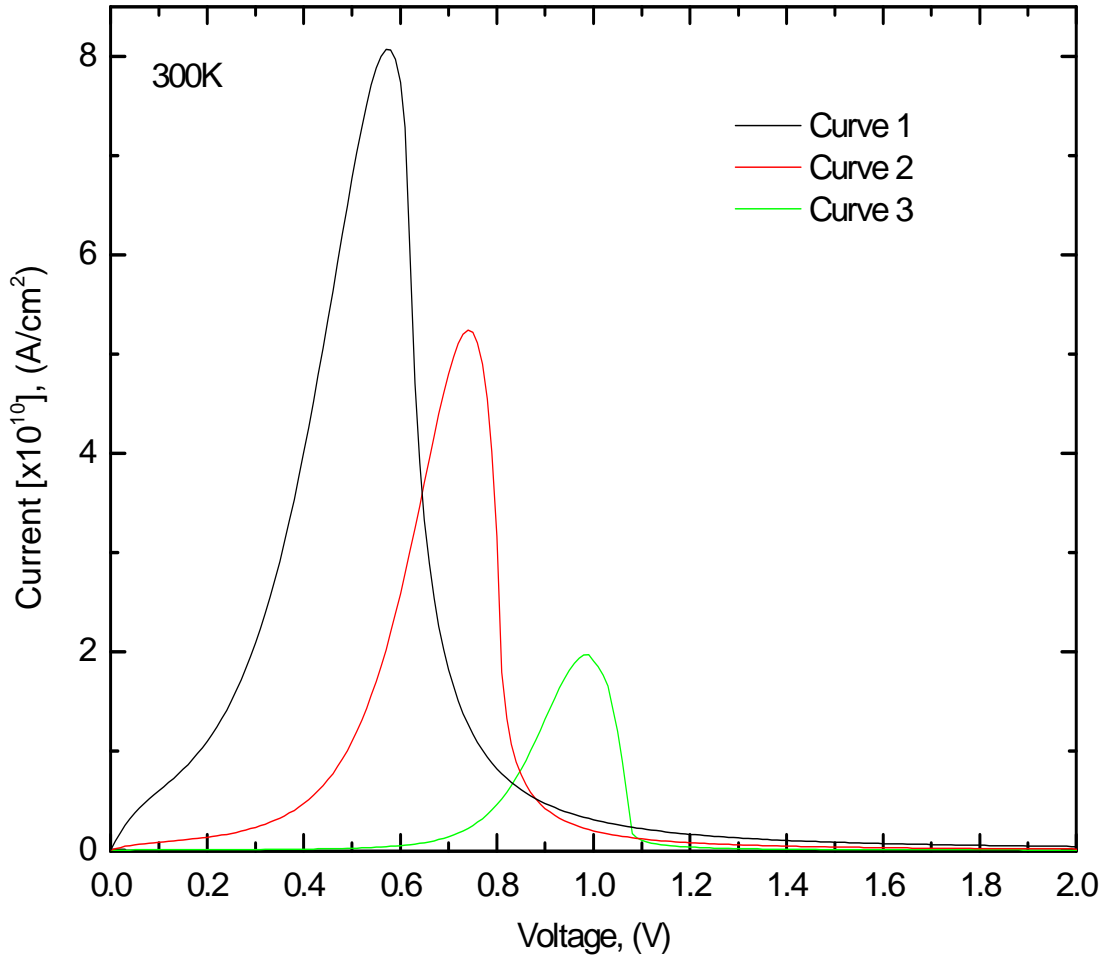


Figure 6.8: The calculated tunnelling current-voltage of $\text{Al}_{0.3}\text{Ga}_{0.7}\text{N}/\text{GaN}$ DBRTD with different conduction band offsets at room temperature.

Figure 6.9 shows the dependence of peak current and resonant width, Γ on well width, d_w for $\text{Al}_{0.3}\text{Ga}_{0.7}\text{N}/\text{GaN}$ DBRTD. Clearly, the peak current decreases as d_w is increased. In parallel, the resonant width, Γ also decreases when thickness is increased. In Figure 6.7, it is revealed that the increase in the well width lowers the value of E_{pk} . Detailed inspection of equation (6.16) shows that lowering this energy decreases the resonant width, Γ and this is consistent with [27]. Thus, the peak current is lower as the well width becomes larger. On the other hand, smaller width gives higher peak current, but the resonant width, Γ is larger. Therefore a compromise between these two effects should be achieved for optimal device performance.

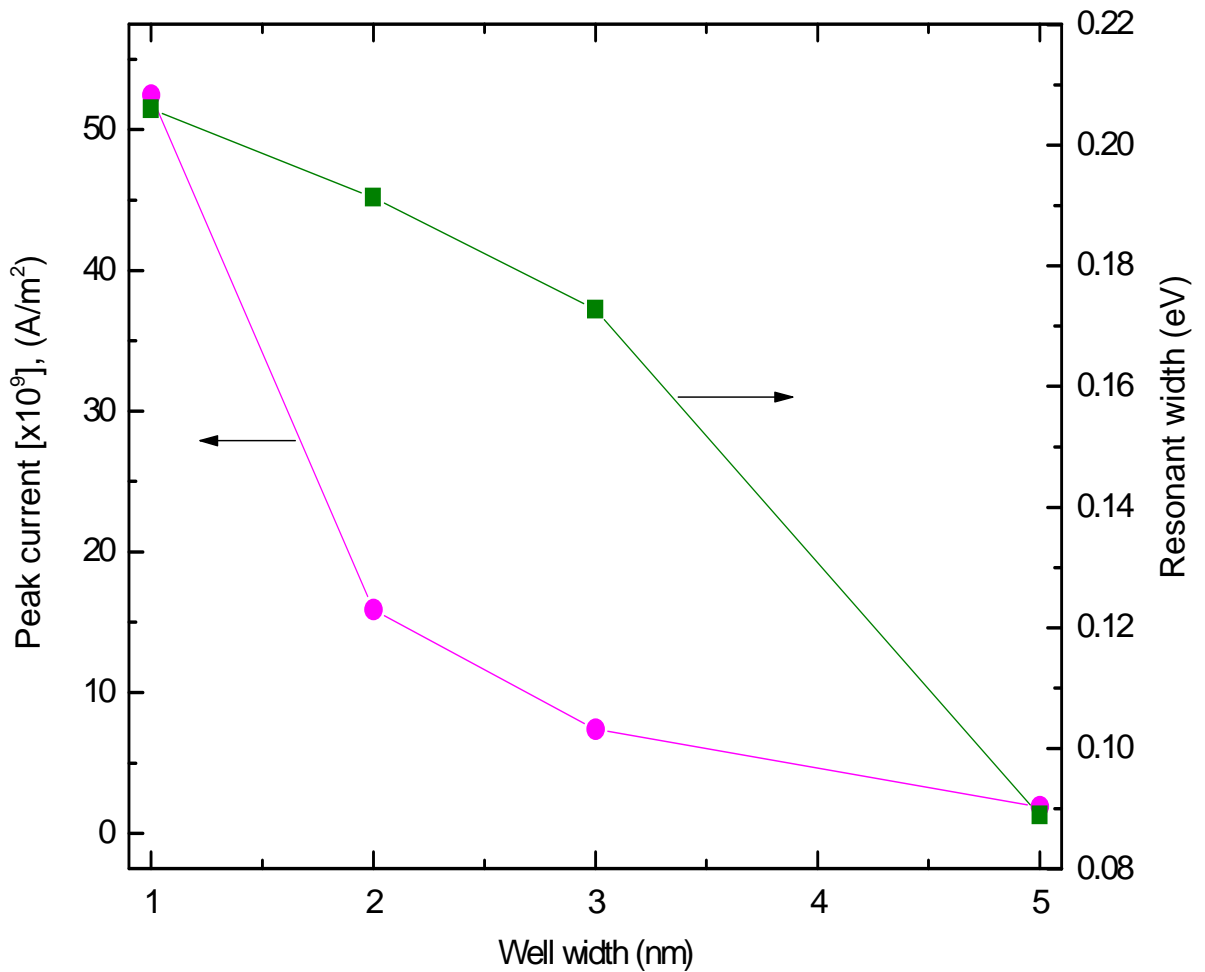


Figure 6.9: The dependence of peak current and resonance width on the well width in $\text{Al}_{0.3}\text{Ga}_{0.7}\text{N}/\text{GaN}$ double barrier device.

In addition to this work, the influence of using different barrier widths in the calculation is studied. Figure 6.10 shows the I - V characteristic for $\text{Al}_{0.3}\text{Ga}_{0.7}\text{N}/\text{GaN}$ DBRTD and the well width, $d_w = 1\text{nm}$ for different barrier width, d_b . Obviously, the peak current is found to be lower for larger barrier widths. Refer to equation (6.16), the increase in d_b reduces the resonant width, Γ and also decreases the peak current. Physically, this seems reasonable as the probability of electrons tunnelling across the barrier is limited by the thicker barrier.

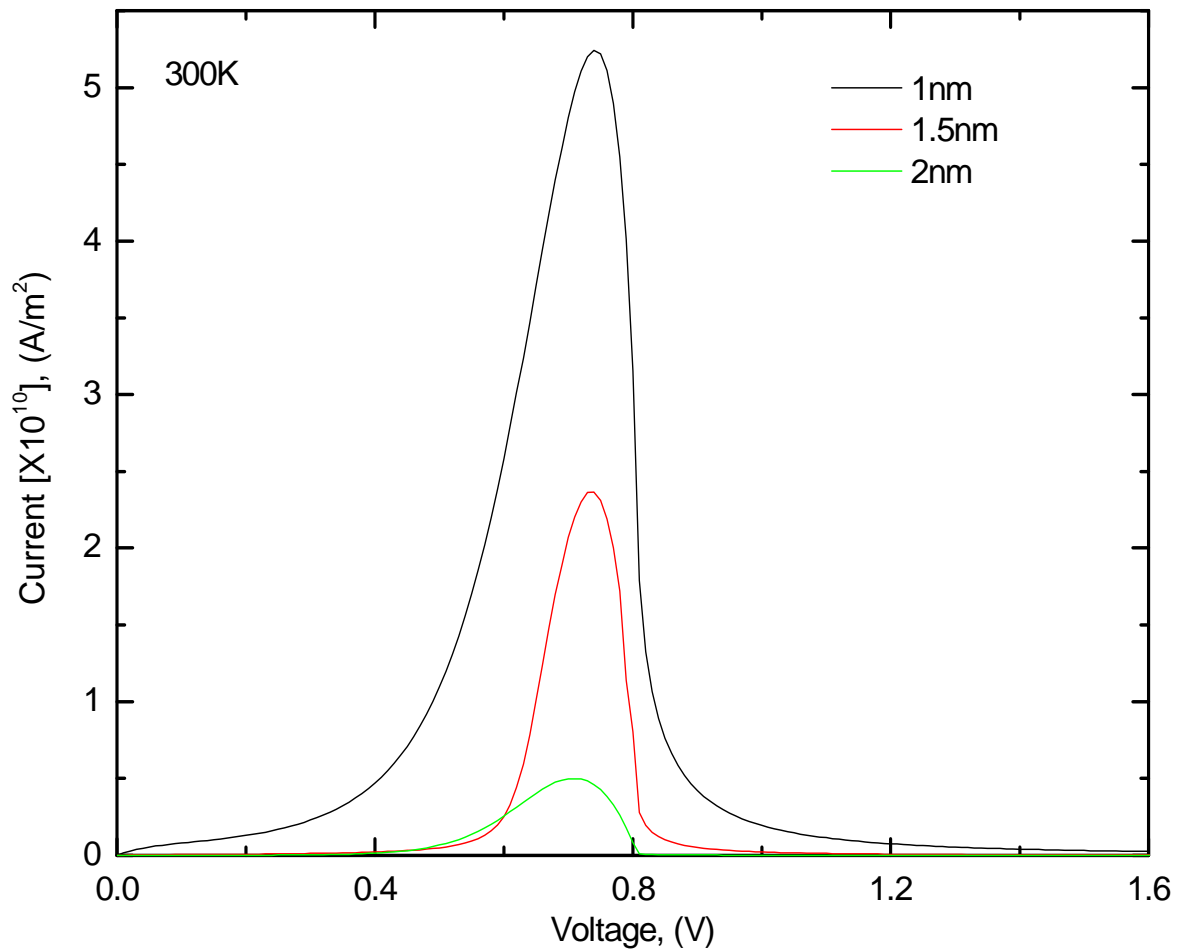


Figure 6.10: I - V characteristic for $\text{Al}_{0.3}\text{Ga}_{0.7}\text{N}/\text{GaN}$ DBRTD with different barrier thickness.

As been discussed previously, it is important to design a device structure that reaches a compromise between maximum peak current and minimum resonance width, Γ . Therefore, it is worthwhile to define a "figure of merit" for the device that gives the ratio of the peak current to the width of the resonant peak. In this work, detailed calculation found that this figure of merit has a maximum value for a certain barrier width d_b at a given Al composition, x and the result is shown in Figure 6.11. It is clearly shown that, as expected, the optimum barrier thickness is smaller for higher Al content.

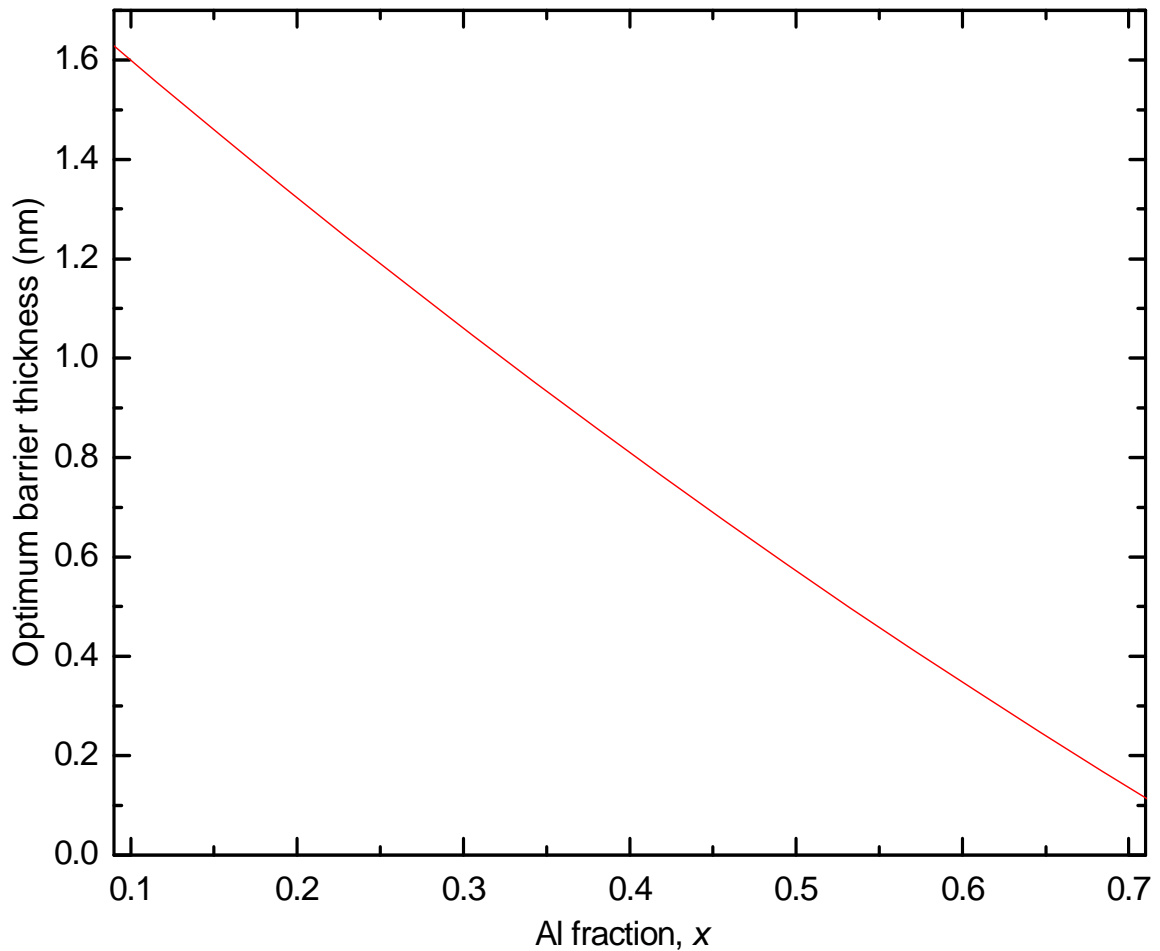


Figure 6.11: The optimum barrier thickness corresponding to the Al composition, x .

It is generally accepted that growing DBRTD structure with very thin (sub nm) barriers is problematic, particularly in the cubic $\text{Al}_x\text{Ga}_{1-x}\text{N}$ system. This is due to layer thickness fluctuation and increased probability of breakdown under bias. Moreover, growing with high Al fraction is difficult and previous investigation showed that the hexagonal inclusions increase with Al content. Thus, Figure 6.11 suggests that optimum structures may have barriers with less than 10% Al fraction and $d_b > 1\text{nm}$.

In addition, it is also important to understand the dependence of the tunnelling I - V characteristic with the variation of temperature. In this work, the tunnelling transport properties of the device with the optimal structural parameters for an $\text{Al}_{0.1}\text{Ga}_{0.9}\text{N}/\text{GaN}$ DBRTD are calculated at 300K and 77K, and the result is shown in Figure 6.12. From the figure, the peak current at 77K is found to be slightly lower than that at 300K. This is expected as the resonant energy in the quantum well

becomes more defined at low temperature but the peak current is lower. This result only applies to the ideal case, where effects like contact resistance, thermionic current across the barrier and structural fluctuation are not taken into account. In a real experiment, these effects could influence the transport properties in the tunnel diode, for example change in the peak current and the NDR voltage and shape of the NDR effect. The discussions on the experimental results are presented in next section.

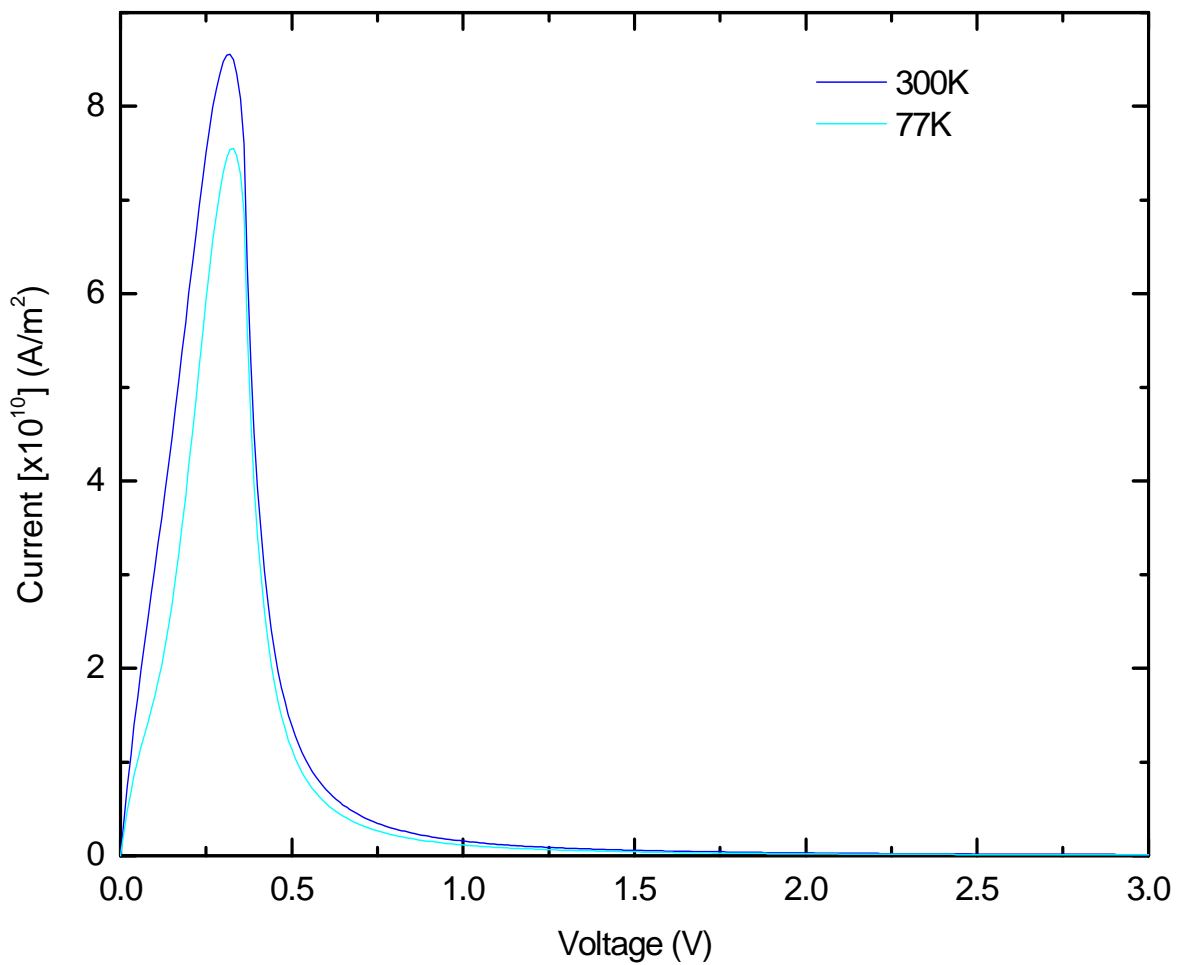


Figure 6.12: I - V characteristic for $\text{Al}_{0.1}\text{Ga}_{0.9}\text{N}/\text{GaN}$ DBRTD at different temperature.

6.5: VERTICAL TRANSPORT IN CUBIC $\text{Al}_x\text{Ga}_{1-x}\text{N}/\text{GaN}$ DBRTD

In this work, we have grown a number of cubic $\text{Al}_x\text{Ga}_{1-x}\text{N}/\text{GaN}$ DBRTD devices with different barrier heights, widths and lateral sizes by MBE. The vertical transport properties of the tunnel devices have been investigated through I - V measurement. In this work, we aim to find the tunnel devices that give a clear and reproducible NDR effect.

6.5.1: Vertical transport in bulk tunnel device

In the beginning of this work, a cubic $\text{Al}_{0.1}\text{Ga}_{0.9}\text{N}/\text{GaN}$ DBRTD with well and barrier widths of 2nm had been characterised. The size of the device is around 1mm^2 . A positive bias is applied on the top contact of the device, which corresponds to forward bias. Therefore electrons are injected from the bottom contact.

Figure 6.13 shows the I - V characteristic of the device at 300K and 77K. Like early measurement on III-arsenide tunnelling devices [28], no evidence of NDR is observed.

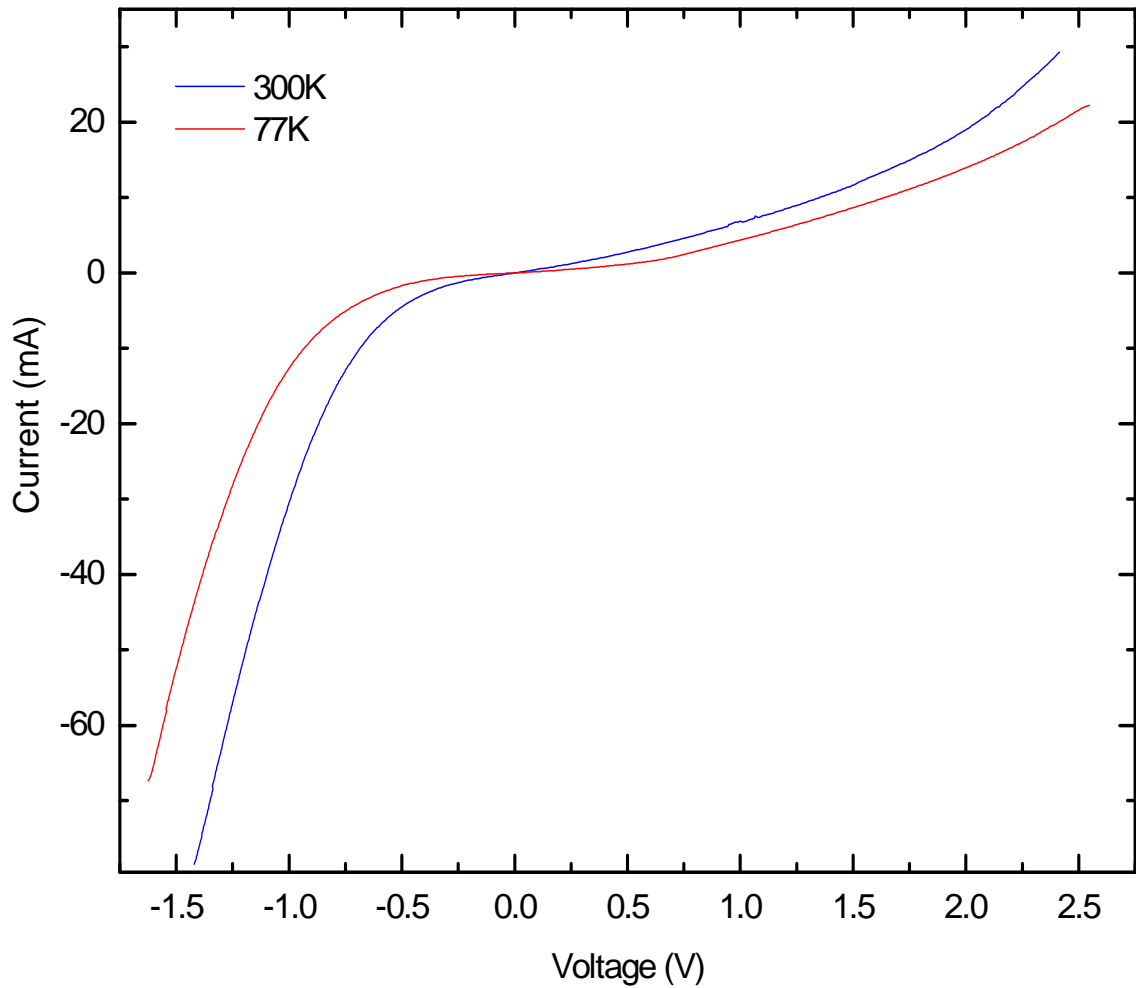


Figure 6.13: I - V characteristic for $\text{Al}_{0.1}\text{Ga}_{0.9}\text{N}/\text{GaN}$ DBRTD. No NDR is observed.

Figure 6.14 shows the dependence of conductance, dI/dV on the bias voltage for the tunnel device. It can be seen that there is a small signal around 0.6V. The signal may correspond to resonant tunnelling and it occurs at the voltage which is about 2 times higher than the calculated value. This difference probably arises from the structural fluctuation during growth, voltage drop across contact resistance [2] and scattering at defects and impurities. At room temperature, the signal is weaker, probably due to higher thermionic emission that considerably masks the evidence of the tunnelling in the device.

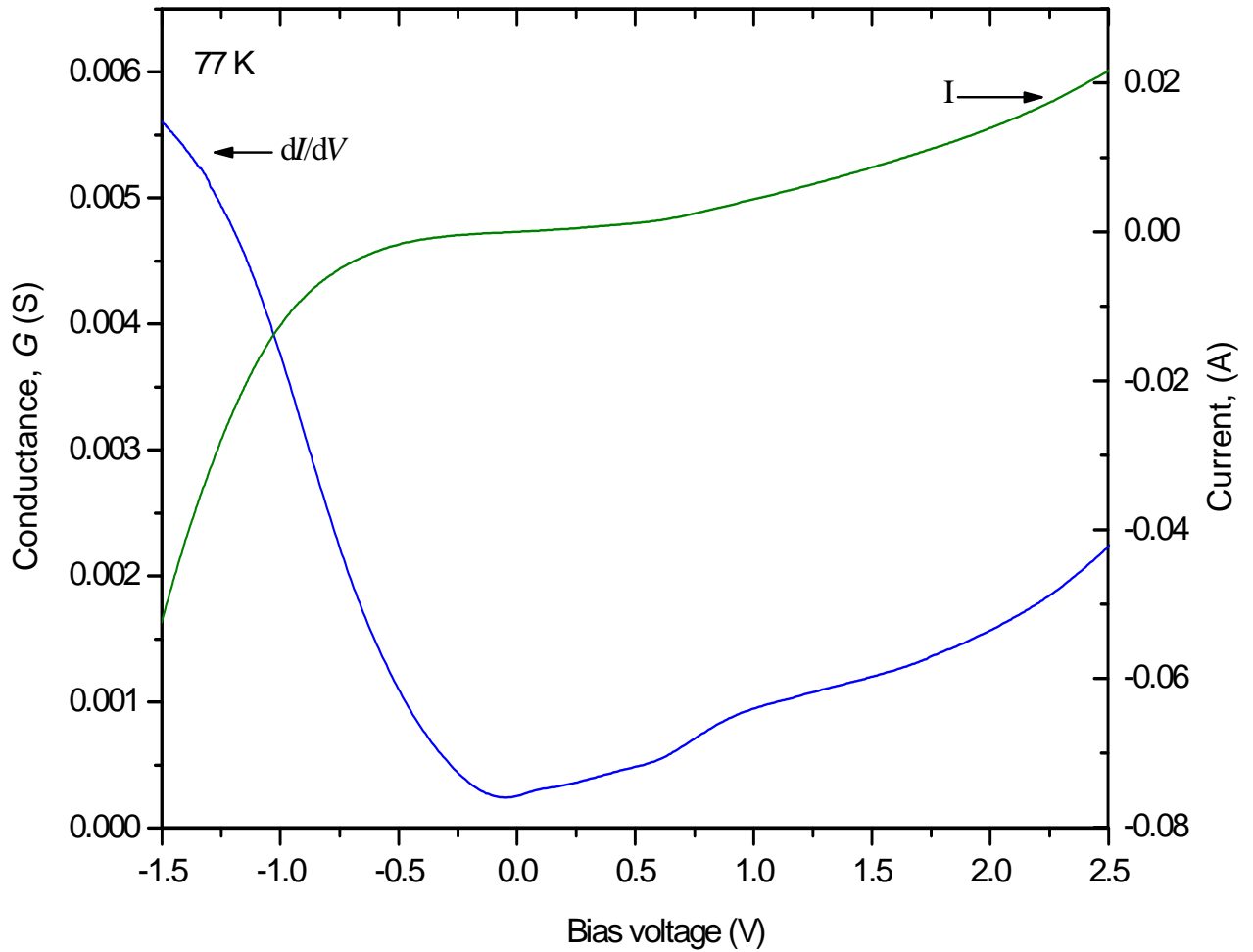


Figure 6.14: Dependence of the current and conductance, G on the applied voltage for $\text{Al}_{0.1}\text{Ga}_{0.9}\text{N}/\text{GaN}$ DBRTD at 77K. A weak feature can be observed around 0.6V in the G - V characteristic.

This observation indicates that the resonant tunnelling is negligible in I - V measurements. The difficulty in observing NDR could be due to the relatively large device used that causes the current contributions from structural fluctuation and scattering at defects and impurities to be more significant in the I - V characteristics. These factors mask the evidence of tunnelling in the device structure. However, such effects can be suppressed when the lateral size of the device is reduced. For this reason, we had fabricated a number of much smaller devices so that the NDR effect associated with tunnelling is clearly observed in the I - V characteristic.

6.5.2: Vertical transport in smaller device

Our simulation results suggested that the optimum structures may have barriers with less than 10% Al fraction and barrier widths, $d_b > 1\text{nm}$. However, in a real situation, lower barrier height could increase the current from the thermionic emission, particularly at room temperature, and consequently suppresses the appearance of NDR in the I - V characteristic. In the following work, a number of $\sim 50\mu\text{m}$ diameter mesas of cubic $\text{Al}_{0.3}\text{Ga}_{0.7}\text{N}/\text{GaN}$ tunnel devices with different structural parameters were fabricated by plasma etching. The well width is around 1nm for all type of samples. Table 6.2 shows the cubic $\text{Al}_{0.3}\text{Ga}_{0.7}\text{N}/\text{GaN}$ tunnel devices grown with different barrier widths and with or without a GaAs buffer layer to improve the crystalline quality of the device structure. Similar to the previous measurements, a positive bias is applied on the top of the device; therefore electrons are injected from the bottom contact. On the other hand, negative bias allows the electrons to be injected from the top contact.

Table 6.2: Detailed structure for the grown cubic $\text{Al}_{0.3}\text{Ga}_{0.7}\text{N}/\text{GaN}$ DBRTDs.

Wafer	Barrier width (nm)	GaAs Buffer layer (Yes/No)
SN-298	3	Yes
SN-299	5	Yes
SN-300	5	No
SN-301	3	No
SN-302	4	No

Figure 6.15 shows I - V characteristics for device SN-298 at room temperature. Clearly, there is a sharp NDR feature around 1.36V with a peak current $\sim 0.049\text{mA}$. The NDR voltage is found to be ~ 2 times higher than the theoretical prediction and this is probably due to voltage drops across other parts of the device and contact resistance in the device. Nonetheless, the NDR voltage is somewhat close to [9, 29]. The peak to valley ratio (PVR) is approximately 3.37 and it is almost similar to the typical value of PVR for hexagonal $\text{Al}_x\text{Ga}_{1-x}\text{N}/\text{GaN}$ DBRTD structures [9, 29, 30].

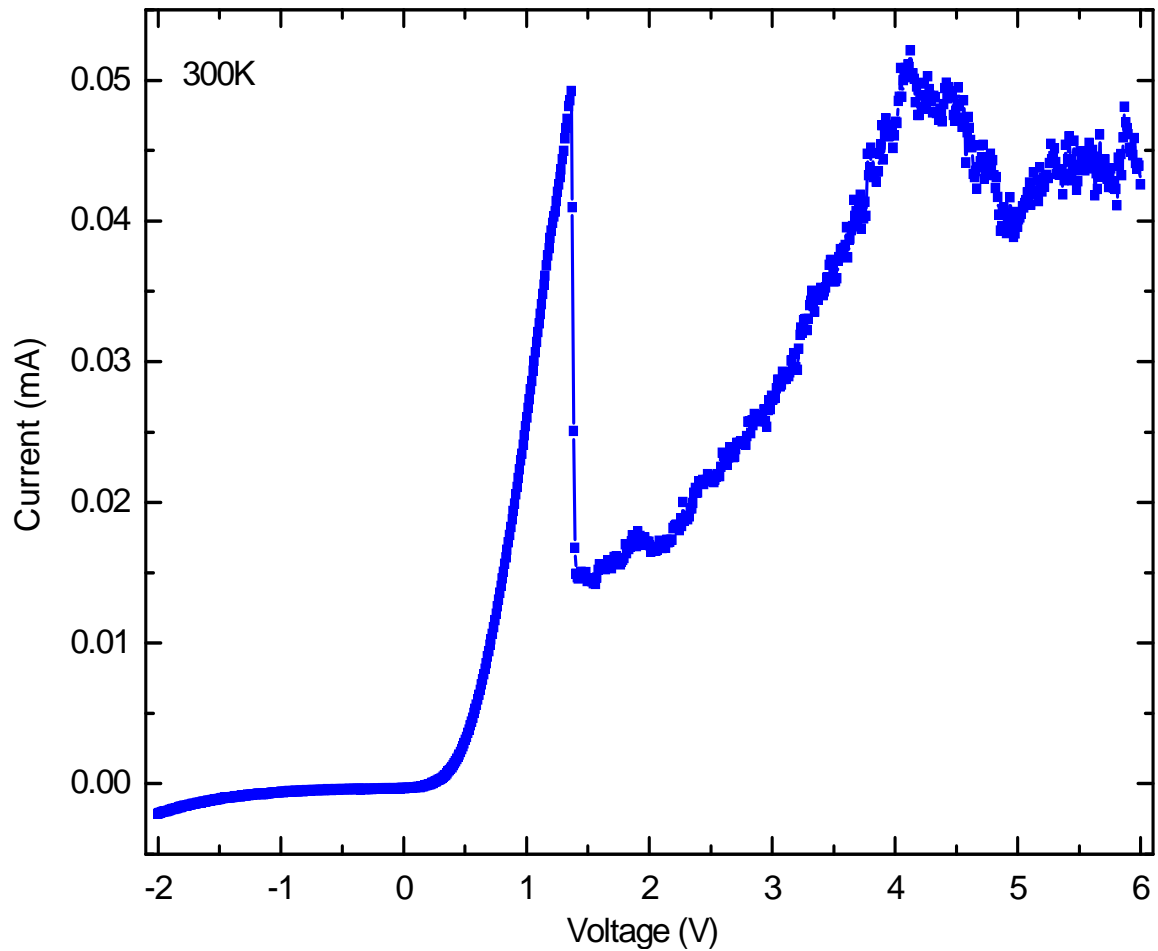


Figure 6.15: Dependence of current on applied voltage for SN-298. The device shows a sharp NDR effect around 1.3V.

It is important to confirm that the observed NDR effect in these devices is related to the existence of the barrier layers. In this work, we prepared a structure without the $\text{Al}_{0.3}\text{Ga}_{0.7}\text{N}$ barrier layers. From the measurement, the structure showed a typical diode characteristic and the result is reproducible for a number of measurements. This suggests that the observed NDR effect must be associated with the presence of barriers in the structure.

Moreover, the figure points out that the asymmetry of the I - V characteristic is due to the asymmetry of the potential in the device structure. Current for negative bias is negligible due to Schottky barrier between n^+GaAs and GaN layers. From the figure, the turn on voltage of the Schottky diode is about 0.5V.

A number of devices had to be measured in order to find one that shows the NDR effect on the I - V characteristic. We suggest that the fluctuation of the grown layers may explain this behaviour. For example, some devices could have too small or too large barrier width and height that make current contributions from other mechanisms become more significant, which considerably suppress the evidence of the NDR effect in I - V characteristic.

Figure 6.16 shows I - V characteristic for device SN-299 at low temperature. The NDR effect can be clearly seen at ~ 1.36 V with a peak current and a PVR value of 0.19mA and 2.88, respectively. The NDR voltage is found to be similar to device SN-298 as the well width in both devices is identical. Nevertheless, there are differences in the peak current and the PVR value in these devices and this could be due to the variation in the barrier widths. We suggest that the second NDR at ~ 2.74 V corresponds to the maximum tunnel current at the second resonant level as this value is somewhat close to the estimated calculation, which is about 2.10V.

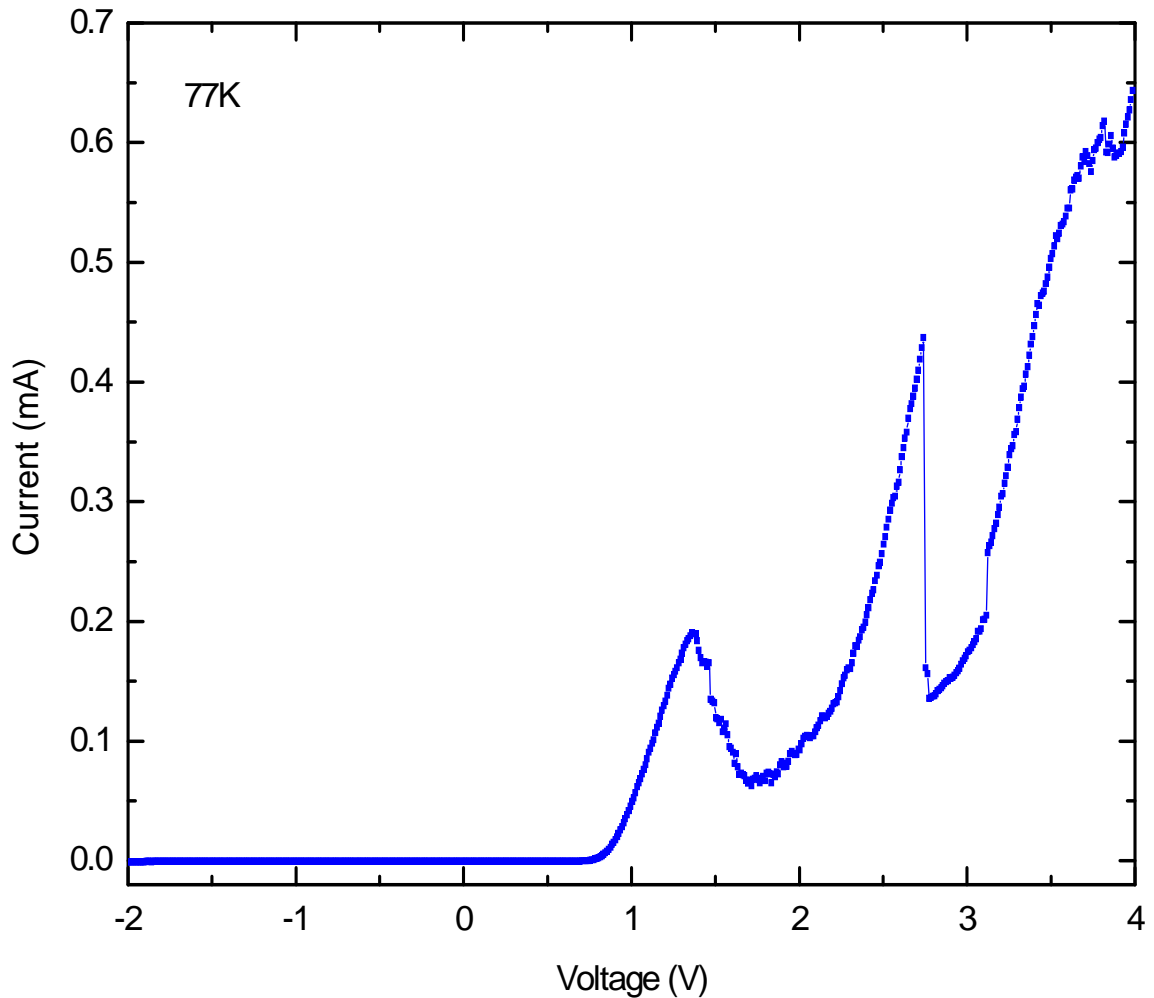


Figure 6.16: I - V characteristic for SN-299 at low temperature. Clearly, the NDR effect is observed at 1.36V.

So far, we have demonstrated the evidence of NDR in several cubic $\text{Al}_{0.3}\text{Ga}_{0.7}\text{N}/\text{GaN}$ DBRTD devices. Next, the reproducibility of the NDR effect of the tunnel device is investigated. Previous studies on hexagonal nitride devices reported that the NDR effect only appears once when sweeping from negative to positive bias and this is attributed to the large charge trapping phenomena due to piezoelectric and spontaneous fields in the device. It is well known that such fields are absent in the cubic nitride system. Here, we initially speculate that charge trapping in our case may originate from the internal fields near defects. To release the carriers from the traps, we propose to sweep the device in the opposite direction and then sweep it back to positive bias. Figure 6.17 shows the electrical properties of device SN-298 for different directions of bias sweeping. Curve 1 shows the first sweep from -2 to 6V. On the subsequent sweep, the device is swept in opposite direction from 6 to -

6V and the result is indicated by Curve 2. There is no NDR is observed and this agrees with the experimental observation by [9]. When the device is swept back from 0 to -6V (Curve 3), the NDR feature still can not be reproduced.

As has been demonstrated in [8], we also heated up the sample at 350°C, so that the trapped carriers could be released. Apart from that, we also shone UV light on the sample to restore the carriers from any traps. However, the NDR effect in the device is not reproducible in both experiments. This clearly shows that the irreproducibility of the result is not related to the trapping phenomena, which we wouldn't expect in cubic material. We suspect that the device is already damaged due to high applied voltage and therefore no NDR effect can be observed again on the subsequent measurements.

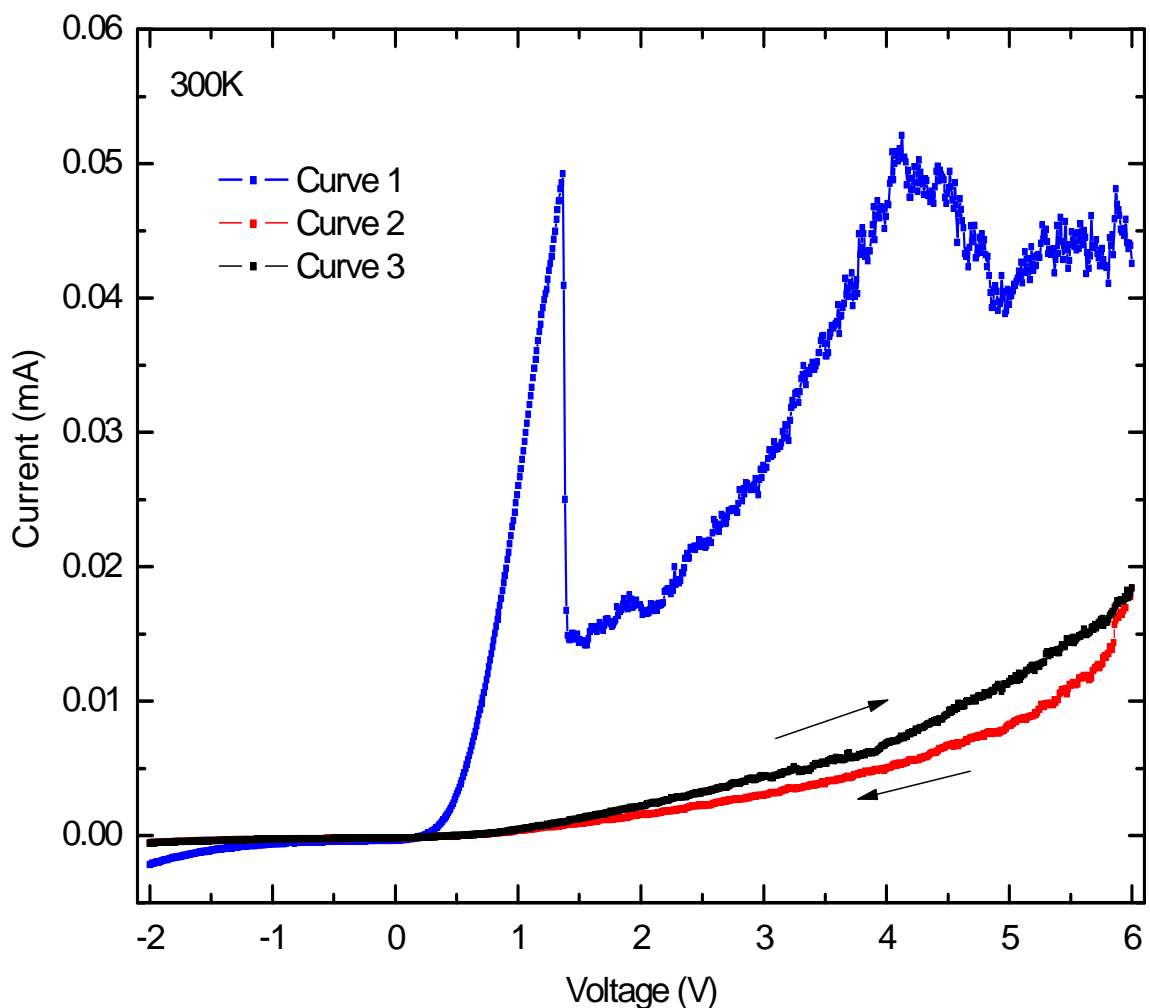


Figure 6.17: I - V characteristic at different bias for SN-298. Clearly the NDR effect disappears in the subsequent sweeping.

In the next experiment, we used a different technique of measurement, where we immediately stopped the sweeping a few points after the end of the peak to prevent the device from breaking down. From that point, we swept the device down to negative bias and then swept it again from the negative towards the positive bias.

Figure 6.18 shows the I - V characteristic for another device of SN-298, using this technique. Clearly, the NDR feature is reproduced in the subsequent positive sweep (from negative to positive side) and this reveals that the NDR feature is not related to the permanent breakdown of the device.

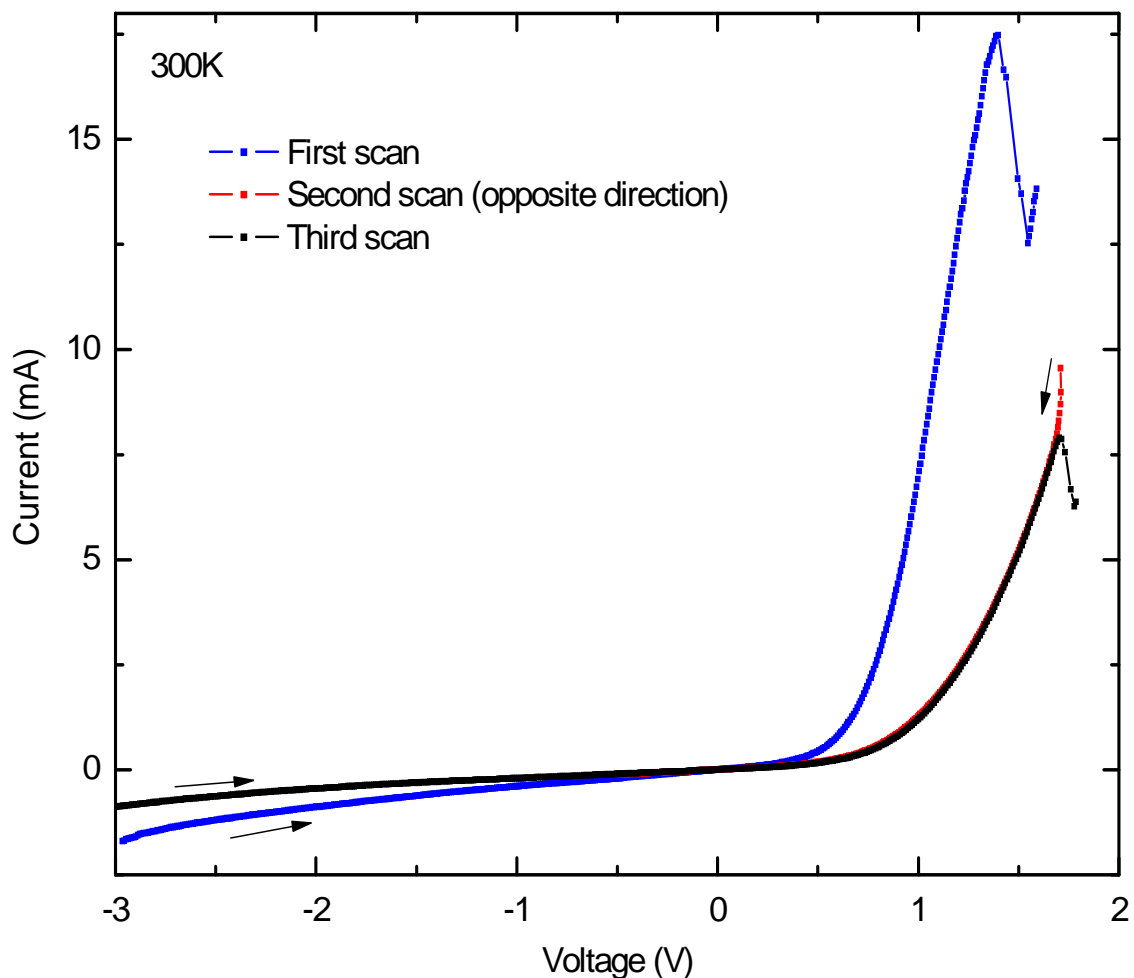


Figure 6.18: I - V characteristic for another device of SN-298 using a different sweeping technique. Clearly, the NDR effect is observed in the subsequent measurements.

The first sweep exhibits the NDR effect at 1.4V with a peak current and a PVR value of 17.60mA and 1.39, respectively. The NDR voltage for this device almost agrees with that for the first sample (refer to Figure 6.15) but its PVR value is lower. This is probably due to large background current (associated with non-resonant tunnelling, thermionic emission over the barriers, scattering assisted tunnelling process and leakage current through the surface states) that increases the valley current and consequently decreases the PVR. The change of the peak current and the shift in the NDR position in the subsequent positive sweep could be due to strong hysteresis that is typically expected in III-V nitrides.

The evidence of the hysteresis in our cubic tunnel device is clearly shown in Figure 6.19 for device (SN-302) at 77K. As can be seen, the position and the height of the NDR change between different sweeps. The strong hysteresis is generally expected from a wide energy gap and large band discontinuity in the nitrides system. The hysteresis phenomena is also commonly observed in GaAs devices [31, 32].

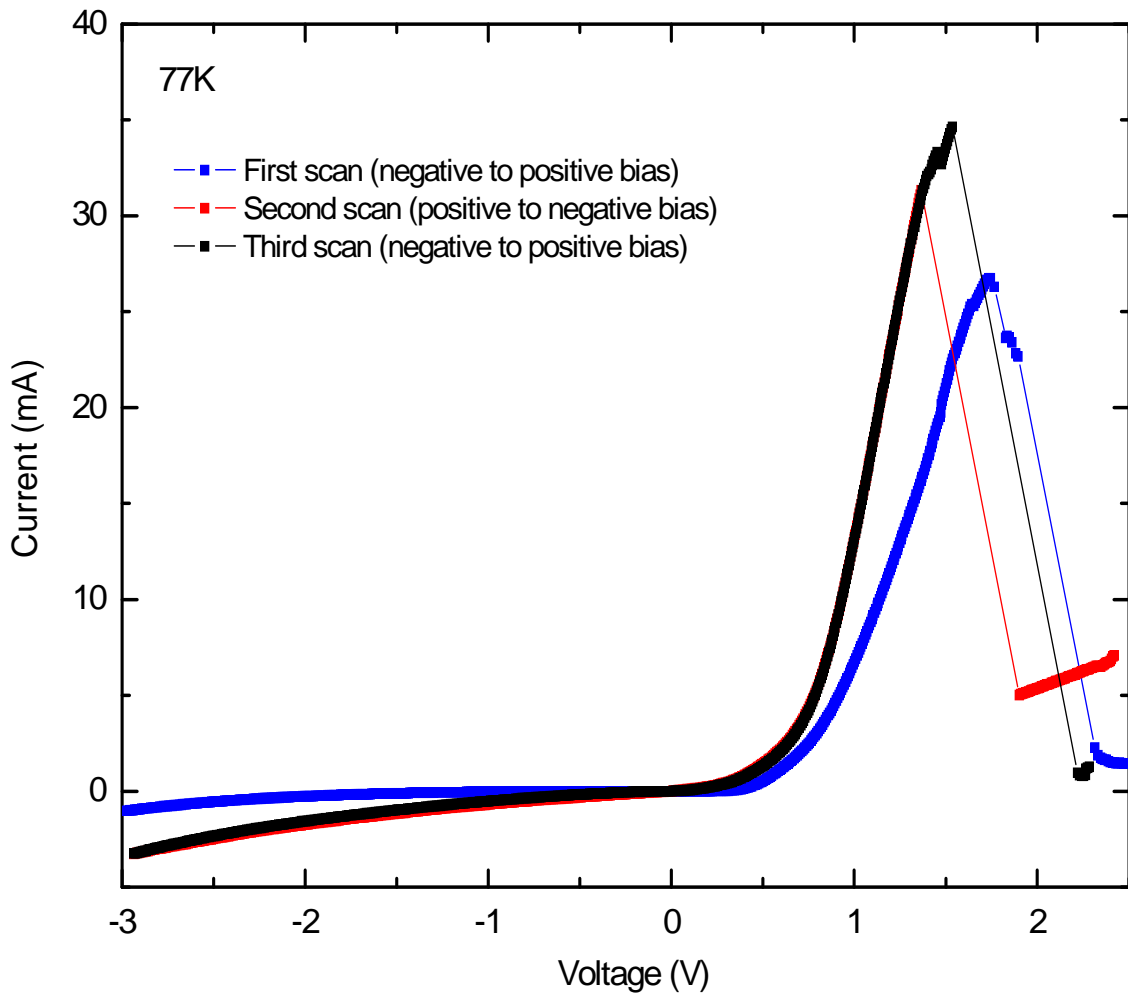


Figure 6.19: I - V characteristic for SN-302 at different bias. Clearly, the signal of hysteresis is observed.

Figure 6.20 shows the I - V characteristic for some tunnel devices with different structures (refer to Table 6.2) for the first sweep at 77K. It can be seen that the NDR voltage differs slightly between different devices even though the well width is similar in those devices. This is probably related to the existence of defects, contact resistance and variation in the grown layer.

Nonetheless, the peak current varies considerably in different devices. The peak current is found to be lower as the barrier width increases and this agrees with our theoretical prediction. As the barrier becomes larger, the probability of electron tunnelling through the barrier decreases and consequently reduces the peak current.

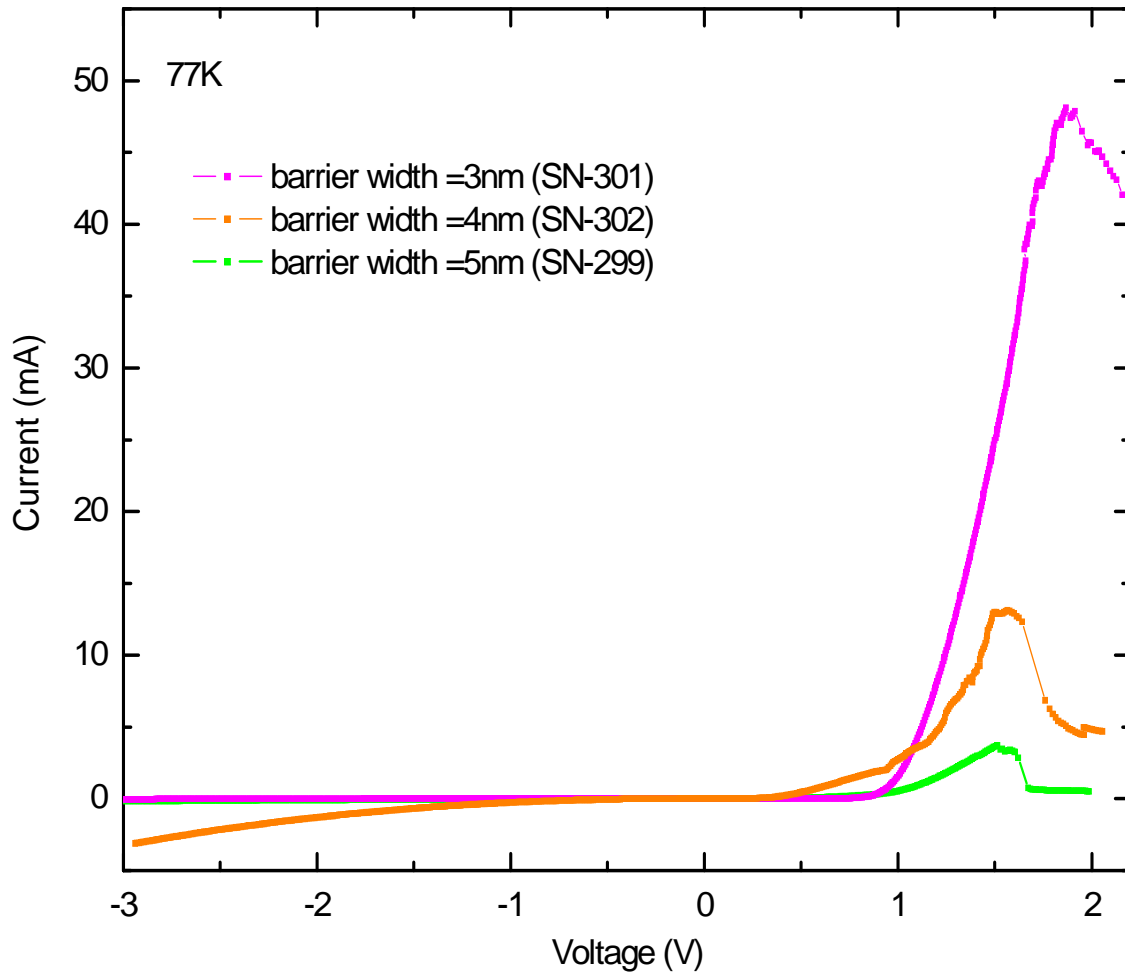


Figure 6.20: *I-V* characteristic for some cubic $\text{Al}_{0.3}\text{Ga}_{0.7}\text{N}/\text{GaN}$ devices with different structural parameters. The NDR effect is observed in all type of the samples.

Tables 6.3 and 6.4 summarise the tunnelling transport properties for all cubic $\text{Al}_{0.3}\text{Ga}_{0.7}\text{N}/\text{GaN}$ DBRTD devices with the variation of structural parameters at 300K and 77K, respectively. In general, device SN-298, SN-301 and SN-302 are highly reproducible. These devices have the barrier widths in between 3-4nm. However, the devices with 5nm barrier widths hardly give reproducible results at all. This shows that the change in the barrier width plays the main role in influencing the transport properties in cubic $\text{Al}_{0.3}\text{Ga}_{0.7}\text{N}/\text{GaN}$ DBRTD rather than the growth of a buffer layer.

Table 6.3: Summary of the results from *I-V* measurement at 300K.

Wafer	Barrier width (nm)	Buffer (Yes/No)	Device number	Peak voltage (V)	Peak current density (A-cm ⁻²)	Peak to valley ratio	Reproducible (Yes/No)
SN-298	3	Yes	1	1.40	896.24	1.39	Yes
			2	1.48	564.91	-	Yes
			3	1.75	616.68	1.33	Yes
			4	1.36	2.50	3.37	No
			5	1.3	112.03	2.5	No
SN-299	5	Yes	1	1.27	194.02	1.64	Yes
			2	4.38	0.51	1.25	No
SN-300	5	No	1	2.14	144.62	1.14	No
			2	2.87	4.58	3.52	No
			3	1.82	36.16	2.02	No
			4	2.26	14.26	3.45	No
SN-301	3	No	1	2.13	16.80	1.46	Yes
			2	2.29	15.79	1.91	Yes
SN-302	4	No	1	1.20	295.35	1.70	Yes

Table 6.4: Summary of the results from *I-V* measurement at 77K.

Wafer	Barrier width (nm)	Buffer (Yes/No)	Device number	Peak voltage (V)	Peak current density (A-cm ⁻²)	Peak to valley ratio	Reproducible (Yes/No)
SN-298	3	Yes	6	1.64	56.02	-	No
SN-299	5	Yes	3	1.51	187.40	-	No
			4	1.36	9.68	2.88	No
SN-300	5	No	5	2.28	212.86	1.71	No
SN-301	3	No	4	1.88	2436.66	-	Yes
			5	1.82	835.14	1.22	Yes
			6	2.12	220.50	1.82	No
			7	1.87	238.32	-	No
SN-302	4	No	2	1.60	57.54	-	Yes
			3	1.75	1366.77	-	Yes
			4	1.57	667.60	2.94	Yes

Statistically, there is a correlation between irreproducibility and low current, for instance, SN-298 at 300K and SN-301 at 77K. We do not have a precise explanation for this behaviour. However, we may speculate the following:

As has been mentioned before, the dimension of our cubic tunnel devices is about $50\mu\text{m}$ diameter. However, we must be aware that not all parts of the device are working because of problems like non-uniformity of the grown materials and damage to the device during etching process. Therefore, the active area may vary in different tunnel devices. Ideally, the current density should be similar in the same device structure. Thus, if the active area is small then the current would be low.

If the active device is too small, the problem related to the structural fluctuation would be more pronounced. From the statistics, the NDR voltage is fairly consistent in different devices with the same structure. This implies that the fluctuation in the well width is not the major problem. However, it is suggested that the variation in the barrier thickness must be responsible for the irreproducibility of the device. This is possible due to the increased difficulty of growing cubic $\text{Al}_x\text{Ga}_{1-x}\text{N}$. This is illustrated in Figure 6.21.

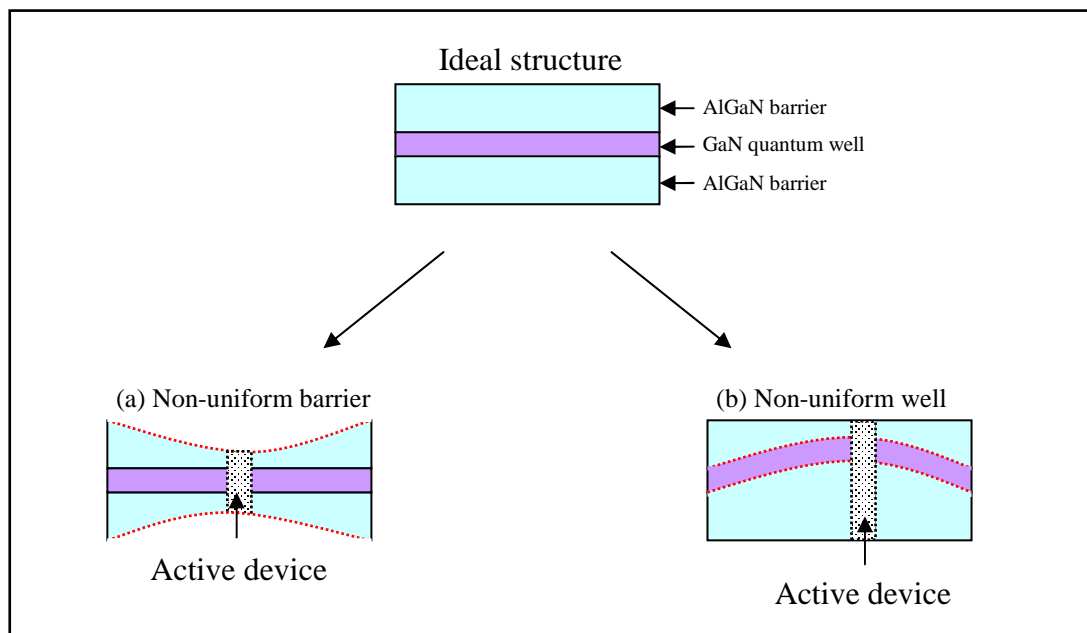


Figure 6.21: Two possible consequences of structural fluctuations during the growth.

The figure indicates how the barrier could be very small in the active area if the well or barrier layers are not uniformly grown. Where the barrier is thin, the tunnel current is concentrated there. However, the applied electric field is high and may

destroy the barrier leading to the breakdown of the device. From this mechanism, we propose that the irreproducibility of the tunnel devices at low current is caused by the small active area within the device, which causes the structural fluctuation problem to become more significant thus leading to breakdown of the device. Such a mechanism could also explain the irreproducibility of tunnel diodes in wurtzite (hexagonal) III-V nitrides as well as charge trapping phenomena.

6.6: CONCLUSIONS

In this chapter, an introduction to the underlying background physics on RTD structures has been presented. This is followed by a detailed numerical calculation of tunnelling I - V characteristic with the variation of band offset, well width, barrier composition and barrier thickness for cubic $\text{Al}_x\text{Ga}_{1-x}\text{N}/\text{GaN}$ devices. This calculation work proposes that the effects of the peak current and peak width need to be compromised for achieving optimum performance of the tunnel device. These results have been used to grow and characterise cubic $\text{Al}_x\text{Ga}_{1-x}\text{N}/\text{GaN}$ RTD devices with different structural parameters. We have successfully demonstrated that some tunnel devices show a clear NDR effect but not all of them are reproducible, probably due to severe problems with fluctuations in the grown layer.

REFERENCES

1. A. Kikuchi, R. Bannai, K. Kishino, Phys. Stat. Sol. (a), (2001). **188**: p. 187.
2. Akihiko Kikuchi, R. Bannai, Katsumi Kishino, Chia-Ming Lee, Jen-Inn Chyi, Appl. Phys. Lett., (2002). **81**: p. 1729.
3. C.T. Foxon, S.V. Novikov, A.E. Belyaev, L.X. Zhao, O. Makarovksy, D.J. Walker, L. Eaves, R.I. Dykeman, S.V. Danylyuk, S.A. Vitusevich, M.J. Kappers, J.S. Barnard, C.J. Humphreys, Phys. Stat. Sol. (c). (2003). **0**: p. 2389.
4. A.E. Belyaev, C.T. Foxon, S.V. Novikov, O. Makarovsky, L. Eaves, M.J. Kappers, C.J. Humphreys, Appl. Phys. Lett., (2003). **83**: p. 3626.
5. A.E. Belyaev, O. Makarovsky, D.J. Walker, L. Eaves, C.T. Foxon, S.V. Novikov, L.X. Zhao, R.I. Dykeman, S.V. Danylyuk, S.A. Vitusevich, M.J. Kappers, J.S. Barnard, C.J. Humphreys Physica E, (2004). **21**: p. 752.
6. A.E. Belyaev, C.T. Foxon, S.V. Novikov, O. Makarovsky, L. Eaves, M.J. Kappers, J.S. Barnard, C.J. Humphreys, S.V. Danylyuk, S.A. Vitusevich, A.V. Naumov, Semiconductor Physics, Quantum Electronics & Optoelectronics, (2004). **7**: p. 175.
7. C. Bayram, Z. Vashaei, M. Razeghi, Appl. Phys. Lett., (2010). **96**: p. 042103.
8. S. Golka, C.P. W. Schrenk, G. Strasser, C. Skierbiszewski, M. Siekacz, I. Grzegory, S. Porowski, Appl. Phys. Lett. , (2006). **88**: p. 172106.
9. S. Leconte, S. Golka, G. Pozzovivo, G. Strasser, T. Remmele, M. Albrecht, E. Monray, Phys. Stat. Sol (c) (2008). **5**: p. 431.
10. D.R. Hang, C.T. Liang, C.F. Huang, Y.H. Chang, Y.F. Chen, H.X. Jiang, J.Y. Lin, 79 66 (2001), Appl. Phys. Lett., (2001). **79**: p. 66.
11. N.Tang, B. Shen, M.J., Wang, Z.J. Yang, K. Xu, G.Y. Zhang, T. Lin, B. Zhu, W.Z. Zhou, J.H. Chu, Appl. Phys. Lett., (2006). **88**: p. 172115.
12. G.Ramírez-Flores, H., Navarro-Contreras, A. Lastras-Martínez, R. C. Powell, J.E. Greene, Physical Review B, (1994). **50**(12): p. 8433.
13. R. Tsu, L. Esaki Appl. Phys. Lett., (1973). **22**: p. 562.
14. Davies, J.H., *An Introduction: The Physics of Low-Dimensional Semiconductors*. (1998): Cambridge University Press.
15. M. Fanciulli, T. Lei, T.D. Moustakas, Phys. Rev. B, (1993). **48**: p. 15144.
16. T. Suzuki, H. Yaguchi, H. Okumura, Y. Ishida, S. Yoshida, Jpn. J. Appl. Phys. , (2000). **39**: p. L497.
17. I. Vurgaftman, J.R. Meyer, L.R. Ram-Mohan, J. Appl. Phys., (2001) **89**: p. 5815.
18. M. Marques, L.K. Teles, L.M.R. Scalfaro, J.R. Leite, Appl. Phys. Lett., (2003). **83**: p. 5.
19. Margarita P. Thompson, G.W. Auner, Tsvetanka S. Zheleva, Kenneth A. Jones, Steven J. Simko, James N. Hilfiker, J. Appl. Phys. , (2001). **89**: p. 3331.
20. E.E. Mendez, E. Calleja, W.I. Wang, Physical Review B (1986). **34**: p. 6026.
21. D.J. As, Microelectronics Journal, (2009). **40** p. 204.
22. R.Y. Korotkov, J.M. Gregie, B. W. Wessels, Appl. Phys. Lett., (2002). **80**: p. 1731.
23. C.I. Wu, A. Kahn, Appl. Phys. Lett., (1999). **74**: p. 546.
24. S. Arulkumaran, T. Egawa, H. Ishikawa, T. Jimbo, M. Umeno, Appl. Phys. Lett., (1998). **73**: p. 809.

25. V.M. Bermudez, T.M. Jung, K. Doverspike, A. E. Wickenden, J. Appl. Phys., (1996). **79**: p. 110.
26. C.I. Wu, A. Khan, J. Vac. Sci. Technol. B, (1998). **16**: p. 2218.
27. M. Tsuchiya, H. Sakaki, Appl. Phys. Lett., (1986). **49**: p. 88.
28. L.L Chang, L. Esaki, R. Tsu, Appl. Phys. Lett. , (1974). **24**: p. 593.
29. A. Kikuchi, R. Bannai, K. Kishino, Phys. Stat. Sol. (a) (2001). **188**: p. 187.
30. S. Leconte, S.G. G. Pozzovivo, G. Strasser, T. Remmele, M. Albrecht, E. Monroy, Phys. Stat. Sol. (c) (2008). **5**: p. 431.
31. T. Wei, S. Stapleton, J. Appl. Phys., (1995). **77**: p. 4071.
32. Alan C. Seabaugh, Yung-Chung Kao, Han-Tzong Yuan, IEEE Electron Device Letters, (1992). **13**: p. 479.

CHAPTER 7: CONCLUSIONS AND FUTURE PLANS

This chapter summarises the outcome from the studies of cubic GaN materials that have been carried out in this thesis. The use of cubic GaN in various aspects of device applications was also demonstrated. At the end of this chapter, some suggestions for future research will be outlined.

7.1: STUDIES OF CUBIC GaN

In the early part of this project, we reported a study on cubic GaN material with the variation of III/V ratio, growth rate and wafer position. Using PL and XRD measurements, we found that all these factors influence the increase of hexagonal inclusions in cubic GaN, leading to poor quality in cubic nitride growth. This problem however is more significant when the thickness of cubic GaN is increased. From the calibration work, a $\sim 50\mu\text{m}$ cubic GaN layer has been grown for the first time with a low average proportion of hexagonal inclusions of around 10% and just few percent at the interface of cubic GaN and GaAs substrate. Thus, the interface would be the most suitable surface for further growth.

Next, we investigated the fundamental properties of cubic GaN using picosecond acoustic measurements. In this material, the sound velocity is found to be 6.9 ± 0.1 kms^{-1} , elastic constant = 285 ± 8 GPa and the refractive index at 400nm = 2.63 ± 0.04 . Comparison with hexagonal GaN films indicated that these parameter values differ considerably in different symmetry of GaN. These show the usefulness of our layers for determination of the basic properties of cubic GaN using a wide range of techniques.

From the Hall transport measurement, the electrical properties of undoped cubic GaN samples depend on growth conditions and thickness. In this work, we successfully demonstrated p-type cubic GaN:Mn using C-doping and n-type behaviour from Si-doped cubic GaN. However, these samples have high electron density but low

mobility as the residual impurities and intrinsic defects were found to be higher inside the samples.

In this thesis, we extended the technology of growing cubic GaN to cubic $\text{Al}_x\text{Ga}_{1-x}\text{N}$. A number of cubic $\text{Al}_x\text{Ga}_{1-x}\text{N}$ samples with different Al content, x were grown and characterised by PL measurement. We found that the hexagonal PL starts to dominate when x is increased, even for thin samples. This could be due to the problems of maintaining cubic $\text{Al}_x\text{Ga}_{1-x}\text{N}$ growth. It could also be due to the miscibility gap between AlN and GaN. More results and data are required to explain this behaviour.

7.2: PROCESSING OF CUBIC GaN SUBSTRATE

The study on bulk cubic GaN showed that the interface between the cubic GaN and the GaAs substrate has only few percent of hexagonal content. Thus, the surface that was in contact with GaAs is the most suitable surface for further processing and growth. Due to the effect of strain, As inclusions and defects were already formed on the surface. By polishing the surface for ~2 hours, these problems were minimised and the surface still had low hexagonal content. In this work, the first working InGaN LED device grown on a polished free-standing cubic GaN substrate has been demonstrated. Our polished cubic GaN substrates also improve the quality of the grown device as been measured by luminescence and I - V characteristics.

7.3: CUBIC NITRIDES BASED RESONANT TUNNELLING DIODE

In the first stage of this work, the I - V characteristics of cubic $\text{Al}_x\text{Ga}_{1-x}\text{N}/\text{GaN}$ DBRTD were calculated for various band offset, well width, barrier composition and barrier thickness parameters. From this work, optimal designs of cubic $\text{Al}_x\text{Ga}_{1-x}\text{N}/\text{GaN}$ tunnel diodes that could be fabricated and characterised were proposed. The result was then used as a starting point for the growth of cubic $\text{Al}_x\text{Ga}_{1-x}\text{N}/\text{GaN}$ DBRTD. A number of cubic $\text{Al}_x\text{Ga}_{1-x}\text{N}/\text{GaN}$ tunnel devices with different structural parameters were grown. Some devices showed a clear NDR effect but not all of them

are reproducible due to breakdown of the device. This factor may also contribute to the irreproducibility of wurtzite (hexagonal) nitride based tunnel diodes in addition to the problem related to charge trapping.

7.4: SUGGESTIONS FOR FURTHER WORK

In this project, we successfully demonstrated $\sim 50\mu\text{m}$ bulk cubic GaN samples with low hexagonal content of about 10%. For further investigation, it would be practical if we use the samples to fill gaps in the table of properties of cubic GaN (in Chapter 2), e.g electron affinity.

We tried to understand the dependence of the electron properties of undoped cubic GaN layers on the layer thickness. However, such behaviour can not be well understood due to insufficient statistics and data. In fact, the measured samples were taken from different part of the wafer, where the growth conditions vary across a wafer. This makes the results incomparable. Thus, for future work, we suggest using the centre part of the wafer for each measured sample, as it has lower hexagonal inclusions, as determined from PL measurement, and makes the analysis more comparable.

In this work, we reported a working InGaN/GaN based LED on our free standing cubic GaN substrate for the first time. In future, we may invest this technology for making a high efficiency cubic nitride based laser diode (LD) as the effect of strain and piezoelectric and spontaneous fields would be insignificant.

We also used the growth technology of cubic GaN to grow cubic $\text{Al}_x\text{Ga}_{1-x}\text{N}$. However, the data analysis is insufficient to elucidate the dependence of hexagonal content on Al content, x . Therefore, a suitable growth for cubic $\text{Al}_x\text{Ga}_{1-x}\text{N}$ needs to be developed so that such behaviour can be well understood. Similar work can also be done for cubic $\text{In}_x\text{Ga}_{1-x}\text{N}$ in order to complete the study on cubic III-nitrides materials.

If the growth of cubic $\text{Al}_x\text{Ga}_{1-x}\text{N}$ is well established, then problems with barrier fluctuation can be reduced. This decreases the risk of damaging the tunnel device,

giving higher reproducibility of the device. If this project is given more time, fabrication and characterisation of cubic $\text{Al}_x\text{Ga}_{1-x}\text{N}/\text{GaN}$ DBRTDs with a wider variety of designs such as different well widths and barrier heights would be undertaken. From this work, more statistics and data on the tunnel devices would be available and eventually the optimum possible structure of the device can be proposed.

Appendix

The calibration procedure to estimate the percentage of hexagonal material in a bulk cubic GaN.

It is well known that the equation for a linear graph is given as

$$y = mx + c \quad (1)$$

where m is the gradient of the graph and c is the intersection at y-axis. From Figure 4.8, the dependence of PL intensity on distance from GaAs/GaN interface shows that c is zero and $m = 0.3627$. Therefore the average of PL intensity is found to be

$$\text{Average of PL intensity} = \frac{1}{2}(m \times d) \quad (2)$$

where d is the total thickness (distance) of the cubic sample that had been excited by micro laser, which is $35\mu\text{m}$. Solving equation (2), the average of PL intensity is equal to 6.3473.

The same procedure is applied for finding the percentage of hexagonal as a function of thickness. By assuming k is the gradient for the dependence of the hexagonal percentage on thickness, therefore

$$\text{Average of PL intensity} = k \times \text{Average of hexagonal percentage} \quad (3)$$

Knowing that the average of PL intensity = 6.3473 and average of hexagonal percentage = 10%, thus k becomes 0.6347. Correspondingly from equation (3), the percentage of hexagonal can be estimated by

$$\text{The percentage of hexagonal percentage} = \frac{1}{k} \times \text{PL intensity} \quad (4)$$

Calculating the first energy level in the quantum well and plotting the electron wavefunction in $\text{Al}_x\text{Ga}_{1-x}\text{N}/\text{GaN}$ double barrier structure using MS Visual Basic

The first part of this section shows the numerical method of calculating the first energy level, E_{pk} and plotting the distribution of electron wavefunction, $|\psi|^2(z)$ throughout a double barrier $\text{Al}_x\text{Ga}_{1-x}\text{N}/\text{GaN}$ structure.

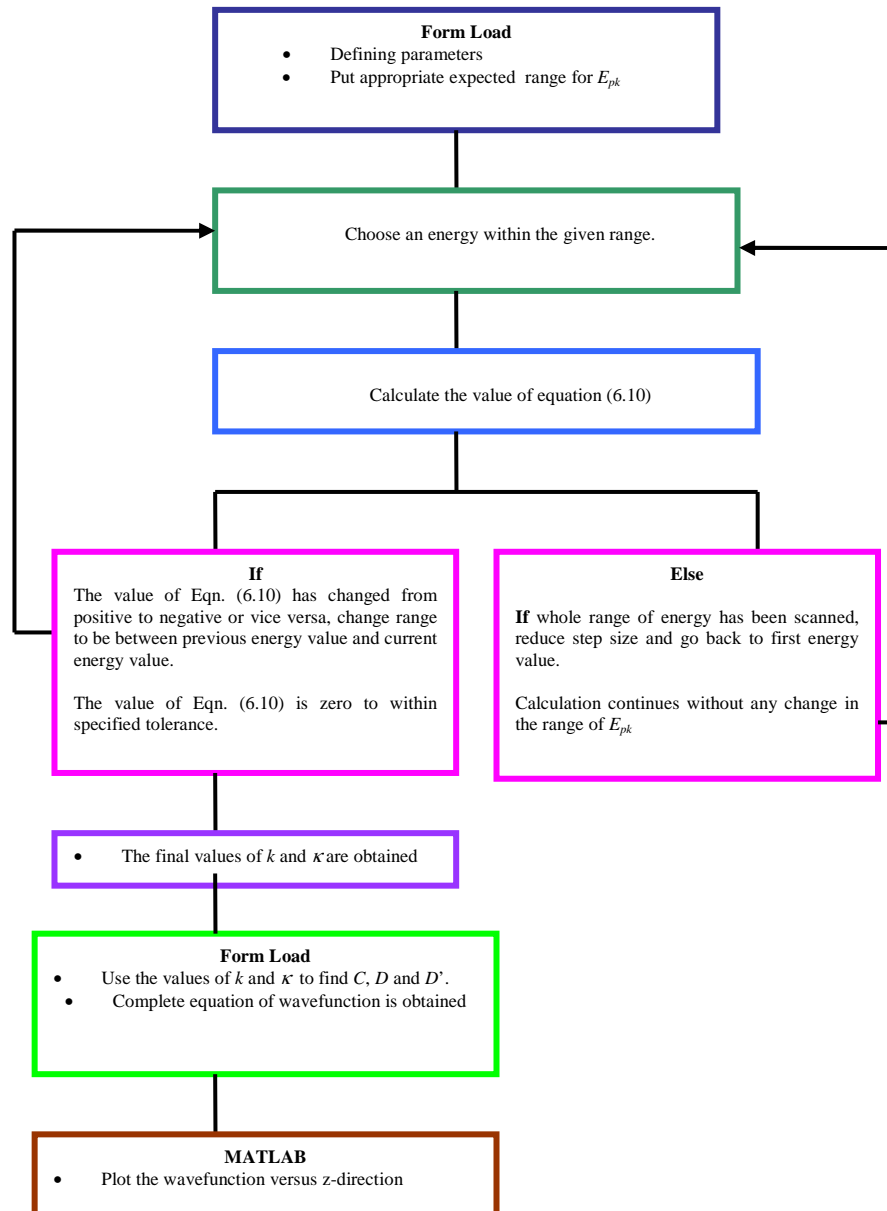


Figure 1: The flow chart on calculating the first energy level, E_{pk} and the distribution of electron wavefunction, $|\psi|^2(z)$.

The example of simulation program

1. Finding k and κ

Private Sub Command1_Click ()

Dim Fsteps(100000) As Double
Dim stepindex As Double
Dim stepsize As Double
Dim x As Double
Dim y As Double
Dim En As Double
Dim k As Single
Dim kappa As Single
Dim V0 As Double
Dim Fsteps(10000) As Double
Dim prev As Double

m0 = 9.109 * 10 ^ (-31)
mw = 0.15
mb = 0.16
a = 1 * 10 ^ (-9)
pi = 3.142
hbar = 1.055 * 10 ^ (-34)
Ecb = 0
Ecb = 5.607 * 10 ^ (-20)
V0 = 5.607 * 10 ^ (-20)
delta = 1E-37
stepindex = 1
nsteps = 1000
x = 1E-20
y = 5E-20
stepsize = (y - x) / nsteps

Do Until (stepsize <= delta)
 For En = x To y Step stepsize

Fsteps(stepindex) = ((mw / mb) * (((V0) / (En - Ecb)) - 1)) ^ (1 / 2) - Tan((((a ^ 2) *
 m0 * mw * (En - Ecb)) / (2 * (hbar ^ 2))) ^ (1 / 2))
 prev = ((mw / mb) * (((V0) / ((En - stepsize) - Ecb)) - 1)) ^ (1 / 2) -
 Tan((((a ^ 2) * m0 * mw * ((En - stepsize) - Ecb)) / (2 * (hbar ^
 2))) ^ (1 / 2))

'Calculate k (prev)

 k = ((2 * m0 * mw * ((En - stepsize) - Ecb)) / (hbar ^ 2)) ^ (1 / 2)

'Calculate kappa (prev)

 kappa = (mb * k / mw) * ((mw / mb) * (((2 * m0 * mw * V0) / ((hbar ^
 2) * (k ^ 2))) - 1)) ^ (1 / 2)

```

'view all value
  List1.AddItem En
  List2.AddItem Fsteps(stepindex)
  List3.AddItem k
  List4.AddItem kappa

If (Fsteps(stepindex) >= 0 And prev < 0 Or Fsteps(stepindex) < 0 And prev >= 0
Then
    List5.AddItem En
    List6.AddItem Fsteps(stepindex)
    List7.AddItem En - stepsize
    List8.AddItem prev
    List9.AddItem k
    List10.AddItem kappa

    GoTo continue

End If

Next En

continue:
  x = En - stepsize
  y = En
  nsteps = nsteps * 4
  stepsize = (y - x) / nsteps
  stepindex = stepindex + 1

Loop

End Sub

```

2. Finding C, D and D'

```

Private Sub Command1_Click()
Dim C As Single
Dim D1 As Single
Dim D2 As Single
Dim k As Single
Dim kappa As Single
Dim a As Single

k = Val(Text1.Text)
kappa = Val(Text2.Text)
a = Val(Text6.Text)

```

'Calculate C, D1 and D2

$$C = 1 / (((\cos((-k * a) / 2) ^ 2 / (2 * \text{kappa})) + (a / 2) + (\sin(k * a) / (4 * k)) - (\sin(-k * a) / (4 * k)) + (\cos((k * a) / 2) ^ 2) / (2 * \text{kappa})) ^ (1 / 2))$$

$$D1 = \cos((-k * a) / 2) / \exp((-kappa * a) / 2) * C$$

$$D2 = \cos((k * a) / 2) / \exp((-kappa * a) / 2) * C$$

Text3.Text = D1

Text4.Text = C

Text5.Text = D2

End Sub

3. Plotting through MATLAB

a=1e-9;

>> z1=-2.5e-9:1e-11:-a/2;

>> z2=-a/2:1e-11:a/2;

>> z3=a/2:1e-11:2.5e-9;

>> k=767512241.584245;

>> kappa=320232031.192469;

>> psi1=18044.72*exp (kappa*z1);

>> psi2=16580.93*cos (k*z2);

>> psi3=18044.72*exp (-kappa*z3);

>> plot(z1, psi1.^2,'b');

>> hold on

>> plot(z2, psi2.^2,'b');

>> plot(z3, psi3.^2,'b');

>> set(gca,'fontsize',18);

>> xlabel('z (nm)');

>> ylabel('\Psi^2');

>> title('Wavefunction, (\Psi^2) versus z-direction');

Calculating the tunnelling current in $\text{Al}_x\text{Ga}_{1-x}\text{N}/\text{GaN}$ double barrier structure

The second part of this section describes the numerical procedures for calculating the tunnelling current in $\text{Al}_x\text{Ga}_{1-x}\text{N}/\text{GaN}$ double barrier structure. Firstly, structural parameters, such as well and barrier widths and its corresponding E_{pk} , k and κ are given in the numerical program. Related constants are also defined in the program. Using this information, the integral tunnelling current in the device structure is calculated as a function of bias voltage, V . An example of simulation script is given as follows.

The example of calculating tunnelling current

```
clear all

V0 = 0.44;
κ = 7.6620 * 10 ^ (8); %
k_well = 1.1012 * 10 ^ (9);
a = 2 * 10 ^ (-9); dw = 1 * 10 ^ (-9);
κa = κ * a;
Epk0 = 0.308304174;
mass = 0.15 * (9.109 * 10 ^ (-31));
h = 4.14 * 10 ^ (-15);
pi = 3.142;
hbar = 6.588160407 * 10 ^ (-16);
vel = hbar * 1.6e-19 * k_well / mass;
hv = hbar * vel;
q = 1;
Ef1 = 0.09128;
kb = 8.62 * 10 ^ (-5);
Temp = 300;
kT = kb * Temp;

qV = 0;
Epk = 1;
M = 300;
aqV = (1:M)' * (0.01);
aQ = zeros(M,1);

for n = 1:M
    qV = aqV(n)
    Epk = Epk0 - (0.5 * qV)
```

```
aQ(n)= quad(@(E)(1./(1+((E- Epk)./0.5).^2).*((a./hv).^2).*((1+((V0.^2).*(exp(kappa)-
exp(-kappa)).^2))./(16.*E.*(V0-E)).^2)).*(log(((1+exp((Ef1-E)./kT))./(1+exp((Ef1-qV-
E)./kT)))))).*((q.*mass.*kT)./(2.*(pi.^2).*(hbar.^3))),0.00001,0.09128)
```

```
end
```

```
plot(aqV,aQ)
```